UNIVERSITY OF CATANIA

INTERNATIONAL PhD IN CHEMICAL SCIENCES

XXXVI CYCLE

PhD THESIS

Francesca Laneri

Development of Photoactivatable Polymeric Nanoparticles for Multimodal Antitumoral Therapies

Tutor
Prof. Salvatore Sortino

PhD Coordinator
Prof. Salvatore Sortino

SUMMARY

Aim of the thesis **1**

1. Introduction **2**

1.1 General background **2**

1.2 NO and NO-Photodynamic Therapy **3**

1.3 Singlet Oxygen and Photodynamic Therapy **5**

1.4 Photothermal therapy **7**

1.5 Cyclodextrin polymers as chemotherapeutics delivering devices **8**

1.6 Conventional chemotherapeutics: Sorafenib and Lenvatinib **9**

2. Results and discussion **13**

2.1 Materials and methods **13**

2.2 A Fluorescent β-Cyclodextrins Polymer Encapsulating Sorafenib and Releasing Nitric Oxide Under Visible Light **19**

2.3 A Supramolecular Nanoassembly of Lenvatinib and a Green Light-Activatable NO Releaser for Combined Chemo-Phototherapy **40**

2.4 A mixed β-γ-cyclodextrin branched polymer with multiple photo-chemotherapeutic cargo **62**

2.5 Near-Infrared Plasmonic Gold Nanostructures by Pomegranate Extract and Their Supramolecular Assembling with Chemo- and Photo-Therapeutics **78**

2.6 Photobehaviour of curcumin in biocompatible hosts: the role of H-abstraction in the photodegradation and photosensitization **93**

2.7 Dextrans polymer functionalized with BODIPY-based NO Photodonor **110**

General conclusions **112**

Acknowledgements **113**

Outcomes **114**

Bibliography **117**

List of abbreviations

α-CD: α-cyclodextrin
ABC: ATP Binding Cassette
ACHN: Renal adenocarcinoma cells line
Au: Gold
β-CD: β-cyclodextrin
βγCD-NOPD: β- and γ-cyclodextrins polymer
CD: Cyclodextrin
γ-CD: γ-cyclodextrin
CUR: Curcumin
CW: Continuous Wave
DLS: Dynamic Light Scattering
DMSO: Dimethyl Sulfoxide
EMA: European Medicines Agency
EtOH: Ethanol
FDA: Food and Drug Administration
FITC: Fluorescein isothyocianate
FRET: Förster Resonance Energy Transfer
HCC: Hepatocellular carcinoma
Hep-G2: Hepatocellular carcinoma cells line
HPLC: High Performance Liquid Chromatography
HAS: Human Serum Albumin
IC_{50}: Half Maximal Inhibitory Concentration
IR: Infrared
ISC: Intersystem Crossing
LSPR: Localized Surface Plasmon Resonance
LVB: Lenvatinib
MCF-7: Breast cancer cells line
MDR: Multidrug Resistance
MKI: Multikinase Inhibitor
MRP2: Multi Drug Resistance Protein
MTT: 3-(4,5-dimethylthiazol-2-yl)-2,5-diphenyltetrazolium bromide tetrazolium
MWCO: Molecular Weight Cutoff
NBF: Nitrobenzofurazane
NIR: Near Infrared
NMR: Nuclear Magnetic Resonance
NOPD-1: 4-nitro-3-(trifluoromethyl)amino derivative
NPs: Nanoparticles
MeOH: Methanol

NO: Nitric Oxide
NO-PDT: Nitric Oxide photodynamic therapy
NOPD: Nitric Oxide Photodonor
$^1O_2$: Singlet oxygen
o/w: oil/water
P-gp: P-glicoprotein
PBS: Phosphate Buffered Saline
PDT: Photodynamic therapy
PS: Photosensitizer
PSE: Pomegranate Seeds Extract
PTT: Photothermal therapy
Rhod-NO: NOPD with Rhodamine as antenna
RNS: Reactive Nitrogen Species
ROS: Reactive Oxygen Species
SRB: Sorafenib
TEM: Transmission Electron Microscopy
UV/ Vis: ultraviolet/visible
Vis: Visible
VEGFR: Vascular Endothelial Growth Factor
w/w: weight/weight

Aim of the thesis

This project aims to the design, development, characterization and potential transfer on industrial scale-up of Photoactivatable Nanoparticle Polymeric Systems for Novel Multimodal Antitumoral Therapies. It is intended to develop multicargo nanocarriers encapsulating “conventional” chemotherapeutics, while simultaneously integrating photoprecursors generating radical species and heat as “unconventional” therapeutic agents.

In particular, nitric oxide (NO), singlet oxygen ($^1O_2$) and/or heat will be generated in a selective, sequential or simultaneous fashion, exploiting the precise spatiotemporal control offered by light stimuli with biocompatible energy, absorbed by suitable photoprecursors. They will be integrated into polymeric nanocarriers through covalent and/or non-covalent approaches, together with conventional chemodrugs, with the purpose to obtain additive and/or synergistic therapeutic effects. This photo-chemo combinatory approach can, in principle, maximize the therapeutic action of the traditional antitumorals while minimizing their side-effects and overcoming drug-resistance. Moreover, all the photogenerators will be active only in the illuminated areas, avoiding the lack in site-specificity, a substantial issue of the common antitumorals.

The entire project was finalized through the instrumentations and the skills available at the University of Catania and thanks to expertise of the academic and industrial partners (University of Almería, Spain, and byFlow srl of Bologna, Italy) involved.

Chapter 1

1. Introduction

1.1 General background

Over the past few years, the employment of nanomaterials able to release unconventional therapeutic agents to enhance the therapeutic efficacy under the exclusive control of light stimuli has collected a tremendous interest in nanomedicine.

In particular, a wide variety of nanoparticles has been engineered with suitable photoactivatable components to open up novel and stimulating avenues for intriguing unconventional therapeutic approaches for fighting cancer diseases, such as photodynamic therapy (PDT), NO photodynamic therapy (NO-PDT) and photothermal therapy (PTT). These emerging treatments hinge on the localized cytotoxic effects induced by the photorelease of $^1O_2$ and NO as reactive radical species or by the photogeneration of heat, developed with superb spatiotemporal control by appropriate photoprecursors. These unconventional approaches may be used in combination with, or even be alternative to, conventional chemotherapeutics [1].

Conventional chemo-drugs are anticancer agents that have already been widely approved by FDA (Food and Drug Administration) and/or EMA (European Medicines Agency) and that are commonly administered in antitumoral therapies. Nevertheless, they show some deficiencies that the modern medical research still has to get the better of. Indeed, they usually are target-specific agents (i.e., DNA or a protein) and present several side effects. Their principal failure consists in the Multiple Drug Resistance (MDR), the mechanism through which many tumoral pathologies frequently develop resistance to anticancer medicals [2].

The main pathway that stands behind MDR is the overexpression of transporters belonging to the family of ATP Binding Cassette (ABC), like P-gp (P-glycoprotein)/ABCB, P-gp/ABCB1, MRP2 (Multi Drug Resistance Protein)/ABCC2, MRP3/ABCC3 and BCRP (Breast Cancer Resistance Protein)/ABCG2. They localize on the surface of plasma membranes of hepatocytes, renal tubular cells, enterocytes and other epithelial cells [3,4]. The substrates of P-gp are mainly amphipathic, hydrophobic and cationic molecules [3–5]. In the treatment of hepatocellular carcinoma (HCC), for example, the overexpression of P-gp plays a main role in the resistance to doxorubicin [6,7] and in

HCC patients who underwent tumor resection it was observed an increased MRP2 expression, leading to a poor response to cisplatin co-therapy [8].

The combination with unconventional drugs have come into play in this scientific battle, aimed to the enhancement of the therapeutic outcome through synergistic or additive effects and to the overcome of MDR [9].

1.2 NO and NO-Photodynamic Therapy

NO belongs to the class of Radical Nitrogen Species (RNS). It is a gaseous, ephemeral transient radical, that has for long been considered only as an air pollutant, but that has gained its deserved scientific attention in 1992, when the journal of Science named it "molecule of the year" [10]. Six years later, the Nobile Prize for Physiology and Medicine would have been assigned to Drs. Furchgott, Ignarro and Murad for having discovered the involvement of NO in many biological routes [11]. By that moment, the slogan "Say YES to NO" became more and more popular among scientists. Nowadays, the active role of NO in physiological and pathophysiological pathways (such as neurotransmission, hormone secretion, vasodilatation, immune response to infections, platelet aggregation and wound repair) is well-known, but they are its anticancer and antibacterial properties that are only a recent discovery [12].

NO is a multi-target cytotoxic species, able to reach more than one biological substrate, like mitochondria, cell membranes and nuclei. Furthermore, it is an uncharged, lipophilic and small molecule, with short half-life in blood (<1s): all these features allow it to diffuse easily within the cytoplasmatic environment over short distances (<200 μm) and, hence, to minimize off-target side effects. Most importantly, NO is able to overcome the MDR issues, frequent for the conventional drugs [13].

It is mandatory to confine the region of action of NO. Radicals are harmful agents if indiscriminately generated, but when wisely produced in the tumoral areas, they become cytotoxic powerful allies, exclusively directed to the target of interest.

Nonetheless, it has been proven that the biological effects of NO are strictly dependent on its concentration. In fact, in the range of picomolar, it encourages tumour proliferation, whereas tumour growth inhibition is observed at micromolar dosage [14]. Recent scientific evidences have also highlighted that, at the appropriate amount, the released NO is able to down-downregulate P-gp expression levels on the membranes, sensitizing tumoral cells to the conventional drugs and tackling the insurgence of MDR [15].

This dosage delicate balance has led to the crucial exigency of new approaches to ensure a precise spatiotemporal delivery of NO, and light has come to the aid of this modern challenge, giving rise to the so-called NO-PDT as unconventional chemotherapeutic approach [16]. Light triggering is a very biofriendly tool. In fact, while preserving the fundamental biological and physiological parameters (i.e., pH, temperature, ionic strength), it provides fast reaction rates, strictly confined in the illuminated areas [17].

The basic idea comprises the use of NO "photocaging" compounds, molecules that covalently incorporate biologically active species within a photoresponsive chromogenic antenna, which makes them temporarily inactivated. Only luminous stimuli, selectively addressed to the photosensitive moieties, can trigger the "photo-uncaging", liberating the "caged" molecule, in this case NO, in its active form (see Figure 1). Site control is restricted to the illuminated area; time and dosage precision is granted by light duration and/or intensity since NO photocage can be regulated, initiated and even stopped when photons are exploited as external input [18]. All these qualities make NO photodonors (NOPDs) very appealing therapeutic tools, much more than pH, enzymatic or thermal activable compounds [19,20].

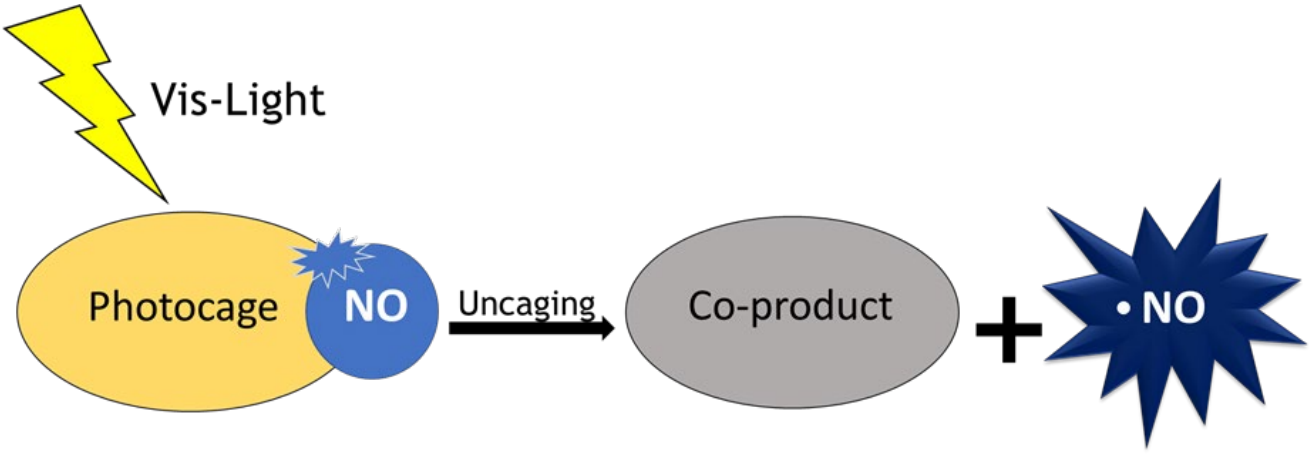

Figure 1: Schematized NO phodecaging process.

The most advanced studies have permitted the direct visualization of the "decaged" NO by the employment of fluorescent components, as the latest scientific strategy of the so-called "See and Treat" approach suggests. Not only do fluorescence techniques allow the tracking of the NO photoprecursors, but they also grant a real-time quantification and localization of the photoreleased radical in a non-invasive method.

NO photocage compounds often integrate "persistent" fluorescent tags (see Figure 2) and this seems to be the most convenient solution, as far as interchromophoric interactions are carefully avoided and the phenomenon of the NO visualization by the fluorophoric unit does not compromise the decaging from the photoreleasing moiety and vice versa [16].

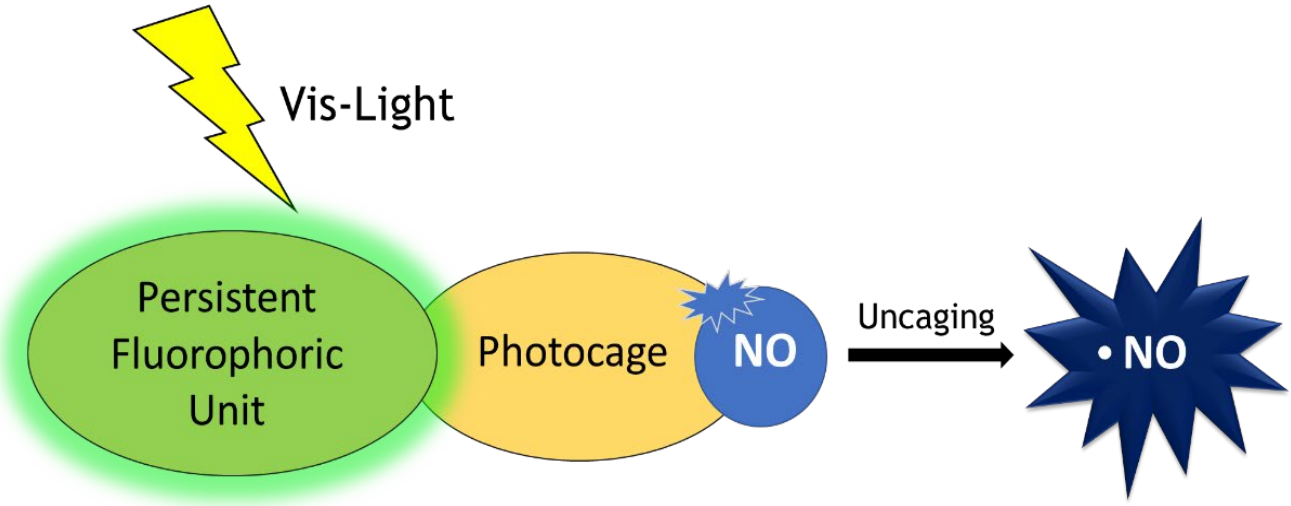

Figure 2: Schematized NO phodecaging process in the presence of a persistent fluorophoric unit, whose emissive properties do not change before and/or after the NO photorelease reaction.

NOPDs that may be applied for therapeutic goals must comply with the adequate requirements for a safe and successful employment.

Besides stability and non-toxicity in the dark, they must dispose of an efficient quantum yield of NO production. Moreover, their activation must not lead to co-products that may be toxic or absorb in the same region of the NOPD itself, since undesired inner filter effects and/or secondary photochemical reactions may occur. Additionally, visible light activated NOPDs are recommended, considering that UV light is far less biocompatible, and it much more hardly penetrates tissues [21].

1.3 Singlet Oxygen and Photodynamic Therapy

Among the light-induced unconventional approaches to cancer treatments, PDT represents one of the most promising and it also finds applications into clinics [22,23]. It is mainly based on the cytotoxic properties of the highly reactive $^1O_2$, which belongs to the category of Reactive Oxygen Species (ROS) [24]. It is much more oxidant than molecular oxygen and is catalytically generated by collisional energy transfer between the excited triplet state of a suitable photosensitizer (PS) and the

surrounding molecular oxygen [25]. Upon light excitation, the PS passes from the ground state to the excited state, before decaying back again to the ground state either with concomitant emission of light as fluorescence or with intersystem crossing, to form a more stable and long-lived excited triplet state (Figure 3). The latter may be quenched by nearby molecular oxygen *via* energy transfer mechanism (Type II reaction), which gives rise to the photoproduction in $^1O_2$, and/or *via* electron transfer mechanisms (Type I reaction), which leads to the generation of other types of ROS, such as a superoxide anion radical ($O_2^{\bullet -}$), a hydroxyl radical ($OH^{\bullet}$), or hydrogen peroxide (H_2O_2) [26].

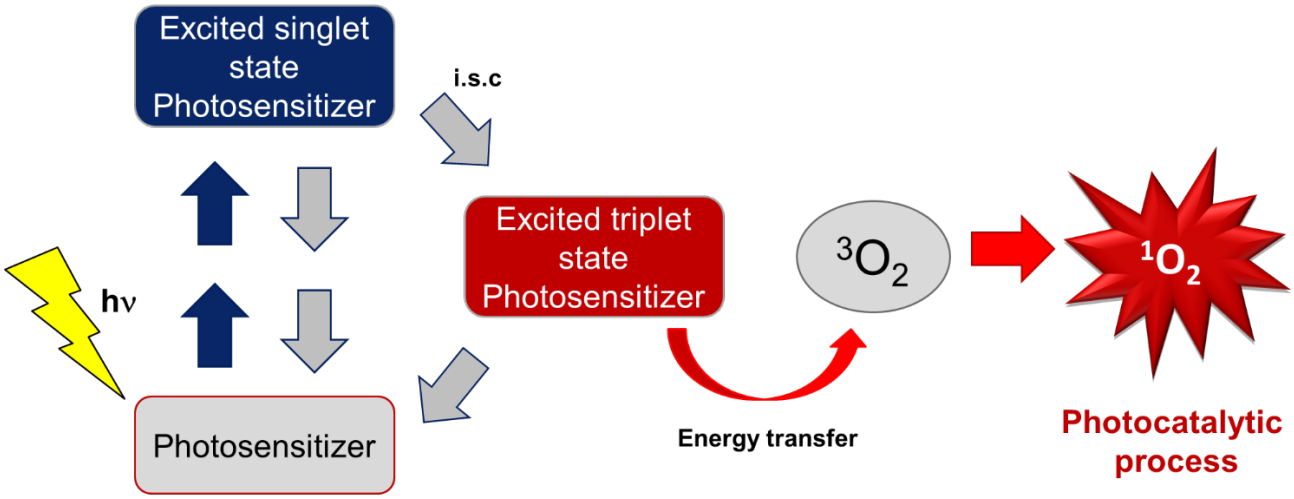

Figure 3: Photocatalytic production of $^1O_2$ in PDT.

Type I and Type II reactions can occur either simultaneously or competitively: the ratio between them depends on the content of oxygen and on the PS used. Anyway, it seems that Type II reaction plays a key role in cytotoxicity [24]. The *in situ* production of $^1O_2$ can explain the photodynamic action on tumoral cells [27], causing irreversible damage to lipids, protein and nucleic acids in the cellular environment and therefore to cell death [28].

Porphyrins and phthalocyanines play a key role as PSs in PDT, thanks to high triplet quantum yields, very long triplet lifetimes, strong absorption in the visible region: these are indeed all crucial parameters for a satisfying photoproduction of $^1O_2$ [29].

In recent years, the combination of PDT with NO-PDT is opening new possibilities in the field of multimodal therapeutic strategies. NO and $^1O_2$ share important advantages as chemotherapeutics, such as the small size, multitarget cytotoxic action, absence of MDR and confinement of their activity over short distances. Just like NO, $^1O_2$ displays short lifetime (<0.1 ms) and range of action

(10–20 nm), which confine the cytotoxic effects to the irradiated sites [30]. NO photorelease is independent of $^1O_2$ availability and it can supplement PDT under hypoxic conditions, which are typical of some tumours and where PDT may fail [31].

1.4 Photothermal therapy

Photothermal therapy (PTT) represents another emerging unconventional treatment for cancer diseases, with very appealing and promising prospects in the burgeoning field of nanomedicine [32]. Suitable photothermal agents are employed to achieve the selective heating of the tumour tissue [33]. When the PTT agents absorb light, their electrons undergo to a transition from the ground state to the excited state. Afterwards, the electronic excitation energy relaxes through nonradiative decay pathways, increasing the kinetic energy and subsequently leading to the overheating of the local environment [34]. Hyperthermia, commonly defined as tens of minutes heating tissue in the range 41–47 °C [35], gives rise to irreversible cell damage due to the loose of cell membranes, denaturation of proteins and eventually leads to tumour destruction. However, it should be paid attention to the employment of conventional heating sources as the surrounding healthy tissues may be damaged too. Instead, the use of suitable PSs, which are at the basis of PTT, offer the great possibility to overcome this limitation. The photoirradiation of the chromophore produces the overheating of only the space around it and lead to selective tissue damage [36]. Naphthalocyanines and metal porphyrins have been some of the most used PSs as exogenous dyes, but they are limited by the photobleaching under laser irradiation, which is actually a serious drawback [28].

The more and more growing field of material science has provided to PTT a variety of nanostructures with unique properties for this application [37]. In particular, gold nanoparticles (AuNPs), Au nanorods and Au nanoshells are ideal nanomaterials for such application, thanks to the absorption coefficients in the visible (Vis) and NIR region several orders of magnitude greater than those of other photoabsorbing dyes, high rates of light-to-heat conversion, excellent photostability and good biocompatibility [38]. The AuNPs optical properties are dictated by the so-called localized surface plasmon resonance band (LSPR) [39], which is related to a collective excitation of conduction electrons. Depending on the size, shape, structure and environment, the LSPR absorption can fall in a wide region from the Vis to the NIR region. Moreover, thanks to the nano-size, AuNPs display good tumour retention, as they are able to penetrate the leaky tumour vasculature [40].

1.5 Cyclodextrin polymers as chemotherapeutics delivering devices

NO photodecaging systems require appropriate materials as delivering devices. Polymers of different nature are one of the most advantageous tools for therapeutic goals.

Indeed, assembling structures offer many perks: the possibility to concentrate a large number of chromophores in a confined region of space, boosting the light harvesting properties; the predisposition to be easily connected to optical fiber light guides; the opportunity of being exploited as drug carriers for the concomitant delivery of unconventional antitumorals, which is a crucial point in the development of multimodal therapeutic systems [19].

Cyclodextrins (CDs) are appealing carriers, both for common and uncommon therapeutic units, since they respect the fundamental criteria as efficient delivery vehicles: good biocompatibility; acceptable cell-penetrating properties; preservation of the optical features of the chromophores [41].

CDs are cyclic oligosaccharides consisting of six (α-CDs), seven (β-CDs), eight (γ-CDs), or more D-(+)glucopyranose units linked through α-1,4-glycosidic bonds [42].

They are shaped like truncated cones, characterized by secondary hydroxy groups localized in the wider edge and primary groups extending from the narrow edge (see Figure 4). This typical chemical structure makes hydrophilic the outer surface, while the central cavity, made of glucose residues, displays a grade of lipophilicity comparable with an aqueous ethanolic solution.

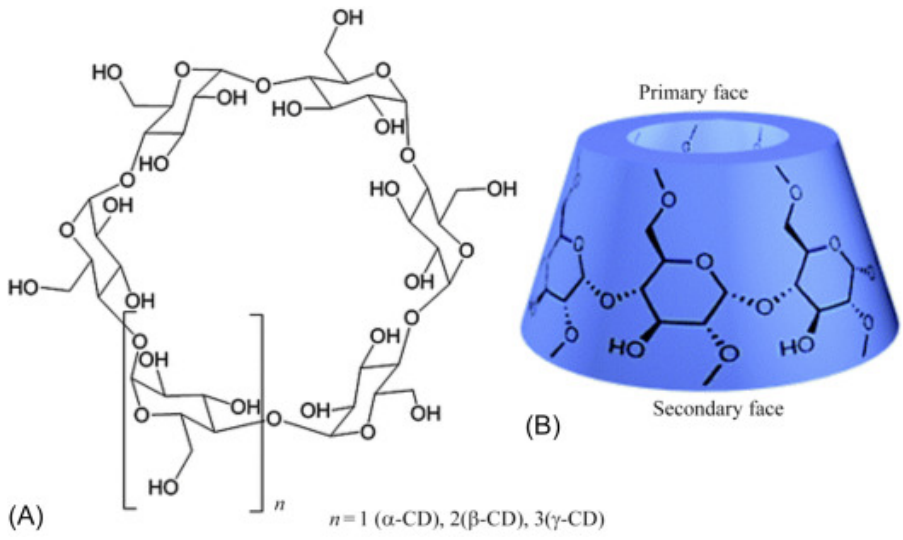

Figure 4: (A) Structures of CDs; **(B)** 3D structure of CDs [43].

In other words, the inner cavity constitutes a sort of lipophilic nanoenvironment, in which suitably small drug molecules may enter and be included [44]. No covalent bonds are formed between the CDs and the encapsulated molecules, but a so-called "inclusion complex" is arranged (see Figure 5).

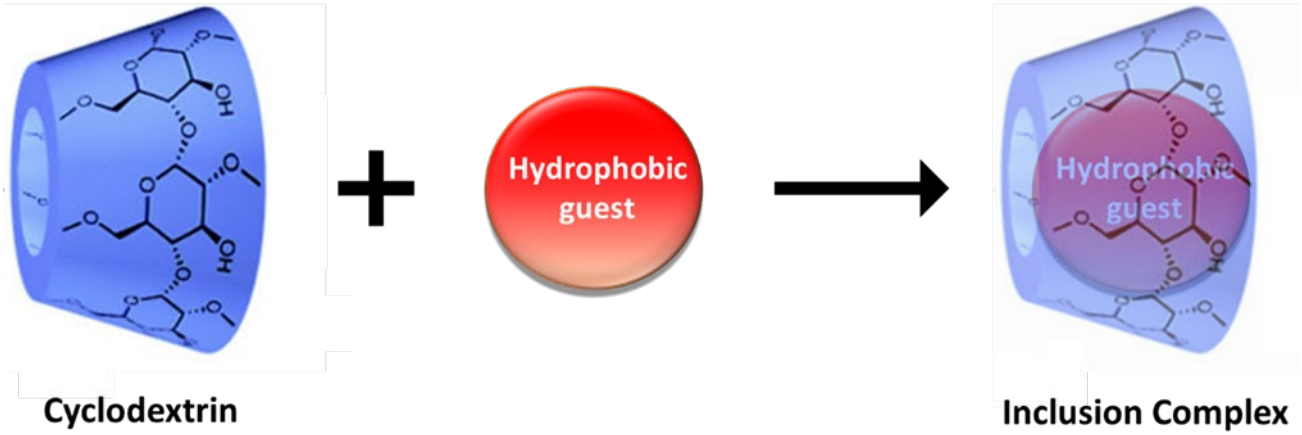

Figure 5: Schematic representation of the "inclusion complex" formation between CDs and a hydrophobic molecule as a guest.

A thermodynamic constant K, that may be named as affinity, stability or binding constant governs the formation and the dissociation of the host-guest complex. Higher values of K correspond to a more stable inclusion, and to a less probable dissociation. Many factors can influence the K, like the size of the CD cavity and that one of the guest molecule (or part of it). Generally, a good complex strength is gained when there is size complementarity between the guest and the CD cavity [45].
CDs are nowadays more and more exploited in the pharmaceutic field to enhance the bioavailability of insoluble drugs by increasing their solubility, dissolution, and/or molecule permeability. Indeed, the hydrophobic guests gain through CDs higher availability at the surface of the biological barrier, eg, skin, mucosa, or the eye cornea [46].

1.6 Conventional chemotherapeutics: Sorafenib and Lenvatinib

Sorafenib (SRB) and Lenvatinib (LVB) are first-line chemotherapeutics for the treatment of hepatocellular carcinoma (HCC), which is the fifth more diffused cancer and the third most fatal worldwide [47,48].

SRB (see Figure 6) is an orally active multikinase inhibitor (MKI), able to target Raf kinases, vascular endothelial growth factor (VEGFR)-2/-3, platelet-derived growth factor receptor β, Fms-like tyrosine kinase 3 and c-Kit.

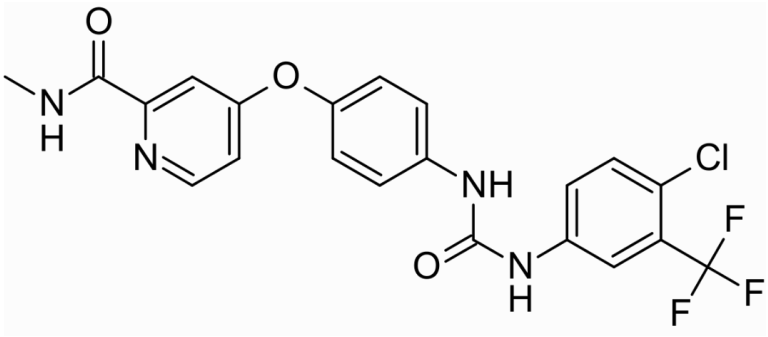

Figure 6: Molecular structure of SRB.

Until the U.S.A. FDA and the EMA approval of SRB, the therapeutic procedures were quite inadequate for advanced liver carcinoma, that displayed almost no response to common therapies [49], [50].

Preclinical studies have also shown that SRB is effective for the treatment of other types of tumours, as it was proven its inhibiting activity on the proliferation and angiogenesis of metastatic renal cell carcinoma [51] breast cancer [52], melanoma [53], thyroid [54] and colorectal carcinomas [55].

Anyway, diarrhea, nausea and an abnormal increase of tiredness have been reported as frequent secondary effects [56]. Though, it seems that they are the dermatologic events, like rashes, that mostly affect patients quality of life [57], besides constitutional syndrome with asthenia, anorexia and weight loss [58]. The several secondary effects lead to mandatory drug dose reduction and often necessary temporary discontinuation [59]. SRB monotherapy application is strongly limited, calling for a urgent research of new alternative therapeutic approaches, including multimodal treatments that may reduce SRB dosage [60].

In addition to the problematic toxicological background, the therapeutic efficacy of the drug is compromitted by the very low water-solubility under physiological conditions (ca. 10 ng/mL) [61] and fast metabolism, i.e, bioavailability is severely low.

For these reasons, a number of different nanocarriers have been proposed over the last years to improve its therapeutic profile [62]. Two SRB formulations are currently available for oral administration [63]. In particular, polymeric-based nanocarriers have shown great potential for the

systemic treatment of liver tumours and fibrosis [60], [32,64–66]. SRB-loaded nanoparticles polymers micelles or lipid nanocarriers [67] represent valid choices to optimize bioavailability, pharmacokinetics, and to target the drug directly to malignant cells or metastasis [63].

It has been demonstrated that the intracellular accumulation of SRB is regulated by particular proteins, that are P-gp, MRP2 and BCRP [68], extruding SRB itself or its metabolites, whose chemical properties are effectively proper of P-gp and MRP2 substrates [69]. As a consequence, SRB resistance in HCC is one of the most significant obstacles in the therapeutic success, due to transporters overexpression and, hence, enhanced drug extrusion [70]. The scientific urgency to overcome MDR is therefore to be added.

Also LVB (see Figure 7) is an oral chemodrug, whose activity is based on multiple receptor tyrosine kinases inhibition [71]. Some of its main targets are vascular endothelial growth factor receptors 1–3 (VEGFR1–3), fibroblast growth factor receptors 1–4, RET, c-kit, and platelet-derived growth factor receptor α [72].

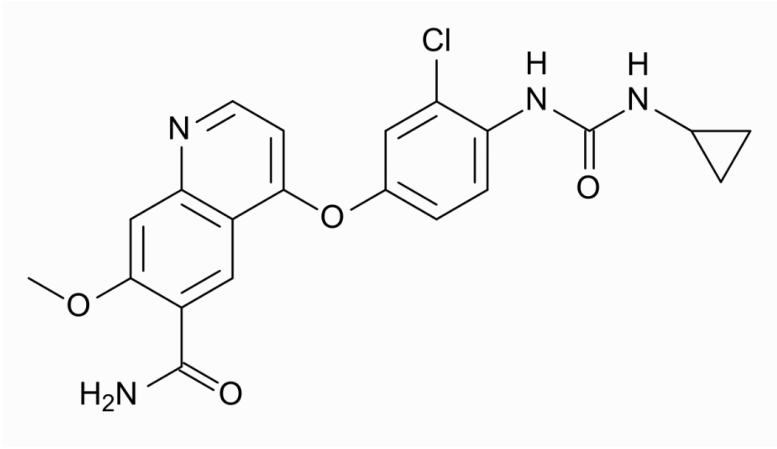

Figure 7: Molecular structure of LVB.

In 2015 it was approved for differentiated thyroid cancer treatment [73], and subsequently for advanced renal cell carcinoma as a combined drug [74]. Recent studies have reported higher efficiency for LVB in unresectable HCC treatment in comparison to SRB: in particular, it has demonstrated to inhibit tumour angiogenesis with more efficient impact [75].

Nonetheless, LVB is very poorly water soluble at physiological conditions [76] and displays low bioavailability [77]. The aqueous solubility was calculated to be 0.7 μg/mL, at 37 ± 0.1 °C [78], thus the clinical administration of the chemodrug is in its Mesylate derivative. Still, the oral bioavailability remains quite low (~36 %) [79], and large dosages are required to give an effective antitumor action.

As a consequence, the secondary effects result to be amplified and limit the available treatment duration [80]. A trial in Japanese patients, affected by advanced HCC, determined 12 mg as the maximum tolerated LVB dose, administered daily in 4-week cycles on a continuous schedule [56]. In a phase II study, patients received oral LVB doses on the basis of the bodyweight (8 mg/day for < 60 kg; 12 mg/day for ≥ 60 kg). When LVB-related toxicities were shown, treatment interruptions were necessary, followed by dosage reductions (to 8 mg and 4 mg/day, or 4 mg every other day) [75].

LVB has been reported to exert hypertension, diarrhoea, decreased appetite and weight, tiredness, nausea, proteinuria, stomatitis, dysphonia, headache and palmar-plantar erythrodysaesthesia syndrome [81]. Thus, novel strategies leading to LVB dosages diminution, such as the combination with unconventional antitumoral agents, are highly desirable.

Chapter 2

2. Results and discussion

2.1 Materials and methods

Chemicals: LVB mesylate that was purchased from Quimigen (HY-10981, Madrid, Spain). CUR (C7727, ≥94% curcuminoid content, ≥80% Curcumin), Pluronic® P123 (EO20–PO70–EO20, MW 5750 g mol^{-1}), Pluronic® F127 (EO100–PO70–EO100, MW 12,600 g mol^{-1}), and HSA were purchased from Merck KGaA (Germany). Maize zein (Z) (F4400C non-GMO/food grade) was a kind gift from Flo Chemical Corporation (Ashburnham, MA, USA). Caprylocaproyl macrogol-8 glycerides (Labrasol®) and propylene glycol monolaurate (Lauroglycol 90®) were a kind gift from Gattefoss´e (France). βγCD-NOPD synthesis is reported in the experimental section. Zinc phthalocyanine tetrasulphonate was purchased from Porphyrin Pdts and used without further purification. All the other chemicals were purchased by Sigma-Aldrich (Milan, Italy), and used as received.

Poly-CD was synthetized by crosslinking β-CDs with epichlorohydrin, under strong alkaline conditions, following a described method [82]. The polycondensation reaction led to a mixture of different molecular weight compounds. Separation was carried out with size exclusion chromatography (SEC) with water compatible high performance columns exploiting pullulan standards. The β-CD content was ca. 70% w/w, as determined through NMR (Nuclear Magnetic Resonance) spectra.

Rhod-NO and NBF were synthesized on the basis of previously reported procedures developed by the research group of Prof. Sortino [83,84].

The model compound NOPD-1 was synthesized according to our previously reported procedure [85].

SRB concentration was determined by absorption spectroscopy, using a molar extinction coefficient of 41280 M^{-1} cm^{-1} at 264 nm in MeOH solution and 37500 M^{-1} cm^{-1} at 269 nm when complexed within the β-CDs polymer [63]. The concentration of LVB was determined through absorption spectroscopy, using a molar extinction coefficient equal to 72.350 M^{-1} cm^{-1} in MeOH at 241 nm and 62.100 M^{-1} cm^{-1} at 245 nm when complexed within Poly-CD.

All solvents used for the spectrophotometric studies were at spectrophotometric grade.

MilliQ water was used for the polymer solubilization for the chemical and photochemical assays, except when otherwise indicated in the experimental section.

Instrumentation: UV/vis absorption spectra were recorded with a Jasco V 650 spectrophotometer. Fluorescence emission spectra were performed with Spex Fluorolog-2 (mod. F-111) spectrofluorimeter.

Fluorescence lifetimes were recorded with the same fluorimeter equipped with a TCSPC Triple Illuminator. The samples were irradiated by a pulsed diode excitation source Nanoled at 455 nm. The kinetics were monitored at 530 nm for both the polymer and the complexes; the prompt was registered at 455 nm. The system allowed measurement of fluorescence lifetimes from 200 ps.

The multi-exponential fit of the fluorescence decay was obtained using the following equation:

$$I(t) = \Sigma\alpha_i \exp(^{-t/\tau i})$$

For absorption and fluorescence assays, quartz cells with a pathlength of 1 cm were used.

NO photodecaging: NO photodecaging analysis were performed by irradiating the samples in solution in a quartz cell (1 cm pathlength, 3 mL capacity) under gentle stirring, by using a 100 mW continuum blue laser (λ_{exc} = 405 nm) having a beam diameter of ca. 1.5 mm.

Amperometric NO detection: The amperometric detection was performed by a World Precision Instrument, ISO-NO meter, allowed the direct monitoring of NO photorelease both from the polymer and the complexes.

The graphical visualization was obtained by a data acquisition system, with short response time (< 5 s) and sensitivity range 1 nM – 20 μM. The analog signal was digitalized with a four-channel recording system and transferred to a PC. Standard solutions of $NaNO_2$ with 0.1 M H_2SO_4 and 0.1 M KI were mixed to calibrate the sensor, according to the following reaction:

$$4H^+ + 2I^- + 2NO_2^- \rightarrow 2H_2O + 2NO + I_2$$

Irradiation was performed in a quartz cell (1 cm pathlength, 3 mL capacity), using a 100 mW continuum blue laser (λ_{exc} = 405 nm), in the same experimental conditions of the phodecaging assays. NO measurements were carried out under gentle stirring of the

samples, with the electrode positioned outside the light path in order to avoid NO signal artefacts due to photoelectric interference on the ISO-NO electrode.

NO photorelease quantum yields: The NO quantum yield Φ_{NO} was evaluated at λ_{exc} = 405 nm through the following formula:

$$\Phi = \frac{\Delta A \cdot V}{\Delta \varepsilon \cdot t \cdot I \cdot F}$$

ΔA is the variation in absorbance at 398 nm; V is the volume of the irradiated solutions; $\Delta\varepsilon$ at the same wavelengths was taken into account (10000 M^{-1} cm^{-1}); t is the irradiation time; I the intensity of the excitation light source, that had been calculated by potassium ferrioxalate actinometry; F is the fraction of absorbed light at the excitation wavelength (λ_{exc} = 405 nm) and at the initial time (t=0) and it is defined by ($1-10^{-A}$), where A is the absorbance at the excitation wavelength and at t=0.

Singlet oxygen detection: The NIR luminescence of $^1O_2$ at 1.27 mm results from the forbidden transition $^3\Sigma^-_g \leftarrow {}^1\Delta_g$. This steady-state emission was registered with the same spectrofluorometer as above equipped with a NIR-sensitive liquid nitrogen cooled photomultiplier, exciting the air-equilibrated samples with a 670 nm continuum laser (100 mW). The timeresolved emission of $^1O_2$ was probed orthogonally to the exciting beam of the same 532 nm pulsed laser as above, with a preamplified (low impedance) Ge-photodiode (Hamamatsu EI-P, 300 ns resolution) maintained at 196 °C and coupled to a longpass silicon filter (41.1 mm) and an interference filter (1.27 mm). The pure signal of $^1O_2$ was obtained as the difference between the signals in air and Ar-saturated solutions. The temporal profile of the luminescence was fitted to a single-exponential decay function with the exclusion of the initial portion of the plot, which was affected by scattered excitation light, fluorescence, and the formation profile of $^1O_2$ itself.

Heat detection: Photothermal experiments were performed by irradiating the samples (100 µL) in an NMR tube with a 808 nm continuous wave (CW) laser (ca. 6 W cm^{-2}) having a beam diameter of *ca.* 1.5 mm and detecting the temperature changes with a FLIR C3 thermal imaging camera. Pictures were edited using FLIR tools software and presented with a linear colour scale for temperature.

Fluorescence Quantum Yields: Fluorescence quantum yields (Φ_f) were determined using optically matched solutions at the excitation wavelength of compounds, and Fluorescein NaOH 0.1 M ($\Phi_{f\ (s)}$ = 0.98) as a standard through the following equation:

$$\Phi_f = \Phi_{f\ (s)}\ (I\ n^2/_{(s)} n^2_{(s)})$$

where $\Phi_{f\ (s)}$ is the fluorescence quantum yield of the standard; I and $I_{(s)}$ are the areas of the fluorescence spectra of compounds and standard, respectively; n and $n_{(s)}$ are the refraction index of the solvents used for compounds and standard. Absorbance at the excitation wavelength was less than 0.1 in all cases.

Laser flash photolysis: All of the samples were excited with the second harmonic of a Nd–YAG Continuum Surelite II-10 laser (532 nm, 6 ns FWHM), using quartz cells with a path length of 1.0 cm. The excited solutions were analyzed with a Luzchem Research mLFP-111 apparatus with an orthogonal pump/probe configuration. The probe source was a ceramic xenon lamp coupled to quartz fibre-optic cables. The laser pulse and the mLFP-111 system were synchronized by a Tektronix TDS 3032 digitizer, operating in pre-trigger mode. The signals from a compact Hamamatsu photomultiplier were initially captured by the digitizer and then transferred to a personal computer, controlled by Luzchem Research software operating in the National Instruments LabView 5.1 environment. The solutions were deoxygenated via bubbling with a vigorous and constant flux of pure nitrogen (previously saturated with solvent). In these experiments, the solutions were renewed after each laser shot (in a flow cell with a 1 cm optical path), to prevent photodegradation. The sample temperature was 295 ± 2 °K. The energy of the laser pulse was measured at each shot with a SPHD25 Scientech pyroelectric meter.

Size distribution: The size distribution of the SRB-β-CDs-NOPD complex were determined on a Zetasizer Nano ZS (Malvern Instruments Ltd, Malvern, UK).

Cell lines: The *in vitro* studies were carried out in a panel of three cancer cell lines, Hep-G2, ACHN, and MCF-7 (all from American Type Culture Collection, ATCC, Manassas, VA, USA). Cell lines were chosen according to SRB clinical applications. Cell lines were maintained in Dulbecco's Modified Eagle's medium (DMEM, Sigma-Aldrich, Milan, Italy) supplemented with 10% fetal bovine serum,

and 1% penicillin/streptomycin. Cells were cultivated in 75 cm^2 culture flasks (EuroClone, Milan, Italy) at 37°C in a humidified atmosphere of 95% air, 5% CO_2. The trypsin-EDTA solution (Sigma-Aldrich, Milan, Italy) was used to detach cells from the bottom of the flask.

Dark and phototoxicity *in vitro*: For the *in vitro* PDT experiments, SRB was loaded into β-CDs by magnetically stirring the SRB film with a serum-free culture medium solution of the branched polymer.

Cells were seeded as previously described and, after 4 hours of incubation with SRB-free or SRB-loaded into phototherapeutic β-CD branched polymer, they were washed once with PBS, and irradiated in PBS with a 150 WXe lamp through a cut-off filter at λ_{exc} 350 nm. Immediately after irradiation, the PBS was replaced with complete medium and cell plates were brought back to the incubator. Cell viability was measured with the MTT test after an additional 24 hours. Results were reported as percentage of viability versus untreated controls.

The SRB free base (molecular weight [MW] 464,8 g·mol-1) was dissolved in 100% DMSO (Sigma-Aldrich, Milan, Italy), and diluted with serum-free medium to the desired concentration with a final DMSO concentration of 0.1%. Control cultures received equal amount of DMSO as solvent control.

The SRB cytotoxic effect in the dark was measured with the MTT (3-(4,5-Dimethyl-2-thiazolyl)-2,5-diphenyl-2H-tetrazolium bromide) assay. Cells (1×10^4) were seeded in in 96-well flat bottom plates and incubated for 48 hours until the monolayer reached a confluency of approximately 80% and then incubated with scalar concentration of SRB diluted in serum-free medium for 24 or 4 hours. The short-term incubation of 4 hours was followed by an additional 24 hours of cell growth in drug-free medium with serum (4h + 24 h). After the indicated time, the medium was replaced with 180 µL of medium and 20 µL of MTT solution (stock solution at 5 mg/mL) and the wells incubated for 3 hours at 37°C. In this condition, mitochondrial dehydrogenases of viable cells conversed the tetrazolium ring of MTT into formazan crystals that were solubilized in 100 µL of DMSO. The absorbance was measured at 550 nm with a Varioskan™ LUX multimode microplate reader (Thermo Fischer Scientific). The cytotoxicity index was calculated using the untreated cells as a negative control (100% viability) and the IC_{50} was extrapolated from the dose-response graph by nonlinear regression analysis using GraphPad Prism software (San Diego, CA).

Localization of the polymer and the complexes through fluorescence microscopy: For localization of the polymer and the complexes inside the cells through the fluorescent properties of the β-CDs-

FITC conjugate, the cells were cultured in glass coverslips inserted into 24- or 6-well culture dishes. The medium was removed and replaced with SRB-β-CDs branched polymer complex for 4 hours. Then cells were first washed with PBS, then fixed with 4% formaldehyde. Images were acquired by microscope (Zeiss Axioplan, Carl Zeiss, Milan, Italy) equipped with a camera (Axicam, Carl Zeiss, Milan, Italy), with λ_{exc} = 450 nm and λ_{em} = 480 nm.

2.2 A Fluorescent β-Cyclodextrins Polymer Encapsulating Sorafenib and Releasing Nitric Oxide Under Visible Light

2.2.1 Introduction

It was designed and characterized a novel multimodal anticancer, aimed to the enhancement of the chemotherapeutic action of the basically water insoluble SRB. The drug was combined to a novel, branched, water-soluble β-CDs polymer (PolyCDNO) with exceptional abilities to incorporate hydrophobic guests and that releases NO and emits green fluorescence upon strict control of light excitation.

In particular, PolyCDNO (MW ca. 420 kD) contains ca. 2.4% (*w/w*) of NOPD and 0.05% (*w/w*) of a fluorescein isothiocyanate (FITC) moiety, exploited as a fluorescent label for imaging the NO photodecaging (see Figure 8) [90].

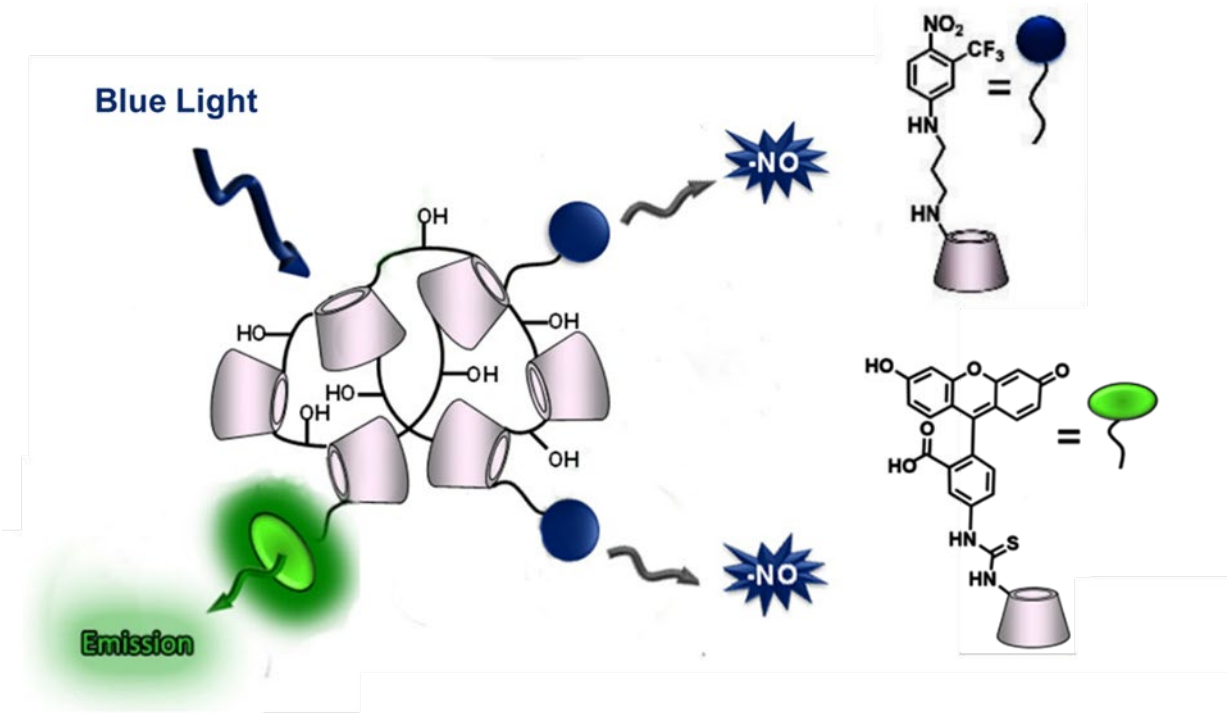

Figure 8: Schematic representation of the fluorescent β-CDs polymer, functionalized with a suitable nitro-aniline derivate as NOPD and a FITC moiety as a fluorescent tag.

A 4-nitro-3-(trifluoromethyl)aniline has been chosen as suitable NOPD [86]. It works like other sterically hindered nitro-derivatives [87] which, under light stimuli, can photorelease NO through a

nitro-to-nitrite rearrangement, the cleavage of the O-NO bond and the generation of a phenoxy radical as a key intermediate (see Figure 9).

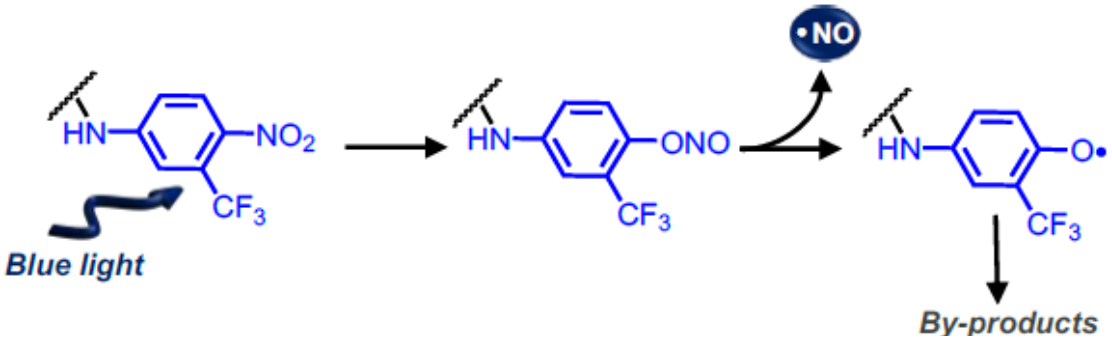

Figure 9: Mechanism of the photochemical NO release from the NOPD unit.

The FITC moiety and the NOPD can be photoexcited both in a simultaneous or selective way: the employment of green and/or blue light, respectively, can lead to their parallel activation, which results in the regulated green fluorescence emission for imaging and/or in the NO release for therapy [86].

2.2.2 Solubility of Sorafenib within the polymer and size distribution

PolyCDNO was employed to supramolecularly assemble SRB (see Figure 10).

As already discussed (see Introduction), β-CDs branched polymers represent a very appealing class of nanocarriers for water-insoluble guests encapsulation [88] and have extensively been used to integrate photoactivatable small molecules and deliver them into cancer cells [89–93].

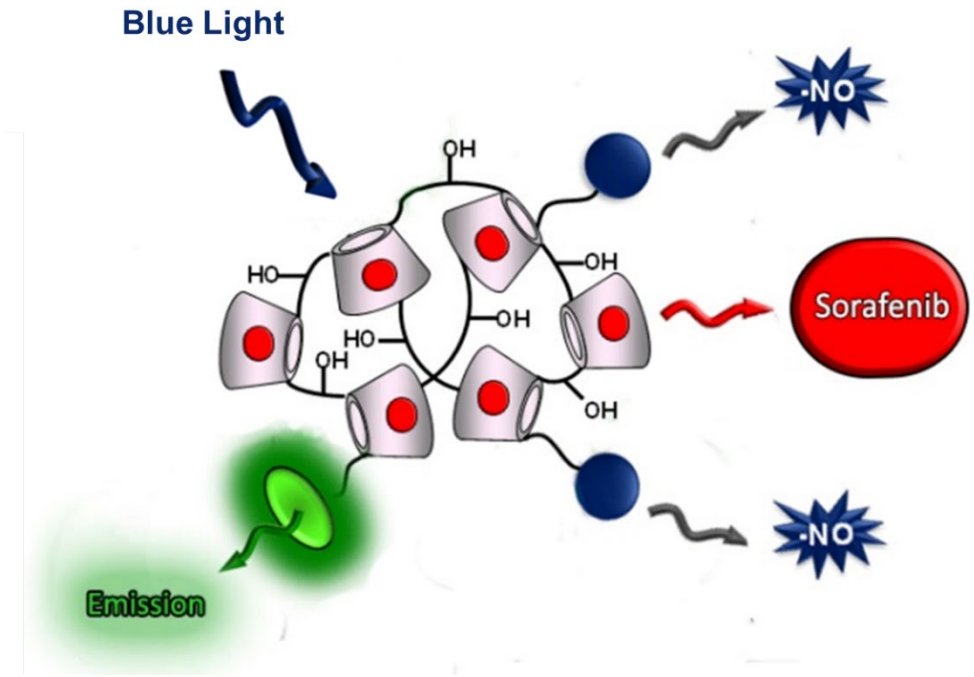

Figure 10: Schematic representation of the complex, formed by the fluorescent β-CDs polymer, functionalized with an NOPD and a FITC moiety, englobing SRB.

PolyCDNO absorption spectrum is dominated by two main different bands: the one of the NOPD falling in the blue region, with a maximum at *ca.* 400 nm, and the other weak shoulder in the green region at *ca.* 500 nm belonging to the FITC chromophore. These spectral features make it ideal to spectroscopically study the encapsulation of SRB, whose absorption profile in methanol (MeOH) displays the main band with a maximum at 265 nm, in a wavelength range where the absorption of the polymer is negligible (see Figure 11 A).

A preliminary analysis was performed in order to evaluate the largest quantity of drug that could be encapsulated within the polymer. As above mentioned, SRB is a poorly water-soluble drug (10 ng/mL) [94].

SRB films had been prepared by employing MeOH solutions of the drug at different concentration, up to 22.2 µg/mL, and by lately evaporating the solvent. They were let stir with a 1 mg/mL polymer aqueous solution, and the absorption spectra of the different samples were recorded. It was noted that the absorbance values at 265 nm increased, as a proof of the formation of a PolyCDNO/SRB host-guest supramolecular complex. A limiting value of 18 µg/mL was found to be suitable for the total solubilization (see Figure 11 A and B).

It is worthwhile noting that the absorption bands of the NOPD and FITC were only slightly affected by SRB encapsulation, suggesting a negligible interaction between the drug and both these chromophoric units in the ground state. On the other hand, a slight red-shift of the absorption maximum of SRB, compared to that one in MeOH, was observed, in agreement with its localization in an environment with different polarity.

As the inset in Figure 11 B shows, the solubilization of SRB within PolyCDNO was visible even at naked eye, by comparing the suspension of SRB in water (a) and the very clear aqueous solution obtained in the presence of the polymer (b). The absorption spectra remained unvaried in intensity and position for several weeks, accounting for good stability of the supramolecular assembly.

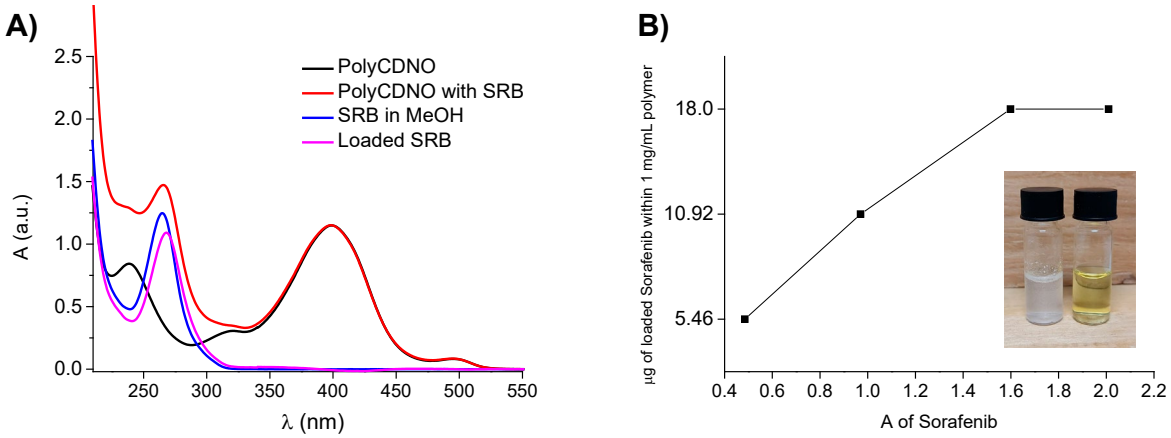

Figure 11. A) Absorption spectra of the solution of SRB in MeOH employed for the preparation of the SRB film (22,2 µg/mL); the 1 mg/mL aqueous solution of PolyCDNO and of its complex formed with SRB; the effective quantity of loaded SRB (18 µg/mL); (pathlength= 1 cm). **B)** Solubility curve of SRB within a 1 mg/mL aqueous solution of PolyCDNO.

The amount of free SRB in equilibrium with the complexed drug was evaluated in order to estimate the extent of SRB complexation within the polymer. To this purpose, the PolyCDNO/SRB samples were centrifuged through a polyethersulfone membrane with a MWCO (Molecular Weight Cutoff) of 5000 Da, exclusively permitting the permeation of the only free SRB; the permeate was then analyzed through HPLC. Poly-CDNO/SRB samples were analyzed with 1.5 and 18 µg/mL drug content: in any case, an amount as high as ca. 80% did not permeate through the membrane due to the complexation with the polymer, evidencing that, independently from its concentration, in the adopted conditions SRB prevails in the complexed form. The permeated amount was ca. 0.3 µg/mL, a value which is reasonably explicable by the low solubility in water. The complexation trend did not undergo any significative changes in cell culture medium (79.3% and 79.9% at 1.5 and 18 µg/mL,

respectively, of free SRB were englobed within the polymeric scaffold), suggesting that the presence of amino acids, vitamins, inorganic salts and glucose does not alter the extent of complexation in the conditions adopted for cell studies.

Size distribution curves of the SRB/polymer were collected at different drug concentrations (see Figure 12). It emerges from the graph that the β-CDs polymer maintains the polydispersity even when SRB is complexed, independently of the amount of the included drug. The graph showed the presence of two populations centered at *ca.* 10 nm and *ca.* 110 nm. The slight shift to lower mean values for the complex indicates a rearrangement of the polymeric network upon noncovalent bounding with SRB. It should be added that the polydispersity may be attributed to the synthetic conditions. It had been preliminary ruled out that the largest population could be ascribable to the aggregation of the smallest one, by observing that the addition of ethanol, which is supposed to discourage the host-guest interactions formation between the nitroaniline moiety and the CD cavity, did not modify the size trend. The polydispersity may be due to the higher solubility of the β-CDs than of β-CD-NOPD monomers in the polymerization solvent, resulting in two different populations: the one arising from an initial β-CDs crosslinking and the other one from a delayed β-CD-NOPD polymerization.

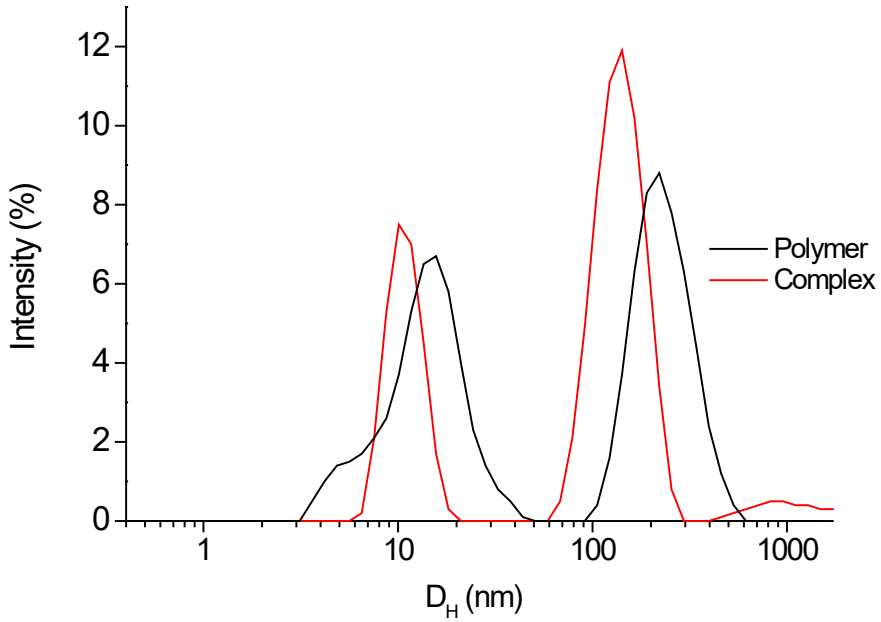

Figure 12: Size distribution curves of the aqueous solutions of SRB/β-CDs complex (SRB= 18 μg/mL within a 1 mg/mL of PolyCDNO) and of the polymer (1 mg/mL) alone.

2.2.3 Release of Sorafenib from the complex

The release of SRB from PolyCDNO was evaluated trough dialysis in physiological medium (PBS, pH 7.4) under sink conditions.

As shown in Figure 13, SRB release rate from the complex at different time points was lower than the one for free SRB at the same concentration, due to complex formation in the dialysis tube (the polymer could not cross the membrane). SRB release was complete after 2 days.

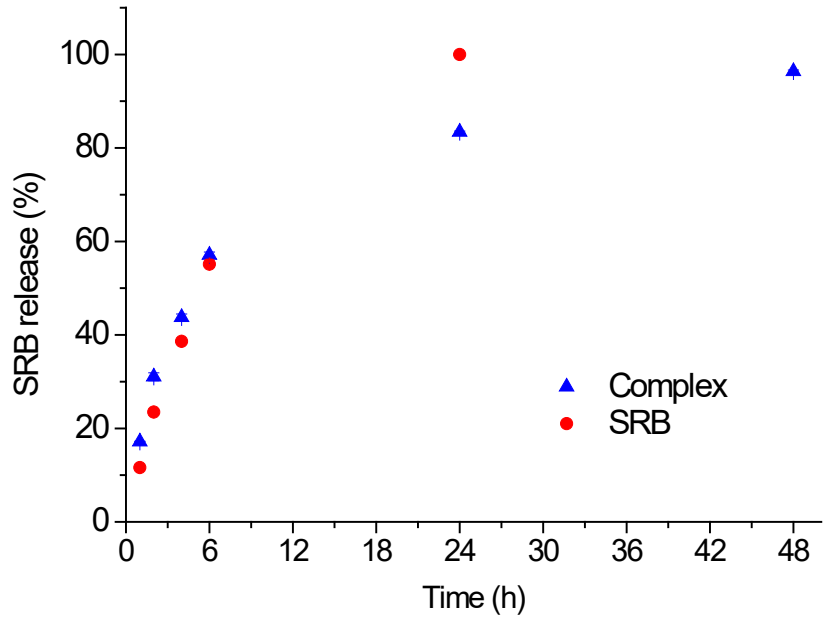

Figure 13. Release profile of SRB from the SRB/PolyCDNO complex assessed by dialysis in PBS at pH 7.4 and 37°C and free SRB for comparison purposes (SRB= 18 µg/mL, polymer 1 mg/mL). Data are reported as mean ± SD (n=3). SD were always lower than 1.65%.

2.2.4 Photochemical characterization

The preservation of the properties of the single functional components after their confinement in a restricted space is an essential requisite for a successful photo-chemotherapeutic combination. The efficiency and nature of the desired photoinduced process might, indeed, be affected by potential intermolecular processes occurring under light irradiation, possibly leading to unexpected photodecomposition pathways. SRB absorption falls at energy higher than that one of the NOPD and FITC, making any photoinduced energy transfer from the latter chromogenic units of the polymer to the drug thermodynamically unfeasible. Nonetheless, photoinduced electron transfer

processes among the same hosts could not be excluded. For this reason, the photochemical and photophysical properties of the complex were further investigated and compared with the ones of the free polymer.

The functionalization of PolyCDNO with the FITC moiety is fundamental for the tracking of the polymer in the cellular environment. It was demonstrated that the incorporation of the chemotherapeutic did not affect the emissive properties of the polymer. It is worthwhile reminding that the NOPD does not show any fluorescent properties and, as a consequence, the risk of an undesirable energy transfer process among the chromophores *via* the Förster Resonance Energy Transfer (FRET) is circumvented [86]. For the same reason, SRB itself is not able to act as a fluorescent quencher, either. Indeed, both the static and the dynamic features of the typical FITC green emission (see Figure 14 and relative inset) remained basically unvaried upon SRB encapsulation. The value of the fluorescence quantum yield remained $\Phi_f = 0.51$ and the fluorescence decay maintained a dominant component (*ca.* 80%) with a lifetime of *ca.* $\tau = 4.3$ ns, barely identical to the one of the free polymer [86].

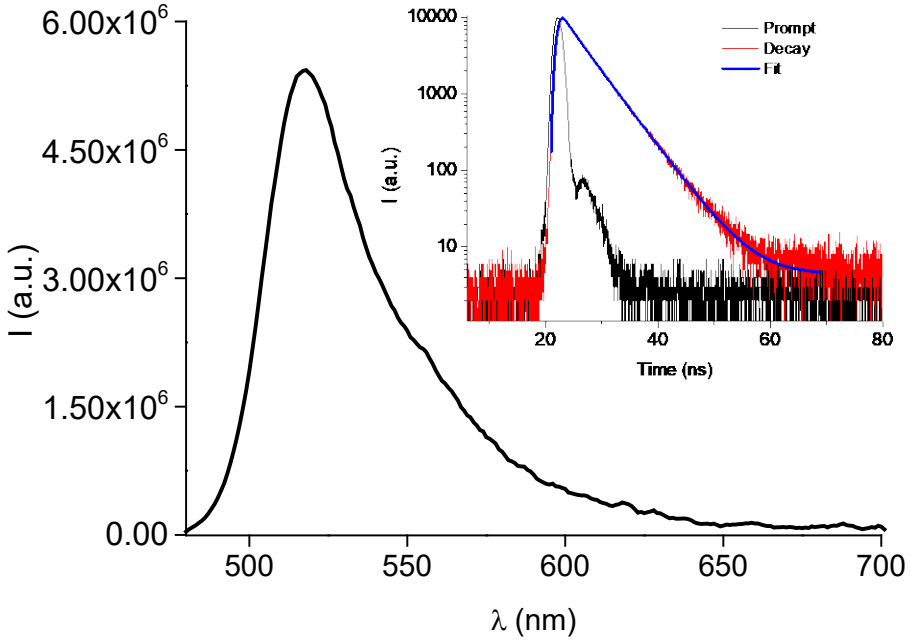

Figure 14: Fluorescence emission spectra of the 1 mg/mL aqueous solution of PolyCDNO and of its complex with SRB (18 μg/mL) (λ_{exc} = 470 nm). The inset shows the fluorescence decays and the related fitting of the same sample, recorded at λ_{em} = 530 nm.

2.2.5 NO photorelease

Aqueous solutions of the polymer (1 mg/mL) and of its complex with SRB were irradiated through a continuum laser with λ_{exc} 405 nm at 100 mW, to prove that the photoexcitation of the nitroaniline derivate, absorbing in the blue region, could lead to the release of NO [86].

The NO photodecaging from the polymer was clearly demonstrated by the bleaching of the NOPD absorption band at *ca.* 400 nm (see Figure 15 A). The absorption shoulder of the FITC moiety at *ca.* 500 nm did not display any affection due to the irradiation; this, once again, confirmed that every kind of biomolecular reactions among the NOPD and the CDs unit (*i.e.* photoreduction of the nitro group) or FITC is excluded: the only stable product is the phenol derivate, that absorbs in the UV region [95].

When the complex with SRB was irradiated, it was observed that the presence of the drug within PolyCDNO did not significantly affect the bleaching of the NOPD absorption band under irradiation (see Figure 15). Moreover, no variations were noticed in the absorption region of SRB (*ca.* 269 nm) and of FITC at 500 nm. These remarks ruled out any interference of the selected conventional drug with the NO photorelease and suggested that the chemotherapeutic, englobed within the CDs, had remained stable and had not been subject to any deterioration under blue light. Accordingly, the rate of the photobleaching was basically the same as that one observed for the free polymer (see Figure 15 C).

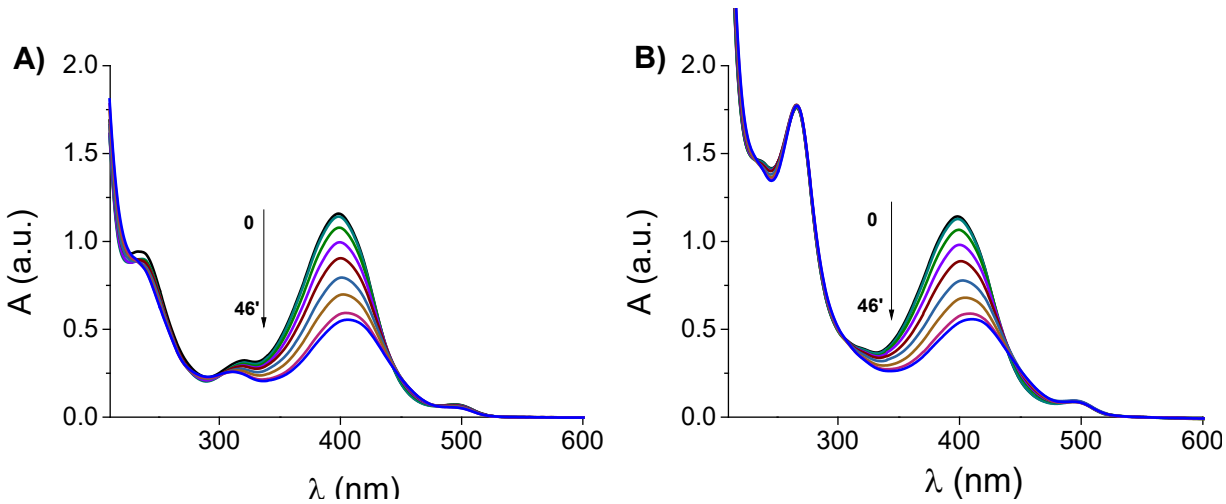

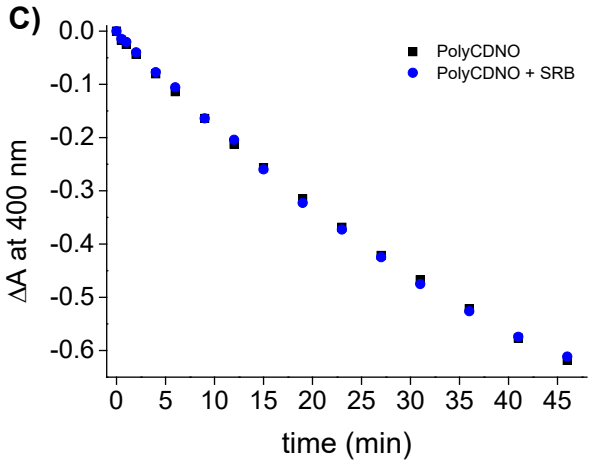

Figure 15. Absorption spectral changes of aqueous solutions of **(A)** 1 mg/mL PolyCDNO and **(A)** SRB-loaded (18 μg/mL) PolyCDNO, equally concentrated, observed at different times upon light irradiation with continuum laser λ_{exc} 405 nm (100 mW) (pathlength= 1 cm); **(C)** ΔA at 400 nm as a function of irradiation time upon light irradiation.

The real time detection of NO, obtained through an amperometric technique, allowed to monitor the photo-regulation of the NO release process from the complex and from the polymer upon photoirradiation (see Figure 16). Indeed, the radical release was detected only when light was turned on and it almost immediately stopped when the blue light stimulus was turned off; then, it started again only under photoirradiation. The NO release quantum yield Φ_{NO} was evaluated from the PolyCDNO/SRB complex: a value $\Phi_{NO} = 0.006 \pm 0.001$ was found, in perfect agreement with that already reported of the single polymer ($\Phi_{NO} = 0{,}005 \pm 0.001$) [86].

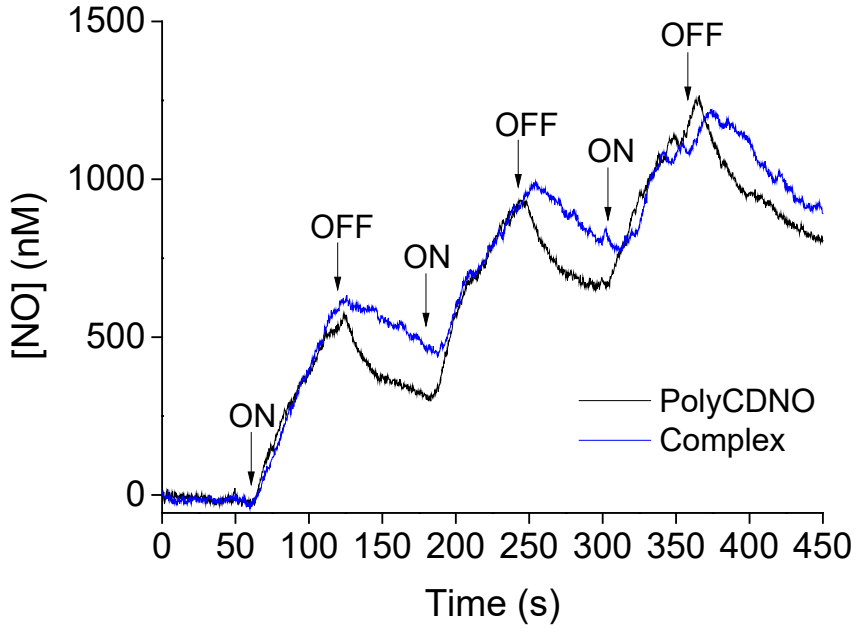

Figure 16: NO release profile of the aqueous solutions of 1 mg/mL polymer, with and without 18 µg/mL SRB, observed upon On/Off alternative irradiation cycles with a laser 405 nm at a power of 100 mW.

As reported in Figure 17, the emission spectra of the complex were recorded before and after the photoirradiation, together with the fluorescence lifetimes, in order to verify that the FITC moiety still permitted the visualization of PolyCDNO and that no environmental changes had involved the fluorophore.

The emission spectra did not show a significant change in intensity, even after prolonged irradiation times, confirming the absence of undesired intermolecular process between the FITC and the byproduct formed after the loss of NO from the NOPD moiety. Fluorescence decays too maintained the same value of *ca.* τ = 4.3 ns before and after the irradiation.

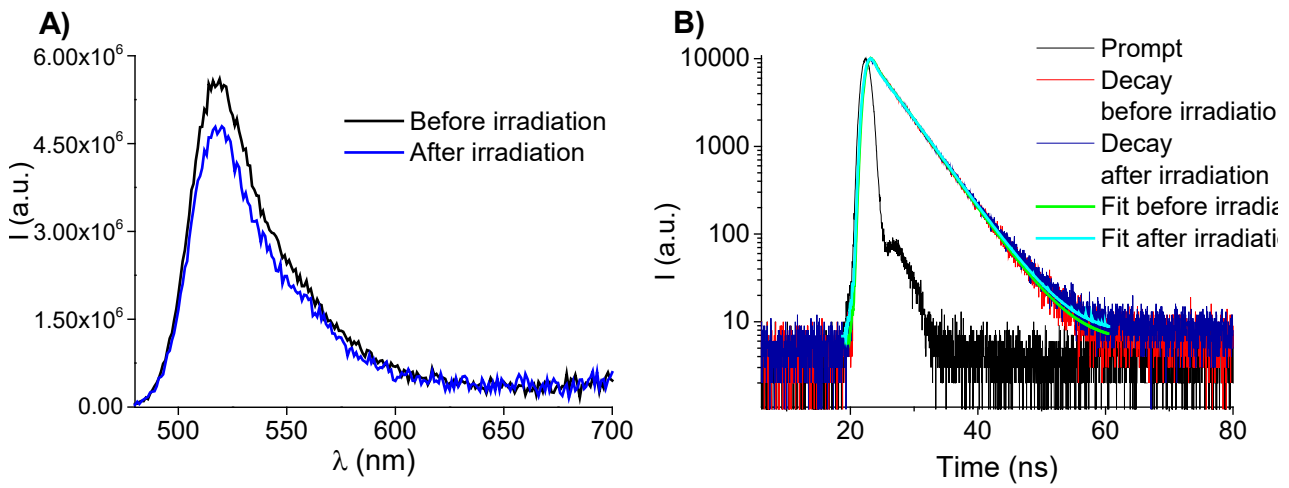

Figure 17: (A) Compared fluorescence spectra (λ_{exc} = 470 nm, slit = 1) and **(B)** compared fluorescence decays and related fitting (λ_{em} = 530 nm) of the aqueous solutions of 1 mg/mL polymer, with and without 18 µg/mL SRB, at the begin and at the end of the 46 minutes long light irradiation with continuum laser λ_{exc} 405 nm; 100 mW.

2.2.6 *In vitro* tests

Hepatocarcinoma cells line (Hep-G2)

The effect of the polymer (1 mg/mL) and of its complex with 1,5 µg/mL SRB was tested upon HCC cells (Hep-G2), both in the darkness and under Vis light stimuli. The results were compared with the lethality of free SRB at the same concentration and in the same conditions.

The SRB IC_{50} (Half Maximal Inhibitory Concentration) values were preliminarily evaluated by investigating the cell viability as a function of the concentration of the free SRB, in order to choose the most suitable concentration of the drug to be encapsulated within the CDs. Hopefully, an amount of drug sharply below the IC_{50} dosage could be employed to obtain good results on cells viability, thanks to the synergism with NO, exclusively released under blue light irradiation.

The cytotoxicity of free SRB was measured after 24 hours of exposure to increasing amounts of the antitumoral in serum-free medium. Cells reported a dose-dependent decrease of their viability, as measured by MTT assay. In these conditions, the SRB toxicity reported maximal levels, due to the absence of growth factors in culture medium.

Thus, it was investigated the effect of a short-term incubation (4 hours), followed by an additional exposure to complete medium for 24 hours. Data showed that, after the removal of SRB, the

presence of serum in culture media sustained cell proliferating activity, inducing an increase of the SRB IC_{50} up to 2-fold in Hep-G2.

The values of IC_{50} are reported in Figure 18 as extrapolated from the dose-response graph by nonlinear regression analysis.

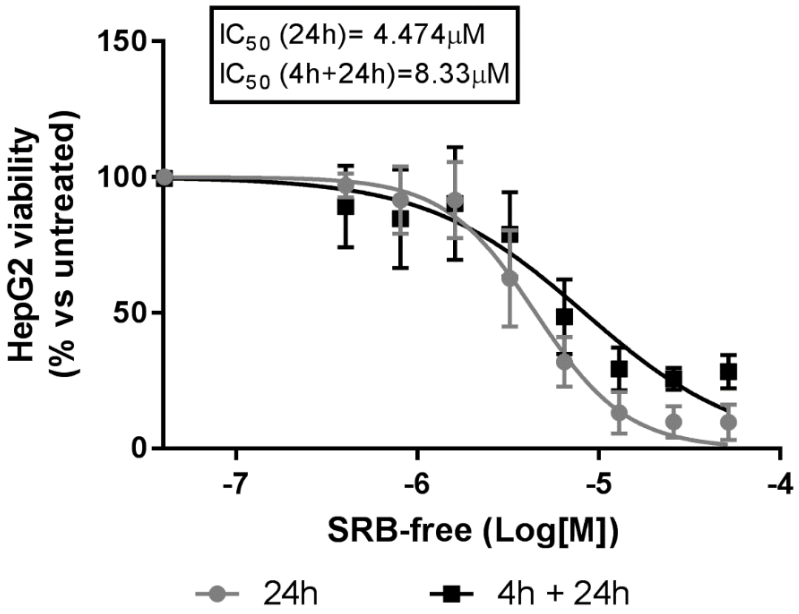

Figure 18: Hep-G2 viability (in % vs untreated cells) changing as a function of concentration of free SRB (Log[M]). The graph shows the IC_{50} values both after 24 hours of cell growth in drug-free medium with serum (24h) and after a short-term incubation of 4 hours, followed by an additional 24 hours of cell growth in drug-free medium with serum (4h + 24h).

According to these results, it was chosen to incubate cells for 4 hours before an additional 24 hours of cell growth, exploiting a SRB concentration which was more than half its IC_{50} (3,86 μg/mL, corresponding to 8.33 μM). Additionally, a recent work from our research group showed that PolyCDNO induces significant cell mortality due to the cytotoxic action of the NO generated only for irradiation times longer than 40 minutes [86].

To evaluate the lethality of the radical/antitumoral synergism, a dosage of 1.5 μg/mL (3.23 μM) of SRB was finally selected. Untreated cells, Hep-G2 treated with free SRB and with the antitumoral, at the same concentration, complexed within the polymer, were irradiated with a Xenon lamp, cutting off UV-light, under λ_{exc}= 350 nm.

Cells were irradiated for 40 minutes; MTT assay was performed 24 hours after the irradiation. The experiments were performed using DMEM as culture medium (base formulation; high level of glucose) and with no serum.

The impact of the complex over the tumoral cells was surprising. As shown in Figure 19, the untreated cells (Control) gave no mortality both in the dark and under Vis light, excluding any photothermal effect due to light irradiation. SRB displayed its own antitumoral properties in any of the experimental conditions, determining the mortality of about 20% of the cells. The polymer determined no decrease in cells viability in the dark, but, after the irradiation, the release of NO from the NOPD-functionalized CDs led to the death of more than 20% of the treated cells.

However, the complex of the polymer with 1.5 µg/mL SRB gave the most promising results. Indeed, in the darkness it was quite unoffensive, but after the 40 minutes long irradiation over the 95% of the hepatocarcinoma cells were killed off.

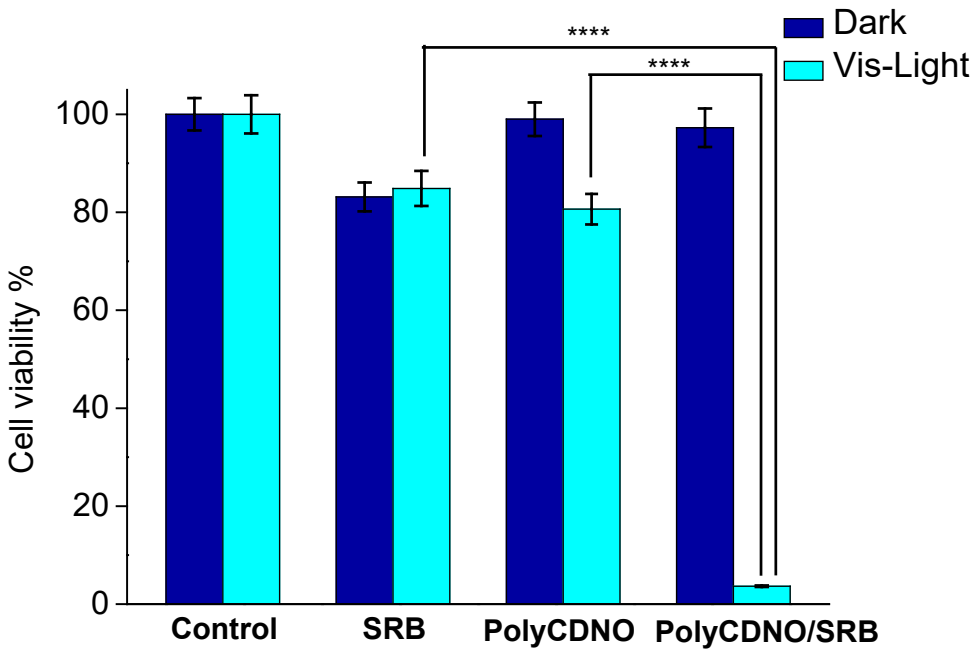

Figure 19: Cell viability in percentual of Hep-G2 cells in the dark and upon 40 minutes long irradiation (λ_{exc} > 400 nm). From left to right: control cells, not treated with the drug and/or the polymer; treated cells with 1,5 µg/mL SRB in its vehicle (DMSO); with aqueous solution of the polymer (1 mg/mL) and with its complex with 1,5 µg/mL SRB. (**** $p < 0.0001$; n = 3).

It is worth reminding that from the absorption analysis it was clear that SRB had not been affected by light, and, hence, could maintain its pharmaceutical activity as a MKI even after complexation

and irradiation. Moreover, it had been demonstrated that NO photorelease efficiency was not affected by the presence of SRB (see Figure 16). As a consequence, it was deducible that the synergy between the conventional drug and the free radical, individually used at not significantly toxic doses, was the responsible of such excellent results.

Since it has been demonstrated that SRB induces the generation of ROS in human HCC cell lines *in vivo* and *in vitro* in a dose-dependent manner [96], it is plausible to hypothesize that ROS, and in particular superoxide anion, reacts with NO, forming the highly cytotoxic peroxynitrite though a well-known diffusion-controlled process [97]. Biological studies addressed to gain insights into the mechanisms at the basis of these synergistic actions deserve forthcoming attention.

The cellular uptake of the PolyCDNO/SRB complex was explored through fluorescence microscopy, thanks to the preservation of the emissive properties of the FITC label after complexation of PolyCDNO with SRB and the fact that the complexation capability of PolyCDNO was not affected by the cell culture medium. Figure 20 shows representative fluorescence images from Hep-G2 cells, obtained after 4 hours of incubation with the complex and, for the sake of comparison, with the free polymer in FBS-free media excited at 488 nm and monitored in the green spectral region (500–580 nm). It was evident that the typical green emission of FITC arises from the cell cytoplasm, where both the complexed and the free polymer were present in the form of brighter aggregates.

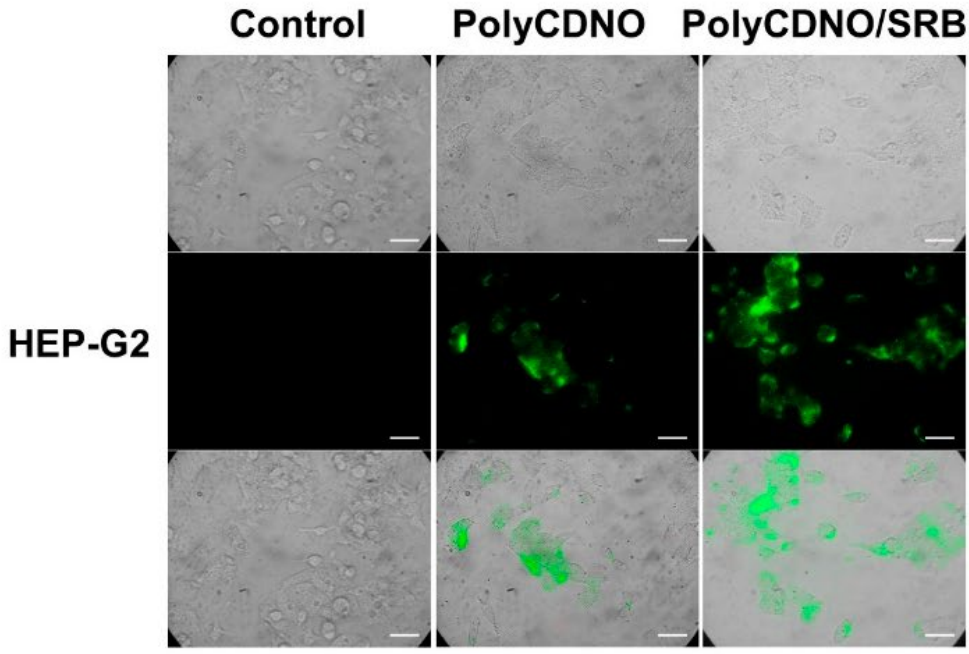

Figure 20: Representative transmission microscopy images (**upper panels**), fluorescence microscopy images of Hep-G2 cancer cells incubated for 4h with a solution a 1 mg/mL β-CDs polymer and a 1 mg/mL β-CDs

polymer complexed with SRB (**central panels**) and merged images (**lower panels**), collected in the range 500-580 nm and observed upon excitation λ_{exc} = 488 nm.

Breast cancer cells line (MCF-7)

The *in vitro* tests were repeated on breast cancer cells line (MCF-7), following the same protocol as above.

The IC_{50} was calculated and resulted in a very high value (see Figure 21), corresponding to 47,49 μM (22 μg/mL), after 4 hours of incubation and 24 hours of cells-growth.

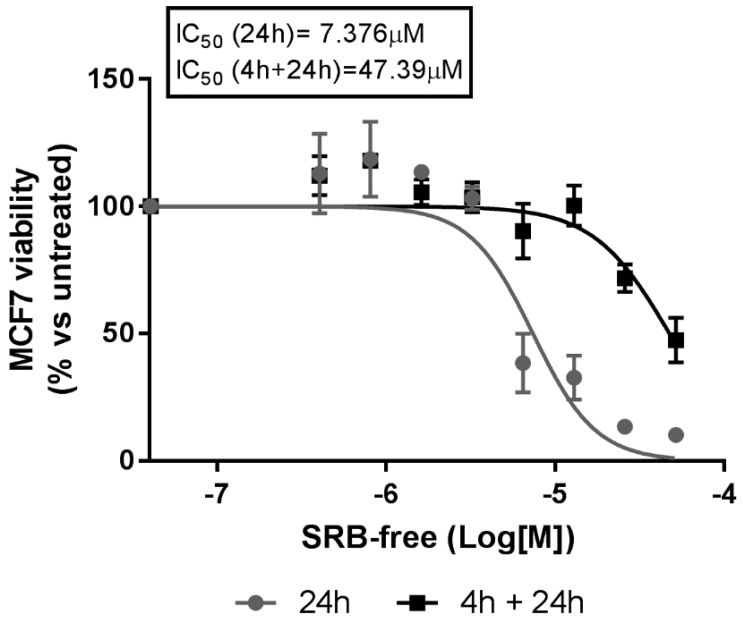

Figure 21: MCF7 viability (in % vs untreated cells) changing as a function of concentration of free SRB (Log[M]). The graph shows the IC_{50} values both after 24 hours of cell growth in drug-free medium with serum (24h) and after a short-term incubation of 4 hours, followed by an additional 24 hours of cell growth in drug-free medium with serum (4h + 24h).

Also in this case, 1.5 μg/mL of SRB was used for the complexation and the cell viability assays.

The results of the *in vitro* assays, reported in Figure 22, show that MCF-7 control cells were not affected, neither under light irradiation. SRB, at a concentration which, in this case, was very much lower the IC_{50} value, gave no mortality in any experimental condition. After the irradiation, the polymer eliminated more than the 20% of the cells, thanks to the photodecaging of NO. The complex

gave about a 30% of mortality in the dark, but only after the 40 minutes long irradiation the 80% of the tumoral cells were killed off, thanks to the NO/SRB synergy.

This latter may be considered an extraordinary result, if it is considered that only 6,81% of the SRB IC_{50} dosage was employed.

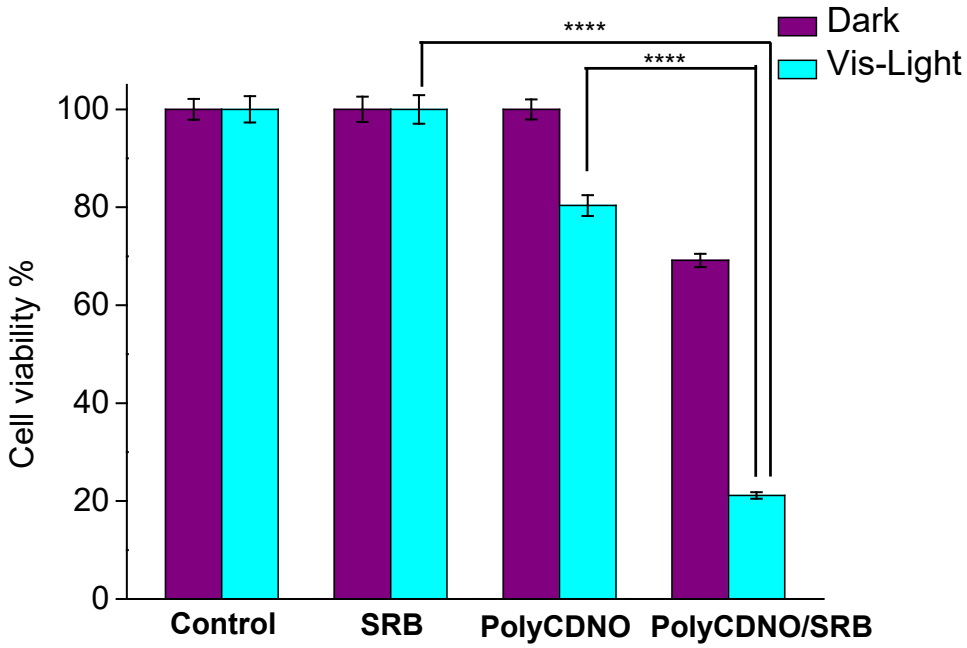

Figure 22: Cell viability in percentual of MCF-7 cells in the dark and upon 40 minutes long irradiation (λ_{exc} > 400 nm). From left to right: control cells, not treated with the drug and/or the polymer; treated cells with 1,5 µg/mL SRB in its vehicle (DMSO); with aqueous solution of the polymer (1 mg/mL) and with its complex with 1,5 µg/mL SRB. (**** $p < 0.0001$; n = 3).

Finally, the polymer and complex uptake within the MCF-7 cells was investigated through fluorescence imaging of the FITC chromophore (see Figure 23).

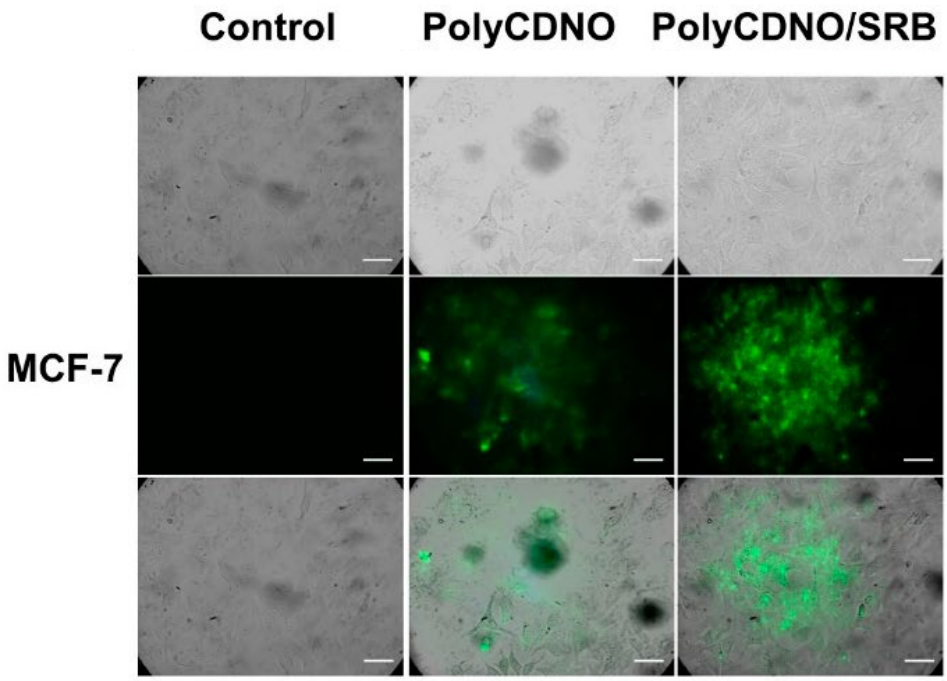

Figure 23: Representative transmission microscopy images (**upper panels**), fluorescence microscopy images of MCF-7 cancer cells incubated for 4h with a solution a 1 mg/mL β-CDs polymer and a 1 mg/mL β-CDs polymer complexed with SRB (**central panels**) and merged images (**lower panels**), collected in the range 500-580 nm and observed upon excitation λ_{exc} = 488 nm.

Adenocarcinoma cancer cells line (ACHN)

Finally, the therapeutic effect of SRB cooperating with NO was verified on renal adenocarcinoma (ACHN) cells.

16,32 µg/mL (35,21 µM) was found out to be the SRB IC_{50} value after 4 hours incubation and 24 hours cell-growing treatment (see Figure 24).

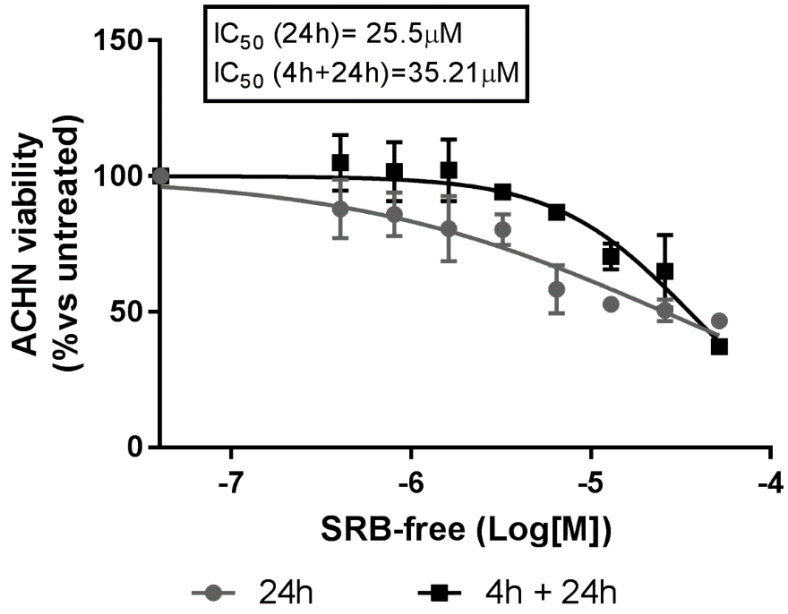

Figure 24: ACHN viability (in % vs untreated cells) changing as a function of concentration of free SRB (Log[M]). The graph shows the IC_{50} values both after 24 hours of cell growth in drug-free medium with serum (24h) and after a short-term incubation of 4 hours, followed by an additional 24 hours of cell growth in drug-free medium with serum (4h + 24h).

As outlined in Figure 25, the control cells, the untreated ones, showed a slight sensibility to the photothermal effect under the Xenon Lamp, probably due to a specific sensitivity of this cell line to irradiation light sources, as demonstrated by the comparable lowering of cell viability noted also in the control sample and according to the inability of SRB to absorb photons in the visible range. SRB in the dark eliminated about 74% of the treated cells and confirmed their modest photothermal influence under luminous stimuli. The polymer destroyed over the 40% of the renal cells under visible light.

Anyway, also in the case of ACHN, the cooperation of SRB with NO seemed to be the winning solution, considering that after the 40 minutes long irradiation, more than the 90% of the cells were killed off.

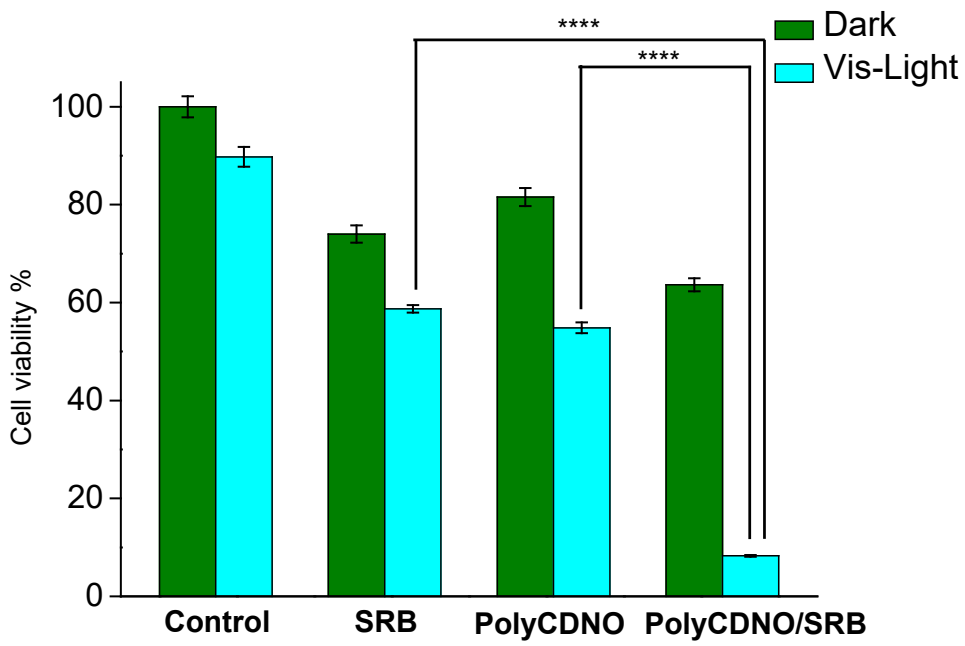

Figure 25: Cell viability in percentual of ACHN cells in the dark and upon 40 minutes long irradiation (λ_{exc} > 400 nm). From left to right: control cells, not treated with the drug and/or the polymer; treated cells with 1,5 µg/mL SRB in its vehicle (DMSO); with aqueous solution of the polymer (1 mg/mL) and with its complex with 1,5 µg/mL SRB. (**** $p < 0.0001$; n = 3).

Once again, PolyCDNO and its complex with SRB were visualized within the cellular environment by fluorescence microscopy (see Figure 26).

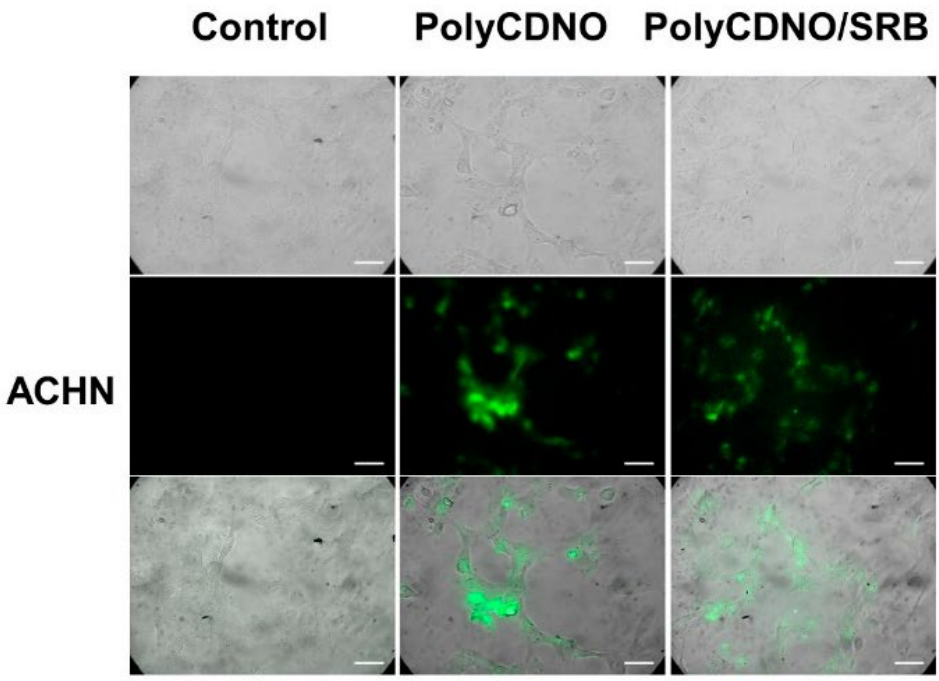

Figure 26: Representative transmission microscopy images (**upper panels**), fluorescence microscopy images of ACHN cancer cells incubated for 4h with a solution a 1 mg/mL β-CDs polymer and a 1 mg/mL β-CDs polymer complexed with SRB (**central panels**) and merged images (**lower panels**), collected in the range 500-580 nm and observed upon excitation λ_{exc} = 488 nm.

2.2.7 Conclusions

In this work, it was presented a viable strategy to enhance the anticancer activity of SRB by using low therapeutic doses, thanks to the combination with NO as an unconventional chemotherapeutic. This synergism between them is obtained through a biocompatible, water-soluble fluorescent β-CDs-based polymer, able to release NO and emit green fluorescence under the exclusive control of light stimuli. This multimodal polymer is able to effectively entrap SRB, significantly increase its solubility in aqueous medium, retaining its photochemical properties after the encapsulation and allowing SRB release in water. The host-guest supramolecular complex efficiently internalizes in different cancer cell lines, where it can directly be visualized thanks to the fluorescent properties of the polymer, and mostly localizes at cytoplasmatic level. From the toxicity experiments carried out over different cancer cells tumoral lines, with a SRB concentration much below the IC_{50} and with a suitable regulation of the NO amount released by light tuning, it emerges a remarkable synergistic effect between the conventional and unconventional chemotherapeutics, resulting in a significant rate of cell mortality.

To our knowledge, this is the first example showing the benefits of a nanoplatform combining a MKI such as SRB with a light-regulated NO release. In view of the increasing interest in the combination of NO with protein kinase inhibitors [14], and taking into account the very critical dependence of the biological effects of NO by its concentration [98–101], these findings may open up interesting avenues not only to potentiate the anticancer action of SRB but, in principle, to reduce its side effects given the low doses used.

2.3 A Supramolecular Nanoassembly of Lenvatinib and a Green Light-Activatable NO Releaser for Combined Chemo-Phototherapy

2.3.1 Introduction

The promising results obtained through the combination of SRB with PolyCDNO (see previous Section), encouraged the attempt to optimize this system through the employment of the much more biocompatible green light for NO release and inspired the extension of our approach to LVB, which has demonstrated to be even more efficient than SRB in unresectable hepatocellular carcinoma (see the corresponding section in Introduction). For this purpose, a ternary supramolecular nanoassembly was developed and photochemically evaluated, based on a water-soluble β-CDs polymer (Poly-CD) (see Figure 27) simultaneously hosting LVB (see Figure 7) and an already reported NOPD, henceforth Rhod-NO, using Rhodamine as a light harvesting antenna, absorbing in the green region and emitting in the red one [83].

PolyCD is a branched and water-soluble polymer, constituted by β-CDs units linked to each other through epichlorohydrin spacers. It has widely been proven to be well-tolerated *in vitro* and has broadly been exploited in literature as a suitable nanocarrier for several guests, including phototherapeutics, whose stability constants and payloads were enhanced in comparison with the unmodified β-CD monomers [91].

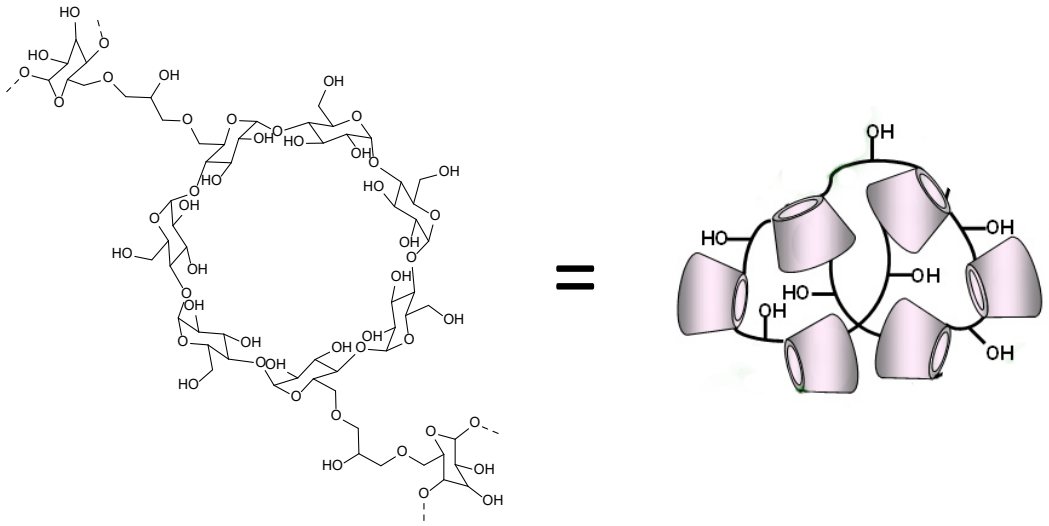

Figure 27. Schematic representation of Poly-CD, made of β-CD units.

Rhod-NO (see Figure 28) was recently reported by our research group as an intriguing, easily synthetized NOPD, based on Rhodamine as a light harvesting antenna [83]. The intense absorption and emissive properties in the green-orange spectral ranges, respectively, grant NO release with remarkable quantum efficiency, even under highly biocompatible photoexcitation [102] and real-time imaging in the cellular environment through fluorescence, as the latest scientific strategy of the so-called "See and Treat" approach suggests [16]. As Figure 28 shows, Rhodamine is covalently linked, through a suitable insulator spacer, to the NO-releasing moiety, which is a N-nitrosoaniline derivative of 4-nitro-3-(trifluoromethyl)aniline.

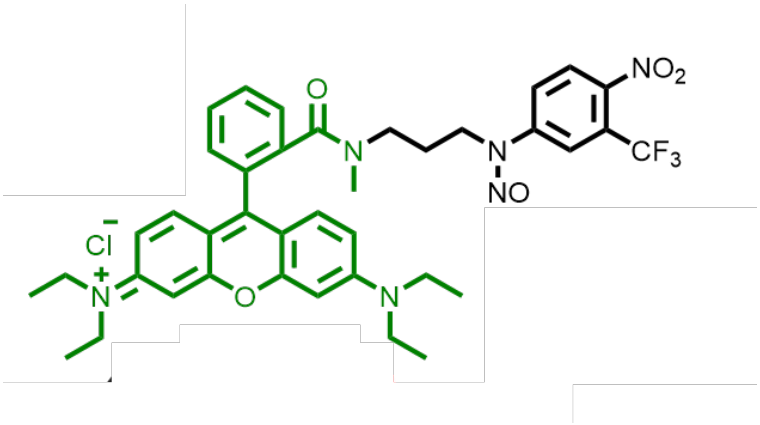

Figure 28. Molecular structure of Rhod-NO.

As Figure 29 schematizes, the excitation of the Rhodamine chromophore with the highly biocompatible green light triggers the uncaging of NO through a photoinduced electron transfer from the N-nitrosoaniline moiety (electron donor) to the excited state of the antenna (electron acceptor). A back-electron transfer follows, leading to the detachment of NO from the nitrosoamine; an anilino radical derivative is finally formed, stabilized by the electron drawing nitro and trifluoromethyl groups. The latter radical specie will be then transformed into a stable photoproduct *via* H-transfer from the solvent. Anyway, the typical orange fluorescence emission of Rhodamine, useful for imaging, is not precluded [83].

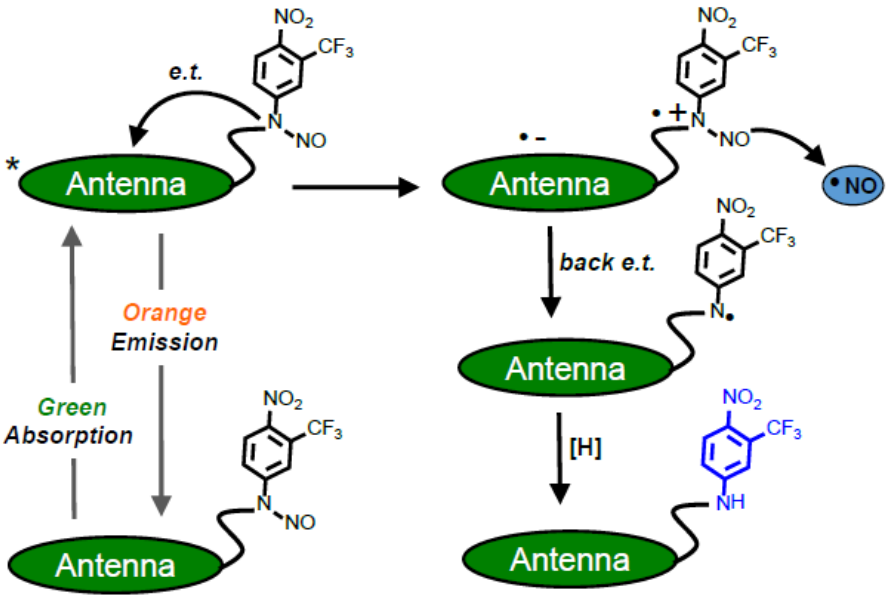

Figure 29. Proposed mechanism for the NO release triggered by green light [87].

On the basis of these promising basis, we have chosen Poly-CD to simultaneously assemble LVB as a conventional antitumoral drug and the fluorescent Rhod-NO as an unconventional chemotherapeutic agent, with the purpose of maximizing the therapeutic action and minimizing the side effects.

2.3.2 Solubility of Lenvatinib within the polymer

Since LVB is very poorly soluble in water, Poly-CD was employed to host it and to enhance its solubility in Phosphate Buffered Solution (PBS). Molar extinction coefficient of LVB was preliminary calculated both in MeOH, in the absence of CDs, and when assembled within Poly-CD (2 mg/mL) in PBS. ε_{241nm} was calculated to be equal to 72.350 M^{-1} cm^{-1} in the first case (Figure 30 A) and ε_{245nm}= 62.100 M^{-1} cm^{-1} within Poly-CD (Figure 30 B).

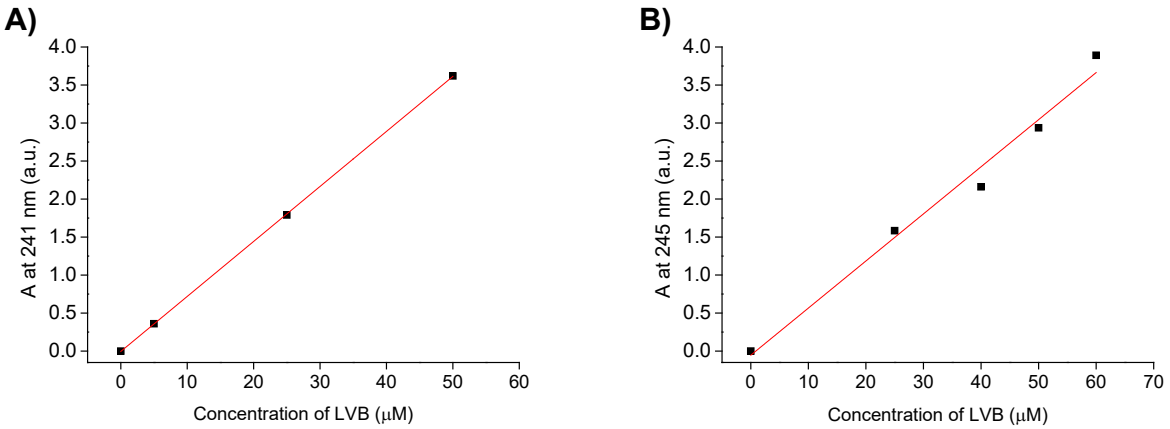

Figure 30. A) Absorbance at 241 nm of LVB solutions **in MeOH** at different concentrations, and relative slope to calculate the molar extinction coefficient; **B)** Absorbance at 245 nm of 2 mg/mL **Poly-CD** PBS solutions englobing LVB at different concentrations, and relative slope to calculate the molar extinction coefficient.

Secondly, the solubility of LVB was evaluated in PBS, both in the presence and in the absence of 2 mg/mL polymer.

As Figure 31 shows, a maximum value of 60 μM (25.5 μg/mL) was reached for the total solubilization in Poly-CD. Considering that only 4.1 μM (ca. 1.7 μg/mL) drug could have been solubilized in PBS, the solubility of LVB was increased more than one order of magnitude thanks to assembling properties of Poly-CD (see Figure 31 B).

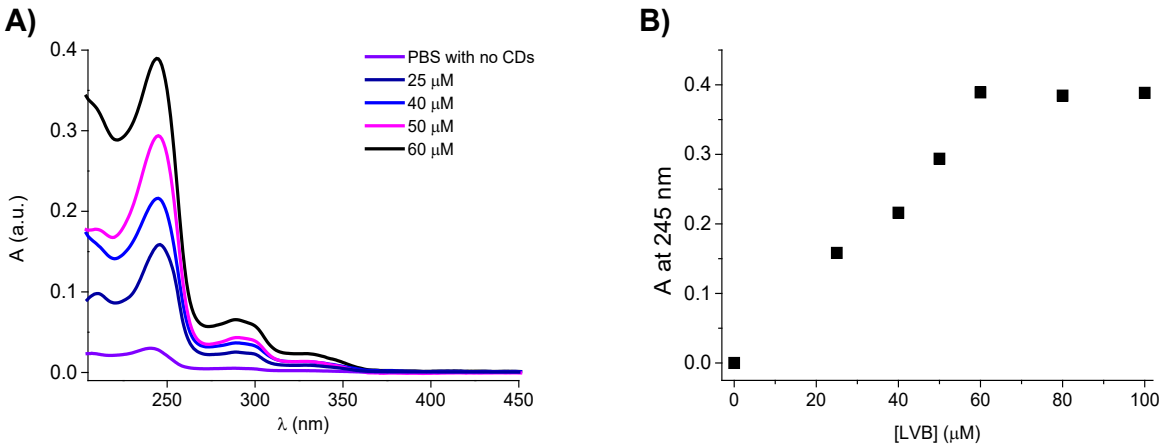

Figure 31. (A) Absorption spectra of the PBS solutions of LVB at different concentrations, in the presence or in the absence of the Poly-CD (2 mg/mL); (pathlength= 0.1 cm). **(B)** Solubility of LVB within Poly-CD (2 mg/mL) in PBS solution.

When LVB was encapsulated within Poly-CD, its absorption spectrum only showed a slight red-shift if compared to the one in MeOH solution (the maximum was shifted from 241 nm to 245 nm), due to the localization in an environment with different polarity. Nonetheless, the two absorption profiles were very similar, ruling out any intra-aggregation of the drug, which often occurs in its monomeric form (see Figure 32).

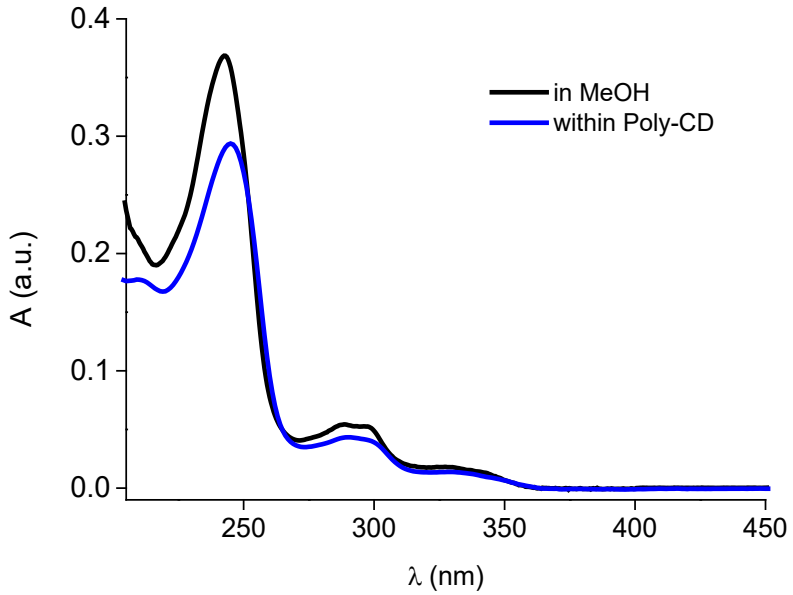

Figure 32: Absorption spectra of 50 µM LVB in MeOH and within Poly-CD (2 mg/mL) in PBS (pathlength= 0.1 cm).

The absorption profiles of the complexes, with LVB at different concentrations, remained unvaried over several days, attesting its stability under ambient conditions. For the sake of simplicity, only the data of 25 µM LVB are shown (see Figure 33 A). On the contrary, free LVB in PBS exhibited very unstable spectra over a few hours, with the absorption maxima gradually falling off over time (see Figure 33 B).

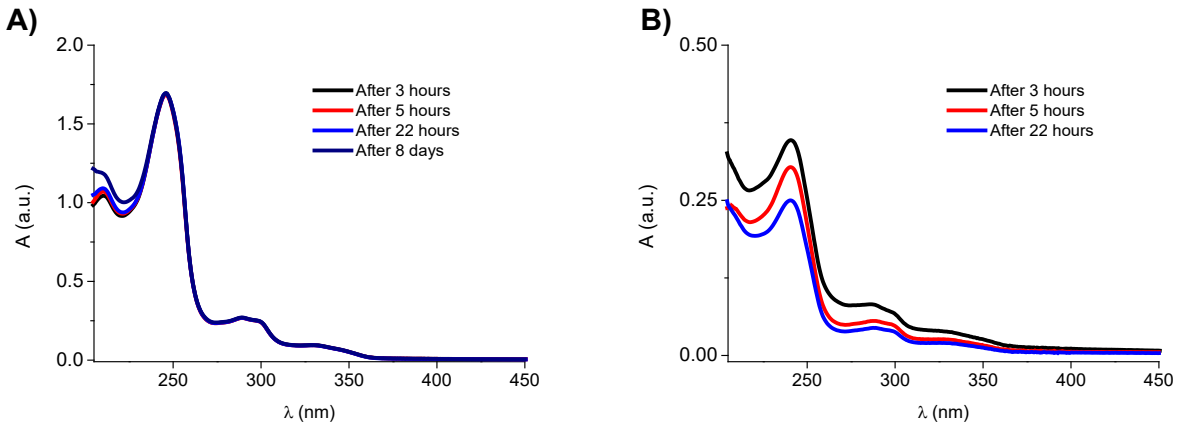

Figure 33: Absorption spectra of LVB (25 µM) in PBS solutions, both **(A)** in the presence and **(B)** in the absence of Poly-CD (2 mg/mL), recorded at different times; (pathlength= 1 cm).

2.3.3 Encapsulation of the NO Photodonor

The encapsulation of LVB within Poly-CD was not affected by the simultaneous assembling of Rhod-NO, which neither is water soluble.

Figure 34 shows the absorption spectrum of Poly-CD simultaneously hosting LVB and Rhod-NO, and, for the sake of comparison, the absorption profiles of the polymer loaded with the single guests at the same concentrations. The sum of the absorption profiles of the binary combinations perfectly matched the one of the ternary nanoassembly. The latter was dominated by two bands: the one of LVB, in the UV spectral range, and the other one related to Rhod-NO, absorbing in the green region. Since the drug absorption shoulder, with the maximum at *ca.* 245 nm, did not overlap the one of Rhod-NO, the selective photoexcitation of the NOPD with the biocompatible green light was granted.

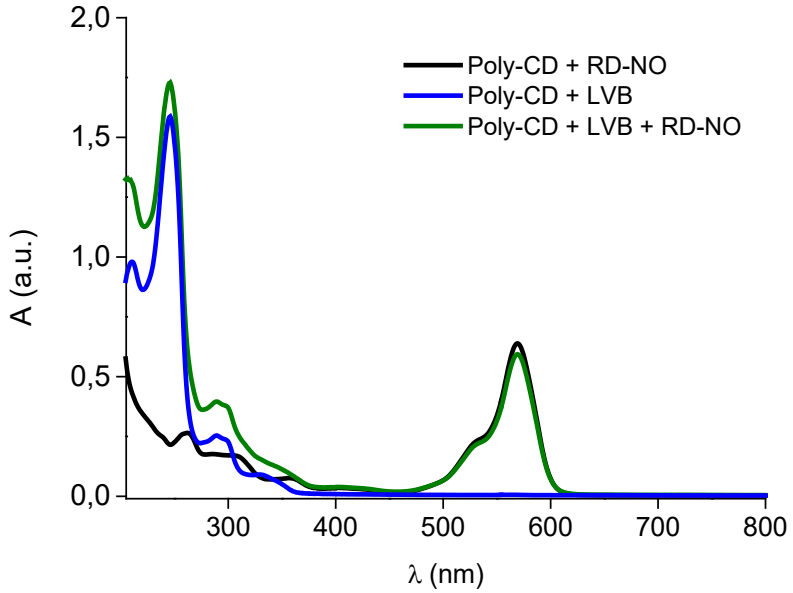

Figure 34: Absorption spectra of Poly-CD (2 mg/mL) loaded with only Rhod-NO (6 µM), with only LVB (25 µM) or with both components at the same concentrations, in PBS solutions; (pathlength= 1 cm).

Moreover, the presence of Rhod-NO gave no shift in the absorption maximum of LVB and vice versa, suggesting that the co-presence of the two compounds led to no significant interaction between them at the ground state and to no rearrangement of the guests within the polymeric scaffold.

2.3.4 Dynamic Light Scattering analyses

Dynamic Light Scattering (DLS) analyses of the ternary assembly sample (Poly-CD/LVB/Rhod-NO) showed an average hydrodynamic diameter of *ca.* 50 nm (see Figure 35), a value that perfectly matched with the ones of already reported host-guest complexes, based on the same polymer with different compounds [95-97].

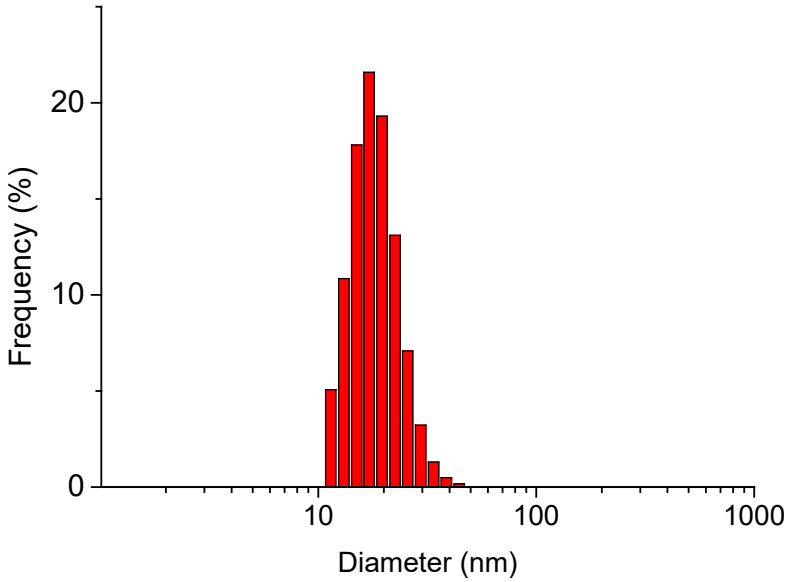

Figure 35: Intensity weighted hydrodynamic diameter distribution of the PBS solution of the Poly-CD (2 mg/mL) loaded with Rhod-NO (6 µM) and LVB (25 µM).

2.3.5 NO photorelease

PBS solutions of the binary and ternary supramolecular complexes of Poly-CD with Rhod-NO, alone or simultaneously hosted with LVB, were irradiated through a continuum laser with λ_{exc} 532 nm at 100 mW. It was proven that the selective photoexcitation of the NOPD, whose absorption falls in the green region, far from the absorption profile of LVB in the UV-spectral range, could be achievable.

Figure 36 A and B show the absorption spectral changes of Poly-CD/Rhod-NO and of Poly-CD/LVB/Rhod-NO, respectively, upon λ_{exc} 532 nm irradiation. In both the cases, the bleaching of the absorption shoulder at 291 nm was accompanied by the formation of another one at 397 nm, together with the isosbestic point at 348 nm, typical of a clean photochemical reaction. The two absorption profiles were almost identical and in agreement with that one already observed for free Rhod-NO in MeOH/H_2O [83]. As Figure 36 C demonstrates, the absorbance changes in the co-presence of LVB were almost identical for the Rhod-NO-loaded PolyCD in the absence of the drug. Moreover, the absorption shoulder of LVB did not display any affection, confirming the stability of the drug upon green light irradiation and excluding any bimolecular interaction between the guests.

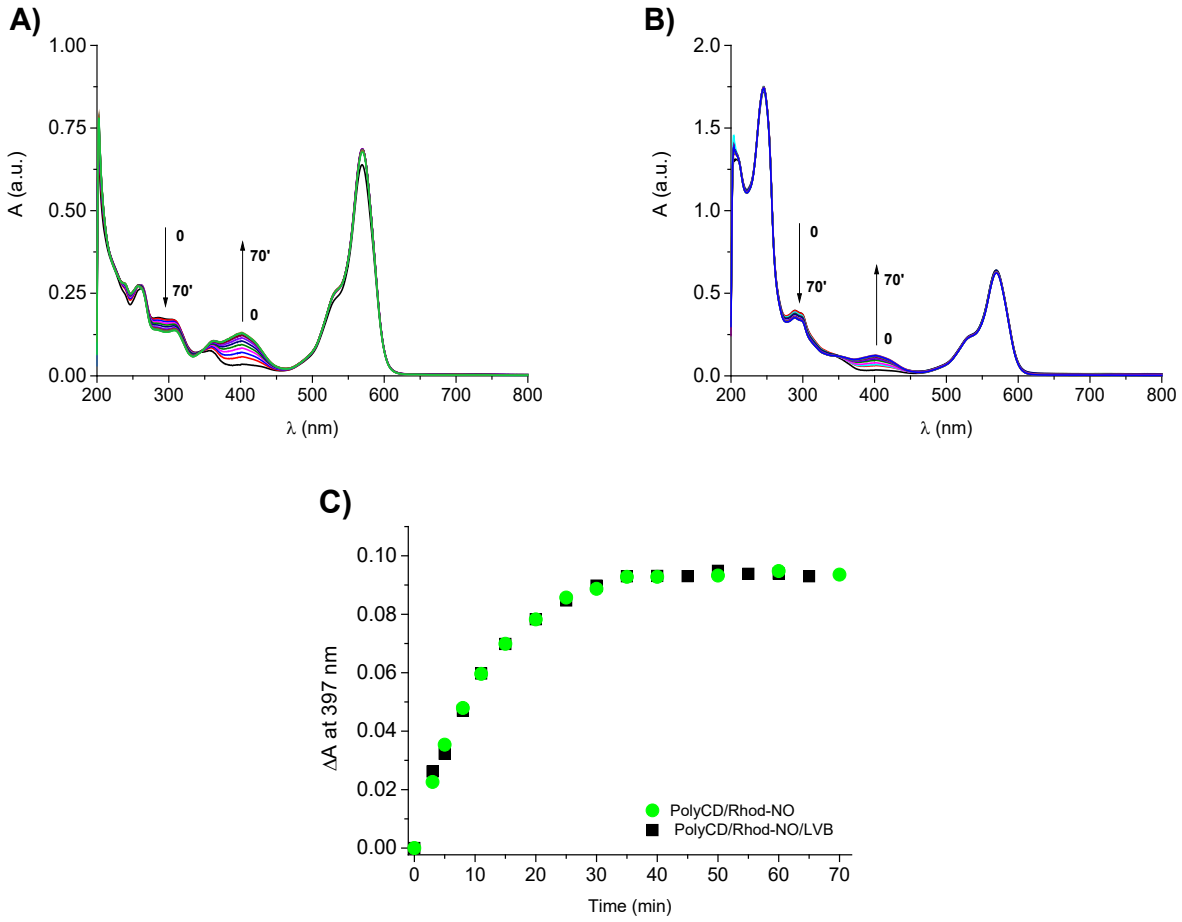

Figure 36: Absorption spectral changes of aqueous solutions **(A)** of Poly-CD (2 mg/mL) loaded with only Rhod-NO (6 µM) and **(B)** of Poly-CD (2 mg/mL) loaded with Rhod-NO (6 µM) and LVB (25 µM), observed at different times upon light irradiation with continuum laser λ_{exc} 532 nm (100 mW) (pathlength= 1 cm); **(C)** ΔA at 397 nm as a function of irradiation time upon light irradiation.

The NO photodecaging was verified through a real time amperometric detection (see Figure 37). The experiment was carried on Poly-CD PBS solutions, assembling Rhod-NO, with or without LVB, under continuous stirring.

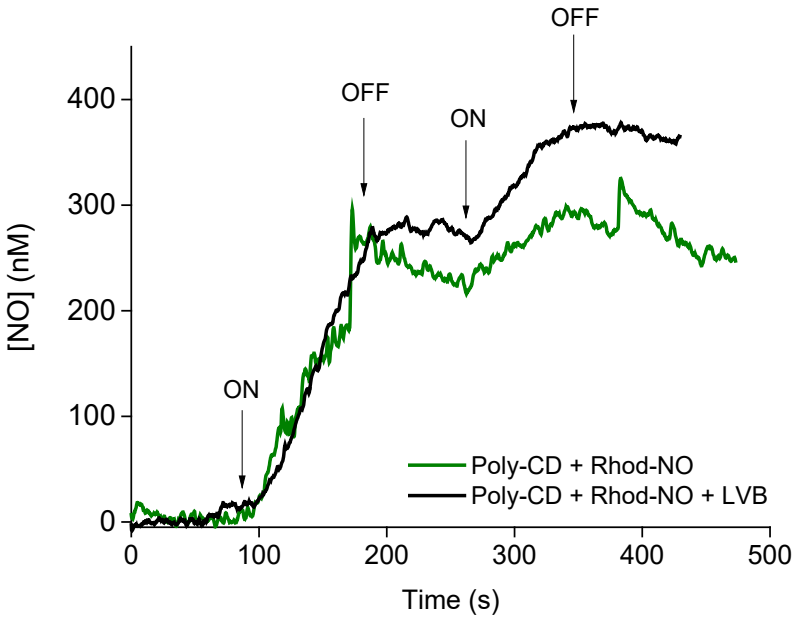

Figure 37: NO release profile of PBS solutions of Poly-CD (2 mg/mL) loaded with Rhod-NO (6 µM), both in the presence or in the absence of LVB (25 µM), observed upon On/Off alternative irradiation cycles with a laser 532 nm at a power of 100 mW.

It was possible to ascertain that the radical release was strictly controlled by light: NO was generated when green light was switched on and immediately stopped as photoexcitation was interrupted; then, it started again only under the luminous stimulus. Moreover, it was observed that the presence of the chemotherapeutic did not affect the NO generation efficiency, in agreement with the photochemical kinetics (see Figure 36 for comparison).

The NO photorelease efficiency was quantitatively calculated for Rhod-NO assembled within Poly-CD. A value equal to $\Phi_{NO} = 4x10^{-3}\pm0.0005$ was found out, *ca.* 4-fold bigger than the one of free Rhod-NO [83]. This evidence suggested that the polymer might play an active role in the radical photodecaging, providing abstractable hydrogens to the anilyl radical intermediate that leads to the NO generation. This would not be a novelty in literature, as the same mechanism is often reported for the decomposition of other similar nitroso-derivative NOPDs involving radical intermediates within polymeric scaffolds [84].

2.3.6 Emissive properties

Since the two guests, both LVB and Rhod-NO, display fluorescent features, which are essential for their tracking within cells, their emission spectra were recorded when singularly and simultaneously

hosted, in order to verify that their co-presence within Poly-CD did not affect the respective photochemical features.

When the solutions of Poly-CD containing LVB, alone or in combination with the NOPD, were excited at λ_{exc}= 290 nm, a broad emission band was observed at *ca.* λ_{em}= 380 nm (see Figure 38). The latter is ascribable to the drug, as it is confirmed by the emission spectrum of Poly-CD containing Rhod-NO, in the absence of LVB, in which the same band was not detectable. Only a slight decrease in the emissive intensity could be noted in the presence of the two chromophores, suggesting that Rhod-NO hardly affected the fluorescence of LVB.

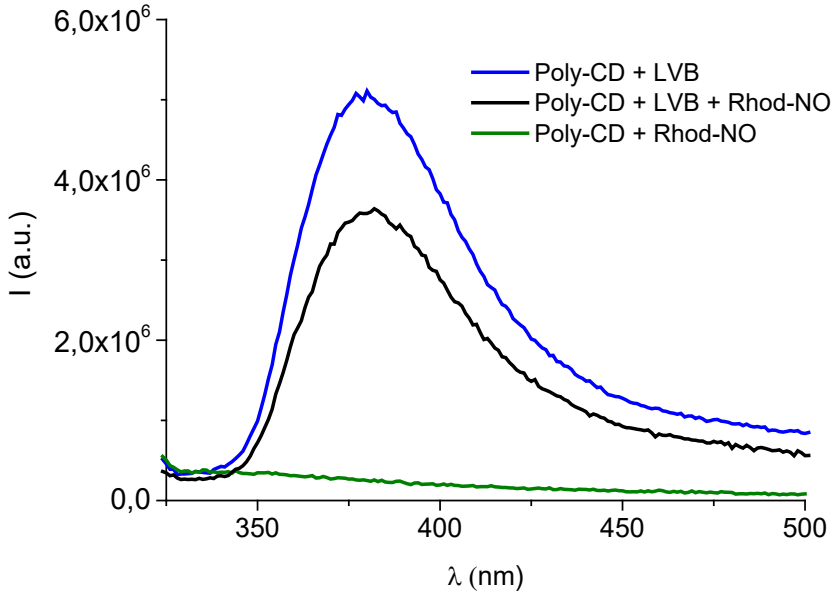

Figure 38: Emission spectra of Poly-CD (2 mg/mL) loaded with only Rhod-NO (6 µM), with only LVB (25 µM) or with both components at the same concentrations, in PBS solutions; (λ_{exc}= 290 nm).

As it is reported in Figure 39, the intensity of the Rhod-NO emission spectrum (with a maximum at *ca.* 590 nm) was almost identical when LVB was co-assembled, once again ruling out any interaction between the two guests.

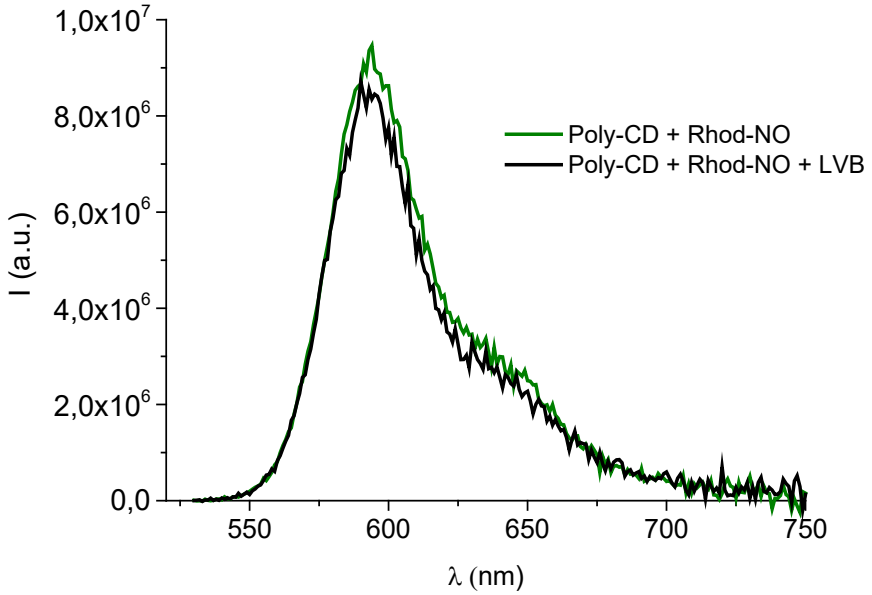

Figure 39: Emission spectra of Poly-CD (2 mg/mL) loaded with only Rhod-NO (6 µM) and with both LVB (25 µM) and Rhod-NO (6 µM), in PBS solutions; (λ_{exc}= 520 nm).

It was lastly calculated the Rhod-NO fluorescence quantum yield within the polymer, by considering as a reference an optically matched solution of Rhodamine B in EtOH, whose Φ_f is equal to 0.79 [104]. A value of Φ_f = 0.40 was found for the NOPD, unchanged in the presence of LVB, but almost 2-fold larger than the one observed for the free compound in MeOH/water solution (80:20 v/v) (Φ_f= 0.22) [83] (see Figure 38 A and B).

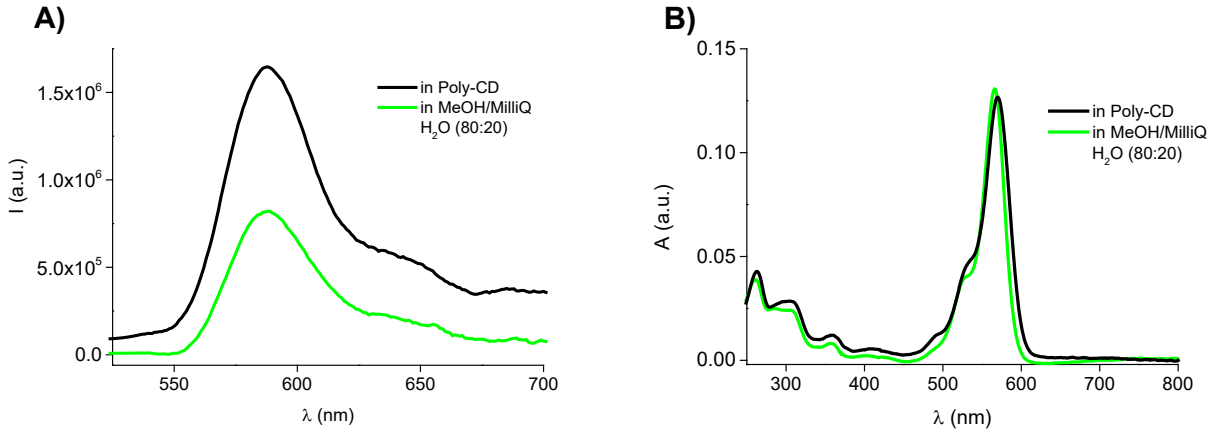

Figure 40: A) Emission and **B)** absorption spectra of Rhod-NO solutions, within Poly-CD in PBS (2 mg/mL) and in MeOH/milliQ H_2O (80:20 v/v), optically matched at λ_{exc}=510 nm.

The rise of the fluorescence efficiency may be explained by a constraint in the free rotation of the fluorophore, once hosted by the CDs polymeric environment, and therefore a reduction of the non-radiative decay pathway. This hypothesis is strengthened by the recorded fluorescence lifetime (see Figure 41), displaying a bi-exponential decay with τ_1 = 1.4 ns, just like it had been observed for the free guest [83], and a longer one with τ_1 = 3.6 ns and an higher relative weight, of *ca.* 60%.

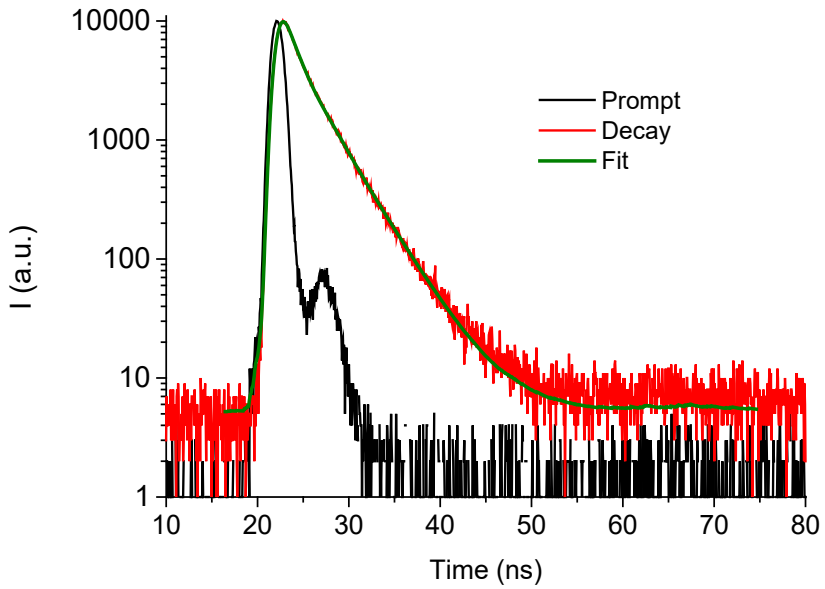

Figure 41: Fluorescence decay of Poly-CD (2 mg/mL) co-loaded with Rhod-NO (6 µM) and LVB (25 µM) and the related fitting of the same solution recorded at λ_{exc} = 455 nm and λ_{em} = 590 nm. T = 25 °C.

2.3.7 Spatial localization of the guests within the polymer and stability of the nanoassembly over time

As already highlighted, the photochemical and photophysical properties of the fluorophores embedded within the same polymer were well preserved even when co-encapsulated. This should be not an underestimated aspect, since photoinduced energy/electron transfer phenomena are very frequent between two guests localized in the same environment, and therefore potentially very close in space.

Nonetheless, in the above-explained Rhod-NO case, not only was the risk of losing the photochemical properties overcome, but they were even improved inside Poly-CD and safeguarded in the presence of LVB. It was deducible that the chemodrug was not able to quench the excited

states of the NOPD because, even if assembled by the same scaffold, the two chromophores were confined in different compartments of the polymer.

To prove this hypothesis, they were performed *ad-hoc* devised FRET experiments. LVB emission spectrum (with a maximum at *ca.* 380) nm does not remarkably overlap with the Rhod-NO absorption profile, which is an essential requisite for FRET phenomena to occur. Indeed, no FRET was detectable between them when LVB was excited in the presence of Rhod-NO. Nonetheless, this result could not give any indication about their spatial disposition within the polymer due to their spectral limitations.

For this reason, a third protagonist, a nitrobenzofurazan derivative (NBF), whose chemical structure is reported in Figure 42, was involved to deepen the issue and it was exploited as a suitable additional guest mediator.

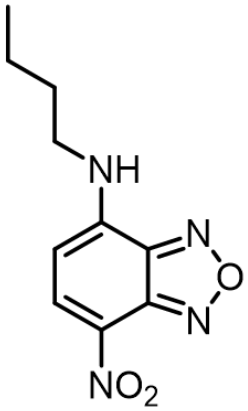

NBF

Figure 42: Chemical structure of NBF.

This hydrophobic compound perfectly fulfilled the desired requirements, since it can easily be englobed within the polymer and displays the right photochemical features to satisfy the pursued goals. LVB emission, indeed, overlaps the NBF absorption (see Figure 43 A); whereas the absorption of Rhod-NO is overlapped by the NBF fluorescence emission (see Figure 43 B.) These hallmarks make NBF a potential energy acceptor towards LVB and an ideal energy donor towards the NOPD.

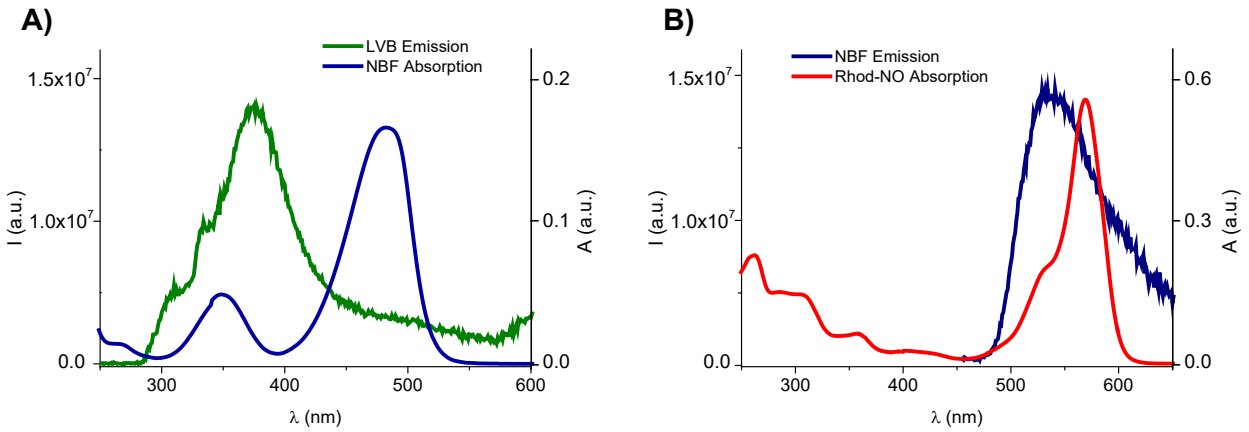

Figure 43: A) Absorption and emission spectra (λ_{exc} =241 nm) of the PBS solutions (pH= 7.4) of Poly-CD (2 mg/mL) englobing NBF (5 µM) or LVB (5 µM), respectively; **B)** Absorption and emission spectra (λ_{exc} = 445 nm) of the PBS solutions of Poly- CD (2 mg/mL) englobing Rhod-NO (5 µM) or NBF (5 µM), respectively.

A ternary nanoassembly was prepared, formed by Poly-CD englobing equally concentrated LVB, NBF and Rhod-NO. The absorption spectrum of the sample showed the typical spectral features of all the single guests (see Figure 44 A), ruling out any significant interaction among them in the ground state.

When LVB (potential energy donor) emission spectrum was recorded within Poly-CD/LVB/Rhod-NO/NBF nanoassembly, exciting at λ_{exc}= 241 nm, no changes in the emission spectrum were noted if compared to the emission profile obtained in the absence of NBF (potential energy acceptor). The lack in quenching of LVB emission suggested that the two chromophores were not close enough in space to let a FRET phenomenon occur between them (see Figure 44 B). In a second experiment, it was recorded the emission spectrum of the same complex, loaded with the three guests, by exciting at λ_{exc}=445 nm NBF (potential energy donor towards Rhod-NO). In this case, it was observed a sharp quenching in the emission of NBF and a correspondent noticeable increase in the Rhod-NO fluorescence. The spectrum was compared to the ones of the respective nanoassemblies with the single guests (see Figure 44 C): with either NBF (potential energy donor) alone (b in Figure 44 C) or Rhod-NO (potential energy acceptor) alone (c in Figure 44 C). The occurrence of a FRET phenomenon between them accounted for their spatial proximity within the polymeric structure.

To sum up, as the insets in Figure 44 B and C simplify, it could be deduced that NBF was located near the NOPD, but far from the chemodrug. Therefore, Rhod-NO and LVB were confined in different compartments of the polymer, far from each other even if assembled within the very same scaffold.

For this reason, the photophysical and photochemical properties of Rhod-NO were perfectly maintained in the presence of LVB, whose integrity and chemotherapeutic action were as well preserved even upon Rhod-NO photoexcitation, (i.e., not affected by any undesired photoinduced bimolecular processes).

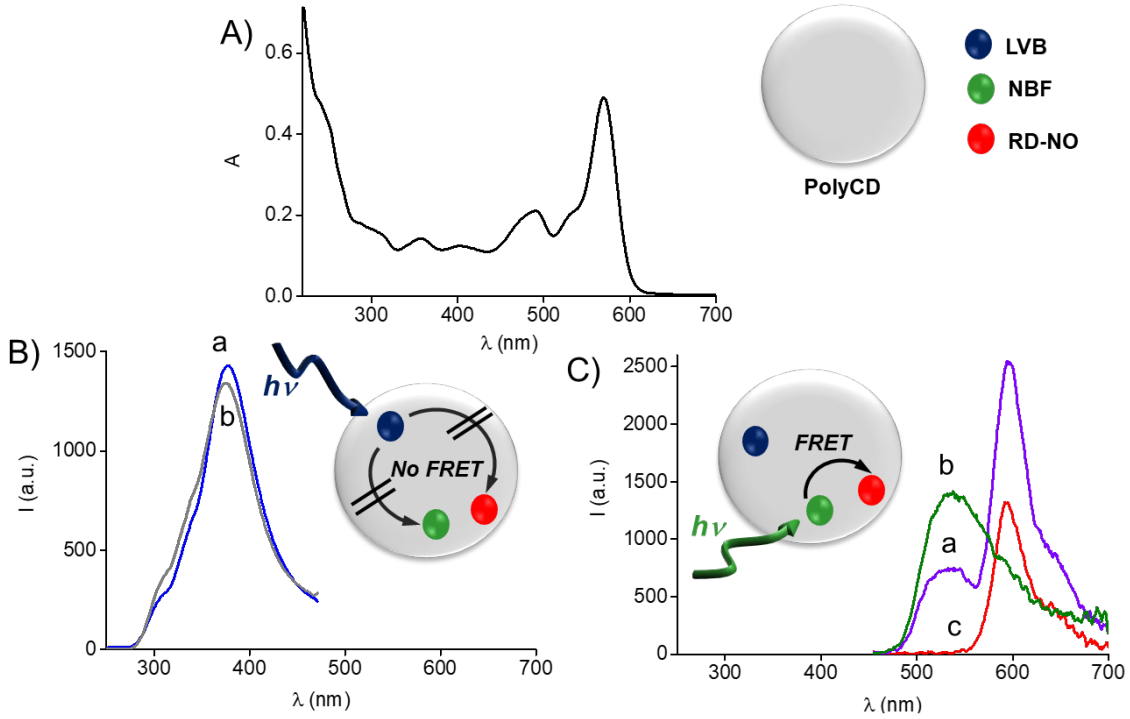

Figure 44: (A) Absorption spectrum of Poly-CD (2 mg/mL) in PBS (pH 7.4) co-loaded with LVB, Rhod-NO, and NBF, equally concentrated (5 µM); **(B)** Fluorescence emission spectra of (a) the sample as in **(A)** and (b) Poly-CD (2 mg/mL) in PBS (pH 7.4) loaded only with LVB at the same concentration (b) recorded at λ_{exc} = 241 nm; **(C)** Fluorescence emission spectra of (a) the sample as in **(A)** and Poly-CD (2 mg/mL) in PBS (pH 7.4) loaded with (b) only NBF and (c) only Rhod-NO (c), recorded at λ_{exc} = 445 nm.

For the sake of control, the same experiment was performed once again in MeOH solution (see Figure 45), to make clear that the FRET phenomenon between NBF and Rhod-NO had occurred thanks to the spatial proximity within the same polymer. Indeed, in organic solution the NBF emission remained almost identical, in the presence or in the absence of the NOPD, confirming that the first one was able to act as an energy donor toward Rhod-NO only when confined in the same polymeric compartment.

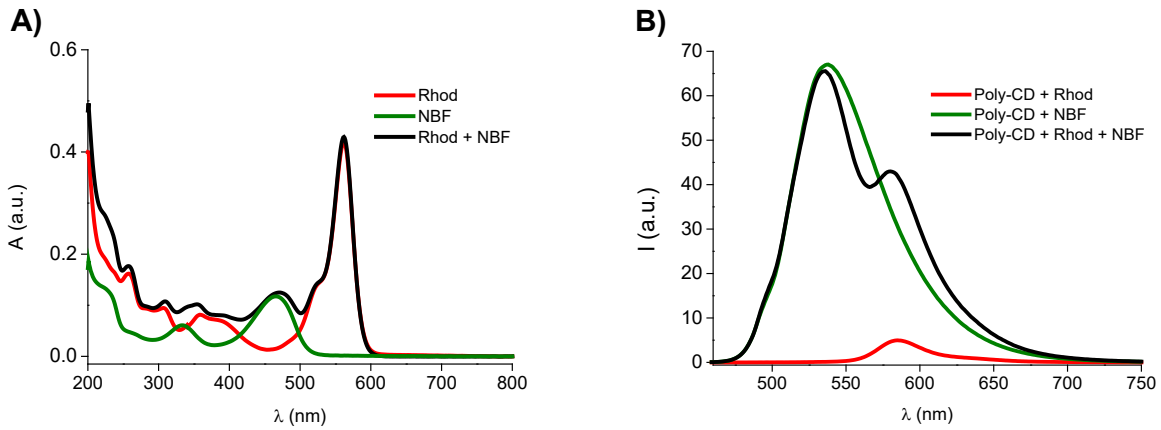

Figure 45: A) Absorption and **B)** emission (λ_{exc}= 445 nm) of equally concentrated NBF, Rhod-NO and both, at the same concentrations, in MeOH; (pathlength= 1 cm).

Note that the FRET experiments reported in Figure 44 C were well reproduced in the presence of a culture medium (5% in serum) for several days, as Figure 46 A reports, confirming the stability of the supramolecular complex even under these experimental conditions (see Figure 46 B). This allowed to assure the complexes stability over time and under the experimental conditions employed for *in vitro* tests.

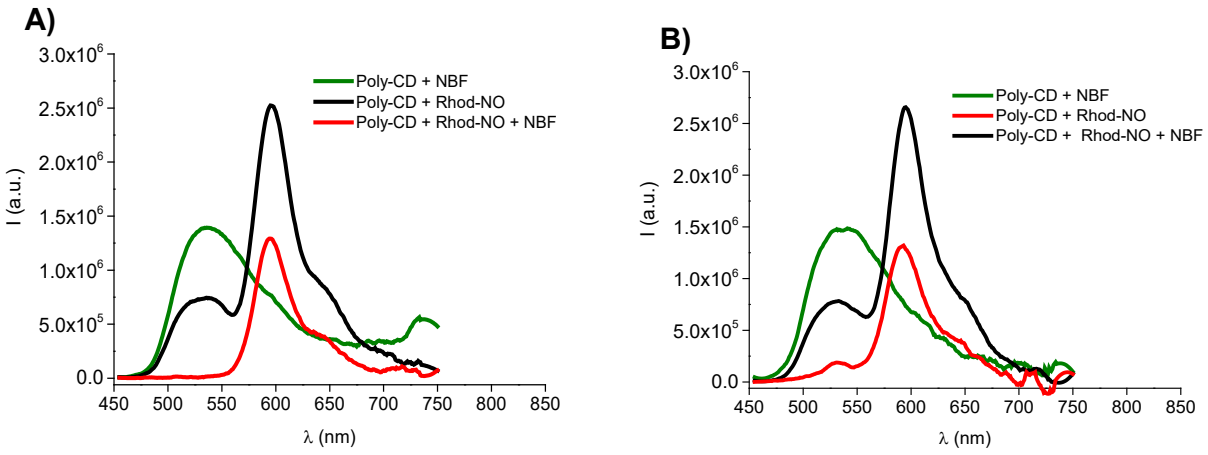

Figure 46: Emission spectra of Poly-CD (2 mg/mL) englobing NBF (6 µM), Rhod-NO (6 µM) and both, at the same concentrations, **A) in culture medium** (with 5% serum) and **B) in PBS** recorded **5 days after the nanoassemblies preparation**; (λ_{exc}= 445 nm).

2.3.8 *In vitro* tests over hepatocarcinoma cells line (Hep-G2)

The chemotherapeutic action of Poly-CD (2 mg/mL) supramolecularly assembling 50 µM LVB and/or 6 µM Rhod-NO was tested upon Hep-G2 cells, both in the darkness and under visible light stimuli. Then, the results were compared with the lethality of free LVB at the same concentration and in the same experimental conditions.

The LVB IC_{50} value upon the Hep-G2 cells was previously calculated, in order to select the most suitable concentration of the chemodrug to be englobed within Poly-CD and to be eventually co-assembled with the NOPD. It had been foreseen to drastically decrease the drug dosage, even below the IC_{50} value, and to consequentially reduce its secondary effects thanks to the synergism with the radical, selectively released from Rhod-NO upon green light irradiation.

The lethality of free LVB over Hep-G2 cells was measured after 4 hours-long incubation with the drug, which did not induce mortality over cells, and the treatment at 24 hours, which led to a limited induced mythocontrial dysfunction. The observed values of IC_{50} are reported in Figure 47.

According to the extrapolation from the dose-response graph by nonlinear regression analysis, the IC_{50} was 132.6 ± 26.8 µM at 24h, and 572.1 ± 235.6 µM at 4h+24h.

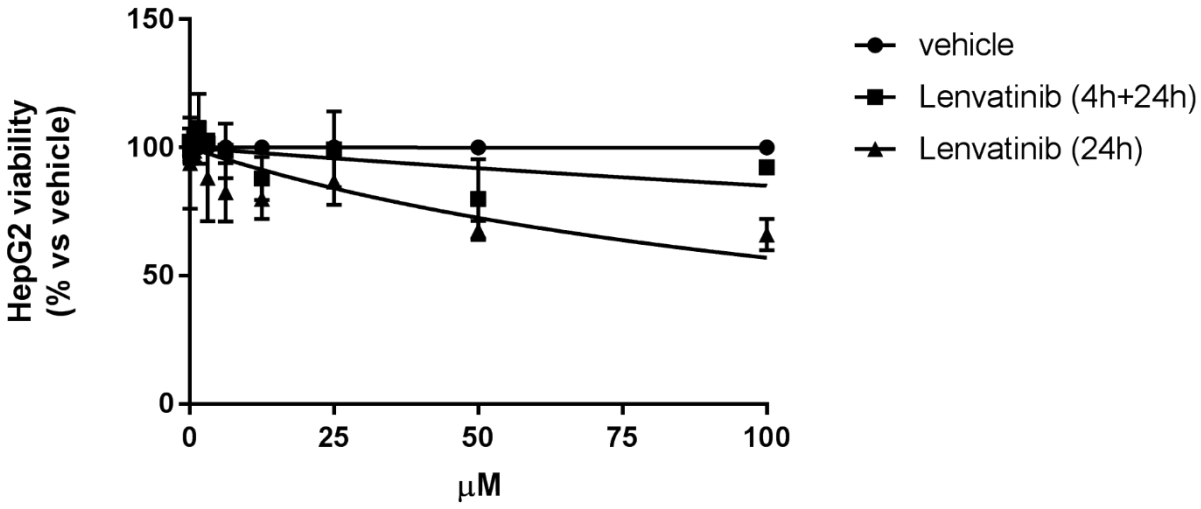

Figure 47: Cells viability of Hep-G2 as a function of the concentration of free LVB.

50 µM LVB was finally selected as suitable concentration of drug to be encapsulated within the polymer and co-assembled with Rhod-NO.

Untreated cells, Hep-G2 treated with free LVB, with empty Poly-CD, with the ternary supramolecular nanoassembly or with the two different binary complexes were irradiated with a Xenon lamp, cutting off UV-light, under λ_{exc}= 500 nm, through a suitable chemical filter. The results were compared with the ones of the Hep-G2 under the very same experimental conditions, but kept in the dark.

The irradiated cells were exposed to light for less than 30 minutes, so that NO could be generated at moderately cytotoxic doses; MTT assay was performed 24 hours after the irradiation.

The synergism between the conventional chemotherapeutic agent and the release of radicals immediately resulted lethal over tumoral cells. As shown in Figure 48, the untreated cells, taken as control, underwent to no mortality both in the darkness and under Vis light irradiation. LVB, in agreement with the much higher IC_{50} calculated values (see Figure 47 for comparison), displayed very low antitumoral properties at 50 µM in any of the experimental conditions. The polymer was very well tolerated by Hep-G2, showing only a slight decrease in cells viability, even upon photoirradiation. When loaded with LVB, Poly-CD led to negligible mortality in the darkness and to a moderated decrease in the viability only at longer irradiation times. On the other hand, when the effects of Rhod-NO within the polymer was considered, higher antitumoral effects were observed, directly proportional to the increasing times of irradiation.

Finally, it was the ternary complex to give the most successful results. In the dark, ca. 70% of the treated cells survived, but under Vis light most of Hep-G2 cells were eliminated. The index of mortality grew together with the increase of the irradiation time, to finally determine the death of ca. 90% Hep-G2 at 30 min. The potentiation indexes of the ternary nanoassembly (considered as the ratio of % viability free LVB / % viability poly-CD/LVB/Rhod-NO) were ca. 3, 5 and 8 at the different times of irradiation (10, 20 and 30 min, respectively).

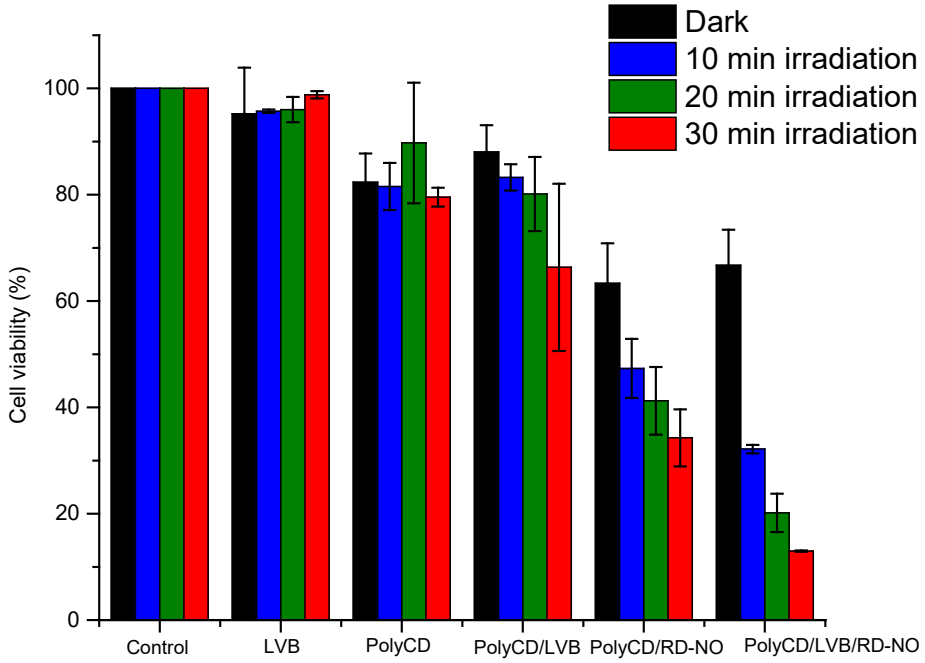

Figure 48: Cell viability in percentual of Hep-G2 cells in the dark and after 10-, 20- and 30-minutes long irradiation with a Xenon lamp and a chemical filter (cutting off under λ_{exc} =500 nm). From left to right: control cells, not treated with the drug and/or or loaded or empty poly-CD; treated cells with 50 µM LVB in its vehicle (DMSO); with Poly-CD (2 mg/mL); with its complexes with 50 µM LVB and/or 6 µM Rhod-NO.

Since it had been demonstrated that the NO release efficiency was not affected by the presence of LVB (see Figure 36 A and Figure 37 for comparison), it resulted obvious that the optimization of the mortality effect induced by the ternary nanoassembly (if compared to the binary ones) was due to the successful synergism between the conventional therapeutic agent and the unconventional one. In agreement with this consideration, it should be once again stressed that also LVB had demonstrated to be perfectly stable under light and after complexation, thus its pharmaceutical activity as a MKI was well maintained.

The internalization of the supramolecular nanoassemblies into Hep-G2 cells was demonstrated by exploiting the emissive properties of Rhod-NO, whose photoexcitation resulted in a diffuse red fluorescence at cytoplasmatic level, unaltered in the presence of LVB, as shown in Figure 49.

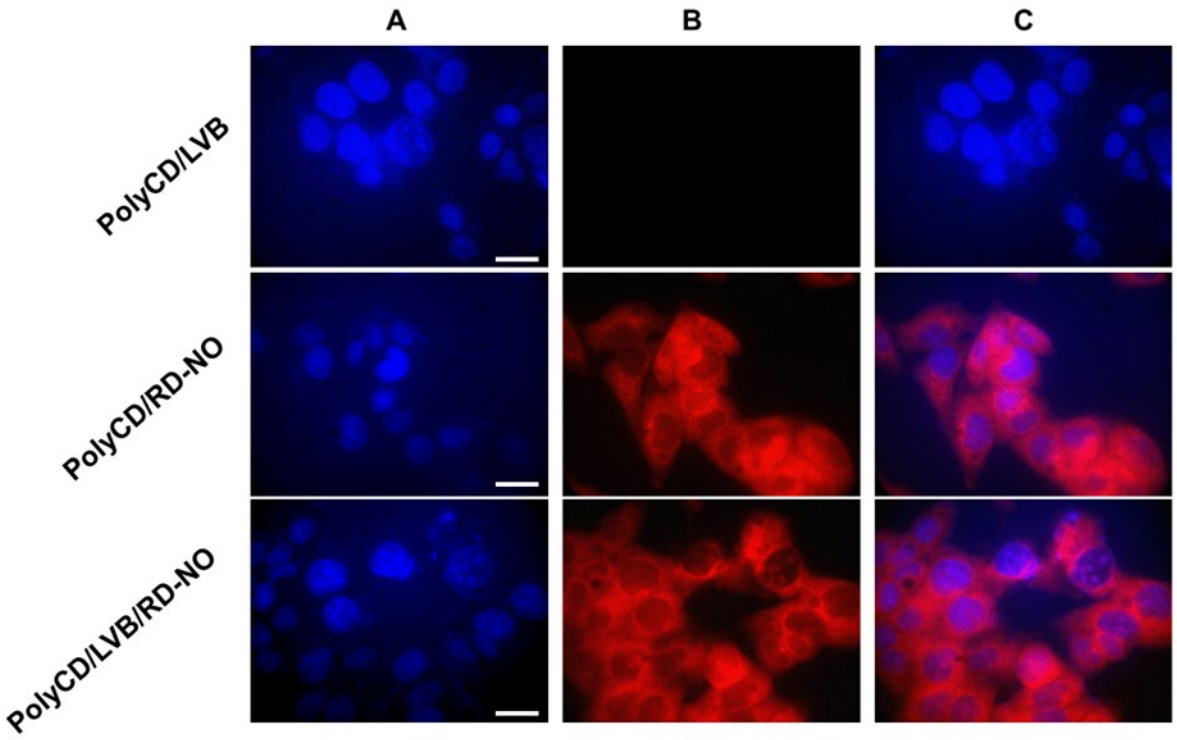

Figure 49: Representative fluorescence microscopy images of Hep-G2 cancer cells incubated for 4 h with 2 mg/mL poly-CD PBS solutions (pH= 7.4), loaded with LVB (25 µM), Rhod-NO (6 µM) or both components, and stained with DAPI. The cells were analyzed with a DAPI.

2.3.9 Conclusions

The above-shown results have demonstrated that the antitumoral activity of LVB can be enhanced by combining it with an NOPD, through the formation of a supramolecular complex based on a biocompatible polymeric host nanocarrier. This latter (i) increased the solubility of LVB by more than one order of magnitude if compared to that observed for the free drug in water, (ii) enhanced the photochemical and photophysical performances of the NOPD and (iii) represents an ideal cargo, since it allowed to simultaneously host the two guests but confined them in different compartments, avoiding any intermolecular communication between them and, thus, preserving their individual properties.

The synergistic action between LVB, which was used at a concentration well below its IC_{50}, and the NO photogenerated at moderated cytotoxic doses through the appropriate light tuning validated the combination of photoregulated NO with MKI as a suitable approach to enhance their anti-cancer action. Compared with the previous work on SRB (see previous section), the present work

represents a step forward in terms of biocompatibility of excitation light (from blue to green) to activate the NO delivery, with a gain of more than 100 nm towards lower energy.

Furthermore, the modular character of the supramolecular assembling of both therapeutic components did not require any additional synthetic efforts, permitting the easy regulation of the relative concentrations of the two guests and facilitating the delivery process in a biological environment. Finally, the use of spontaneous NO releasers in combination with MKI has also been recently proposed as a suitable strategy to exploit the role of NO as a vasodilator able to reduce hypertension [105,106], which is one of the main side effects of this class of chemotherapeutics [77]. In this view, and considering the well-known critical dichotomous biological effects of NO strictly depending on its concentration [98–100,107,108], our findings may also open up interesting avenues in the perspective of *in vivo* applications not only to enhance the anti-cancer activity of MKI but also to reduce one of their major side effects.

2.4 A mixed β-γ-cyclodextrin branched polymer with multiple photo-chemotherapeutic cargo

2.4.1 Introduction

With the aim to advance towards a trimodal approach to cancer treatment, it was developed a novel photo-chemotherapeutic cargo, based on a mixed β- and γ-CDs polymer (βγCD-NOPD) covalently linked to an NOPD and simultaneously hosting LVB and a PS releasing $^1O_2$ under red light.

βγCD-NOPD is a novel, water-soluble and branched polymer, consisting of β- and γ-CDs and covalently integrating a nitroaniline derivative, henceforth NOPD-1 (see Figure 50). LVB (see Figure 7) and zinc phthalocyanine tetrasulphonate (ZnPc) were supramolecularly ensembled within the polymer as representative conventional antitumoral and suitable PS, respectively. The NOPD and ZnPc do not show any overlap in their absorption profiles, thus they could separately be photoactivated with blue and red light, respectively.

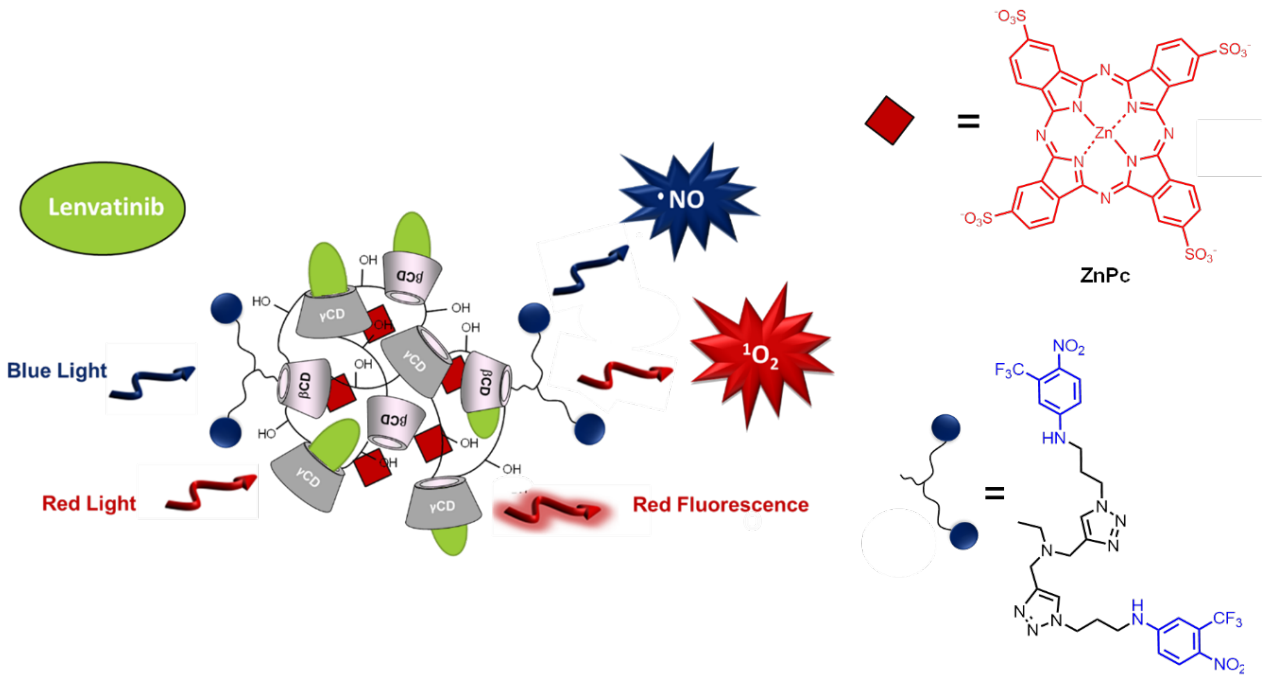

Figure 50: Schematic representation of the mixed branched polymer βγCD-NOPD, functionalized with NOPD-1 and englobing the PS ZnPc and the chemodrug LVB.

2.4.2 Mixed β-γ-cyclodextrin branched polymer

βγCD-NOPD was synthetized by Dr. M. Seggio, in collaboration with Cyclolab Ltd., Budapest, Hungary. βγCD-NOPD (MW *ca.* 70 kDA) contains *ca.* 1.8% (w/w) of NOPD and is highly soluble in aqueous solution.

Figure 51 shows the absorption spectra of the polymer and, for the sake of comparison, of NOPD-1. The first one is dominated by the huge band of the NOPD moiety in the blue region, with a maximum at 393 and extending up to 500 nm. Overall, the spectral profile was unmodified if compared to the free NOPD in water, but in the case of the copolymer, the band resulted to be blue-shifted, of *ca.* 4 nm. This shift may be considered in great agreement with the difference in polarity that NOPD-1 underwent, since, once within the polymeric microenvironment, it was not completely exposed to the aqueous solution, but partially embedded within the more hydrophobic compartments of the polymer.

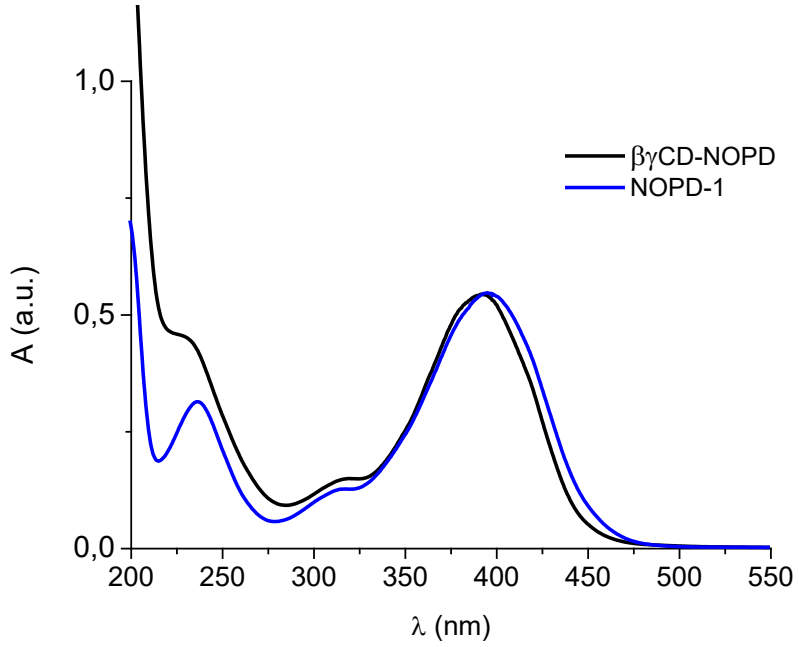

Figure 51: Normalized absorption spectra of βγCD-NOPD and, for the sake of comparison, of the NOPD-1 compound in water.

The irradiation of βγCD-NOPD under blue light resulted in a bleaching of the main absorption band (see Figure 52 A). As reported in Figure 52 B, the photolysis rate was not influenced by the presence or the absence of oxygen. The photobehaviour was in excellent agreement with that one already reported for the single NOPD [95], accounting for the release of NO under photoirradiation and

corroborating the unchanged nature of the primary photochemical process after the NOPD-1 integration in the polymer.

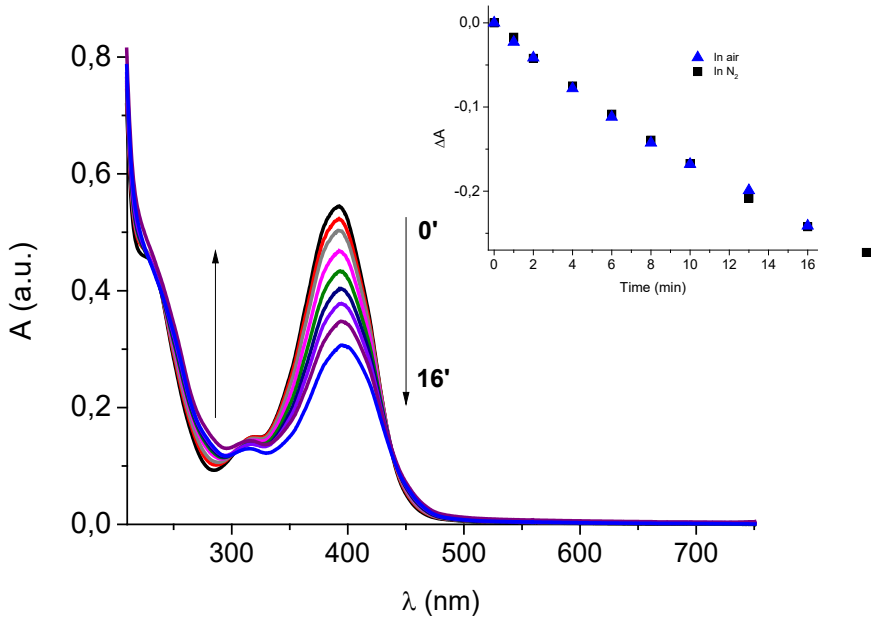

Figure 52: Absorption spectral changes observed upon exposure of an air-equilibrated water solution of βγCD-NOPD (2 mg/mL) at λ_{exc} = 405 nm for time intervals from 0 to 16 minutes. The arrows indicate the course of the spectral profile with the illumination time. The inset shows the absorbance changes with the irradiation time at λ_{exc} = 393 nm, observed in air-equilibrated and N_2-saturated solutions.

The NO release was directly measured through an amperometric detection, as Figure 53 shows. The alternate light/dark cycled demonstrated that the NO generation strictly depended on photoirradiation. Interestingly, it was obtained a NO photorelease value for the polymer equal to Φ_{NO}= 0.007±0.001, which is more than one order of magnitude higher than that one reported for the model NOPD-1 in the same experimental conditions (see Figure 53). This observation is in great accordance with what has been lately reported for NOPDs based on the same chromogenic unit and covalently linked to βCDs-based branched polymers [86], or entrapped in micelles [109,110] or in calixarene hosts [111]. This higher photoreactivity is due to the polymeric CD units, which, indeed, play an active role in providing easily abstractable hydrogens close to the phenoxy-radial intermediate species, formed in the mechanism of NO photorelease (see Figure 9).

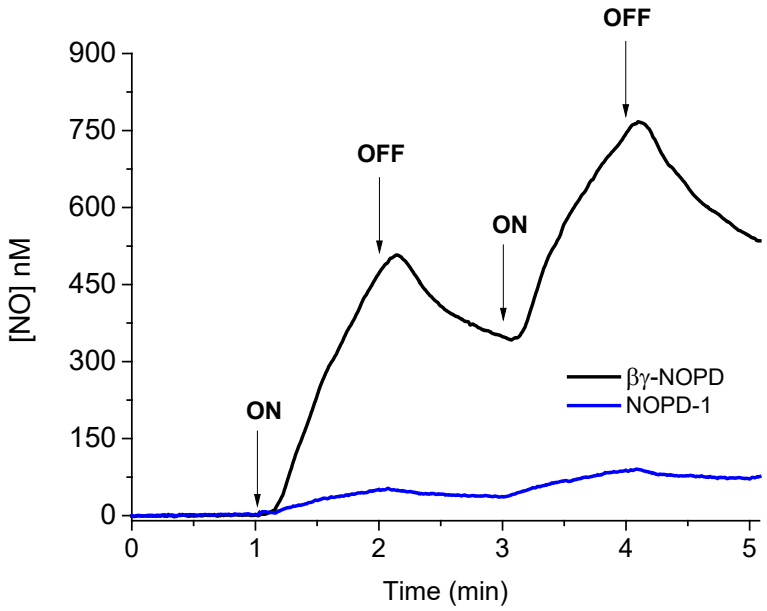

Figure 53: NO release profile observed for an aqueous solution of βγCD-NOPD (2 mg/mL) and of the single NOPD-1 upon alternate cycles of irradiation (λ_{exc}= 405 nm) and dark. T= 25°C.

2.4.3 Solubility of Lenvatinib within the polymer

They were ascertained the hosting abilities of βγCD-NOPD in the encapsulation of the poorly water-soluble LVB.

As previously shown in Figure 31, the solubility of the drug in PBS is *ca.* 4.1 μM (*ca.* 1.7 μg/mL). To evaluate the solubility within the polymer, thin films of LVB at different concentration (from 25 to 160 μM) were let stir with a 2 mg/mL βγCD-NOPD solution in water. As Figure 54 shows, when the most concentrated films were employed (140 and 160 μM), a maximum quantity of 125 μM (*ca.* 52 μg/mL) was solubilized within the polymeric scaffold (see Figure 54 A and B). It corresponds to a *ca.* 30-fold higher concentration than that observed in the absence of βγCD-NOPD, and more than 2-fold higher than that one seen for the same drug in the presence of the same amount of Poly-CD (see Figure 33).

It is worth underlining that the absorption profile of hosted LVB was barely identical to the spectrum in MeOH, which is shown in Figure 54 for the sake of comparison: this indicates the lack of any intra-host aggregation of the chemotherapeutic. Furthermore, all the absorption spectra remained stable for several days, accounting for satisfying stability of the assembly under ambient conditions.

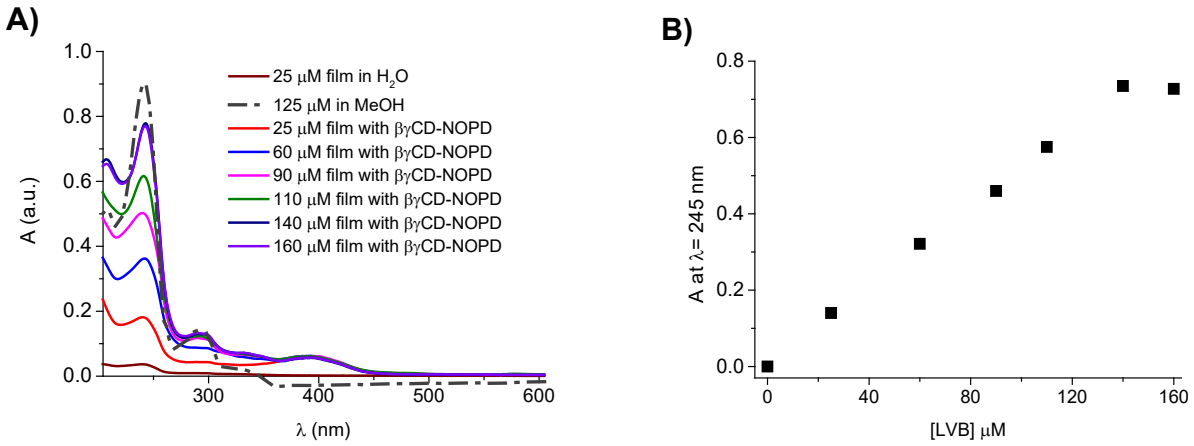

Figure 54: A) Absorption spectra of the PBS solutions of LVB at different concentrations, in the presence or in the absence of βγCD-NOPD (2 mg/mL), (pathlength= 0.1 cm); **B)** Solubility of LVB within βγCD-NOPD (2 mg/mL).

2.4.4 Encapsulation of zinc phthalocyanine tetrasulphonate

βγCD-NOPD turned out to be a perfect scaffold for ZnPc encapsulation too. It is a well-known PS employed for PDT, able to photogenerate cytotoxic $^1O_2$ under highly biocompatible red light irradiation and to emit red fluorescence, essential for imaging [29]. It is very soluble in water, showing absorption bands with maxima at 335 and 635 nm, respectively (see Figure 55). Nonetheless, in aqueous solution they are formed soluble aggregates that obstruct its responsiveness to light, impeding the triplet state to be populated, and, therefore, making unfeasible the $^1O_2$ photogeneration and very low efficient the fluorescence emission [112].

When βγCD-NOPD was added to the ZnPc water solution, self-aggregation was remarkably reduced: the PS was entangled within the polymer as a monomer, in a satisfying amount (> 20%). As Figure 55 shows, the monomerization was ascertained through the decrease of the absorption band at *ca.* 635 nm, belonging to the aggregate form, and the simultaneous formation of a new absorption shoulder, with the maximum at *ca.* 680 nm, already reported in literature to be typical for the monomeric species [113].

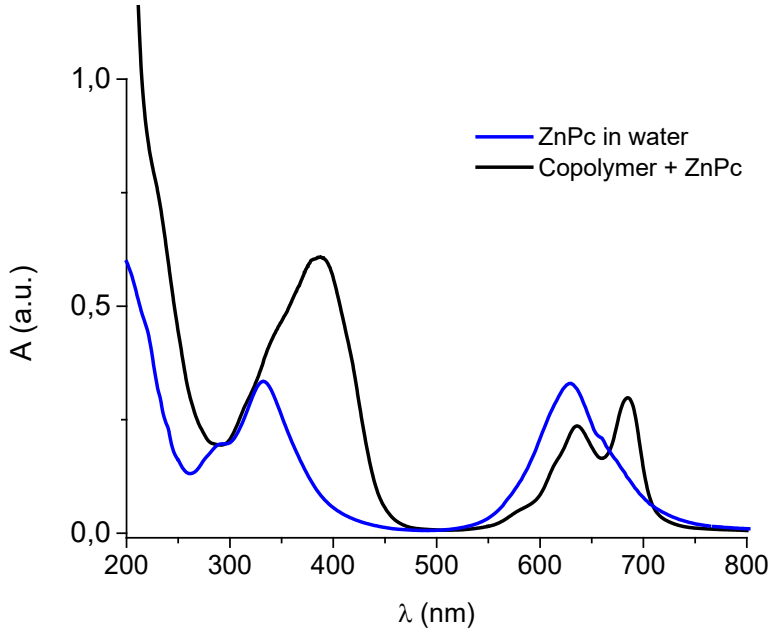

Figure 55: Absorption spectra of ZnPc (10 μM) aqueous solutions, both in the presence or in the absence of 2 mg/mL βγCD-NOPD.

The monomerization in the presence of the polymer resulted in a significant enhancement of the typical red emission of the PS (see Figure 56). When encapsulated, ZnPc showed an emission profile slightly red shifted (of *ca.* 7 nm) if compared to the free form in water. This is attributable to environmental influences on its photo-chemical and photo-physical features: indeed, when the phthalocyanine is solubilized non-aqueous media, its emission results stronger and red-shifted [114]. The inset of the same Figure displays the fluorescence decay, characterized by a very dominant component (> 84%) with a lifetime equal to τ= 3.5 ns.

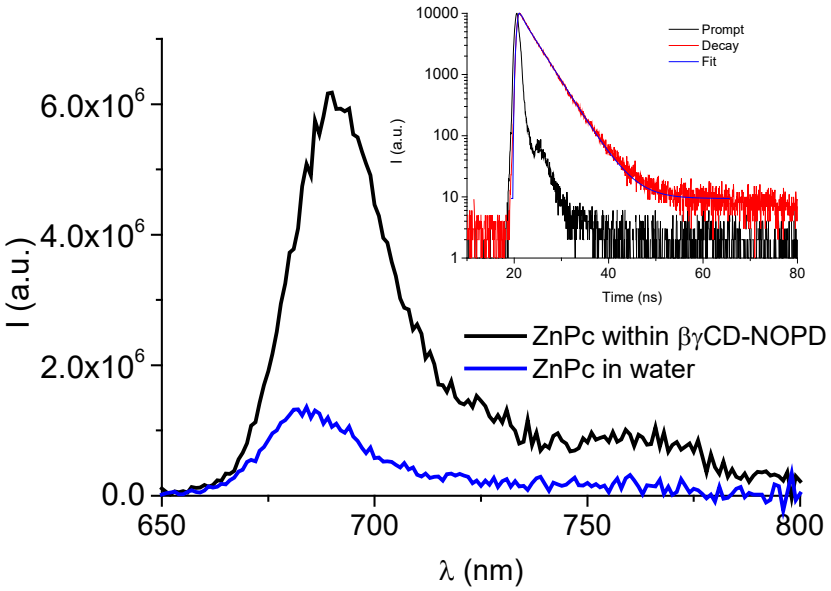

Figure 56: Fluorescence spectra of ZnPc (10 μM) aqueous solution, whether alone or in the presence of βγCD-NOPD (λ_{exc} = 640 nm). The inset shows the fluorescence lifetime and the related fitting of ZnPc in the presence of βγCD-NOPD, recorded at λ_{exc} = 635 nm and λ_{em} = 690 nm.

The entrapment of ZnPc as a monomer can be promoted by the 3D frame of the CD polymer, as a result of the co-operation of the huge local concentration of hosting units and the presence of nanocavities in the cross-linked network for the monomerization [114]. In principle, the benzene sulfonate moieties of the macrocyclic structure of ZnPc display perfect geometrical matching with the β and γCD units, and for this reason are able to easily interact [115,116].

The encapsulation of ZnPc within the branched polymer led to the restore of the fluorescence, but also to the population of the lowest triplet state, the key transient intermediate in the photogeneration of the highly cytotoxic $^1O_2$ through a collisional energy transfer mechanism with the surrounding molecular oxygen [22,24]. Laser flash photolysis with nanosecond time resolution is the best tool to gain insight into spectroscopic and kinetic features of triplet states of porphyrinoid compounds, as these excited intermediates display strong absorptions in the visible region and own lifetimes usually falling in the microsecond time regime [104]. Laser excitation of ZnPc in neat aqueous solution showed a negligible signal, whereas, within the polymeric network it exhibited the characteristic triplet-triplet absorption, with a maximum at 500 nm, and a bleaching of the ground state absorption of the monomer, at 680 nm (see Figure 57).

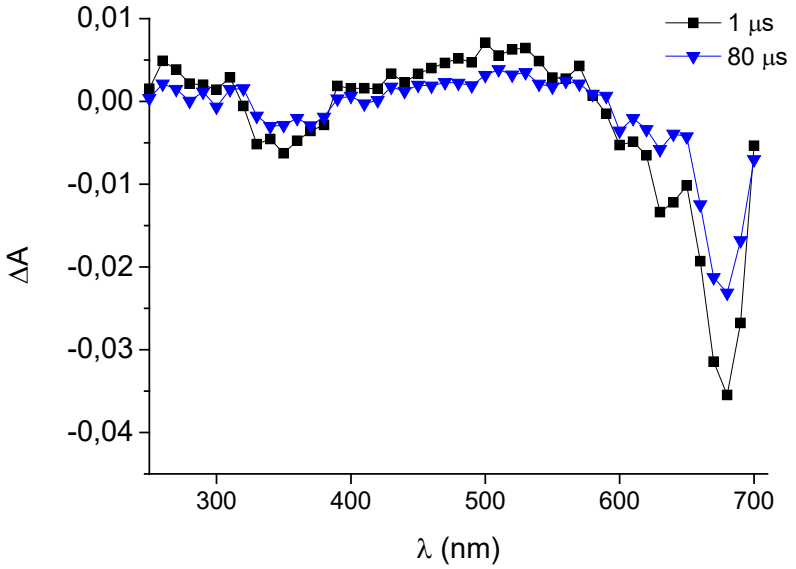

Figure 57: Transient absorption spectra observed 1 μs and 80 μs after 355 nm laser excitation (E_{355} ~ 10 mJ/pulse) of N_2-saturated water solution of βγCD-NOPD (2 mg/mL) loaded ZnPc (10 μM).

The triplet decay was bi-exponential with lifetimes τ_1 ~ 20 μs and τ_2 ~ 300 μs, probably due to the different triplet population confined in different regions of the same host (see Figure 58).

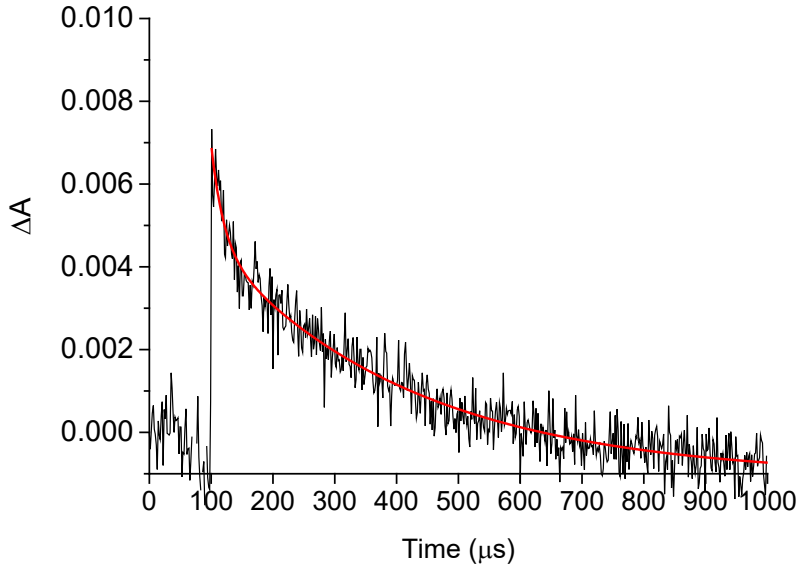

Figure 58: Decay trace and related bi-exponential fitting of the same sample as Figure 57, monitored at 500 nm under N_2-saturated conditions.

2.4.5 Ternary assembly of the polymer with Lenvatinib and zinc phthalocyanine

Both LVB and ZnPc were co-encapsulated within β,γCD-NOPD in a two-steps method: a ZnPc aqueous stock solution was initially stirred for at least 24 hours in the presence of the polymer; then, the chemotherapeutic was added too by exploiting a thin film (see Material and Methods section).

The effective formation of the ternary construct was monitored by comparing the absorption spectra of the β,γ-CD-NOPD alone and its nanoassemblies with LVB and/or ZnPc, whether singularly or simultaneously encapsulated. As Figure 59 shows, the novel nanoassembly absorption profile was characterized by the typical shoulder belonging to the copolymer, at *ca.* 390 nm, accompanied by the characteristic absorption of LVB in the UV region (at *ca.* 240 nm) and the one of the partially monomerized ZnPc at 680 nm.

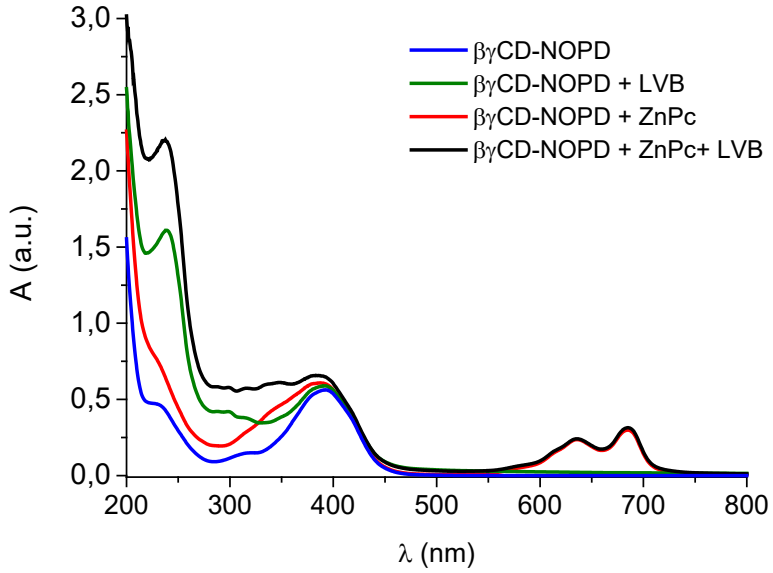

Figure 59: Absorption spectra of ZnPc (10 μM) aqueous solution and/or LVB (25 μM), in the presence of 2 mg/mL βγCD-NOPD, whether alone or simultaneously co-loaded within the copolymer, at the same concentrations; (pathlength= 1 cm).

It is essential to underline that the absorption maxima position, the absorbance values and the spectral profiles of all the involved chromogenic components were basically unchanged if compared to the absorption spectra of the two guests individually hosted in the same polymer. This observation granted the lack in any displacement or aggregation phenomena of the individual

chromogenic centres when co-encapsulated, probably explainable with different affinity of the hosts for the numerous binding sites of the polymer.

The fluorescent properties of ZnPc and LVB co-entangled within the host were barely identical to those found when they were singularly encapsulated. As Figure 60 shows, the same emission profile was noted for ZnPc alone and with LVB (see Figure 56 for comparison).

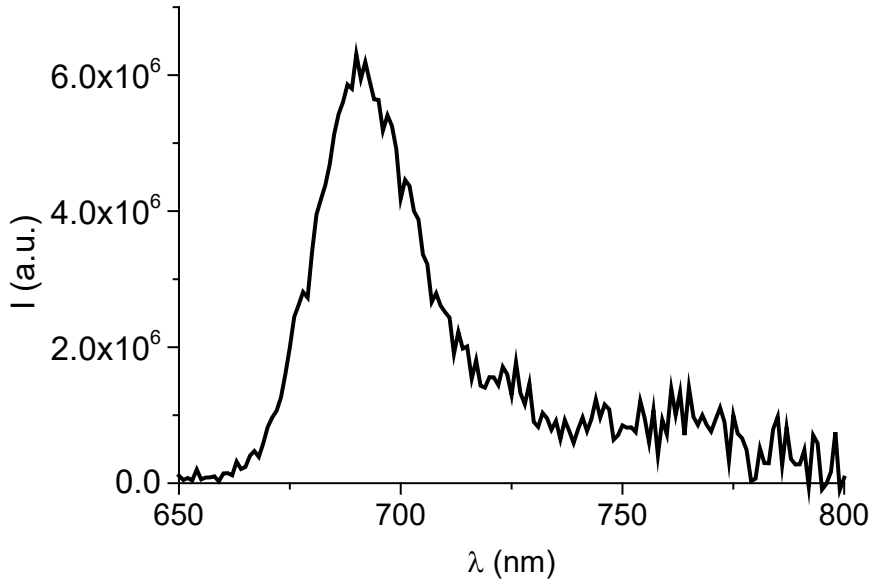

Figure 60: Fluorescence spectra of ZnPc (10 μM) aqueous solution, in the presence of βγCD-NOPD (2 mg/mL) and LVB (25 μM) (λ_{exc} = 640 nm).

DLS data indicated an average hydrodynamic diameter of *ca.* 15 nm for the ternary nanoassembly (see Figure 61). The relative inset shows a real picture of the ternary nanoassembly aqueous solution.

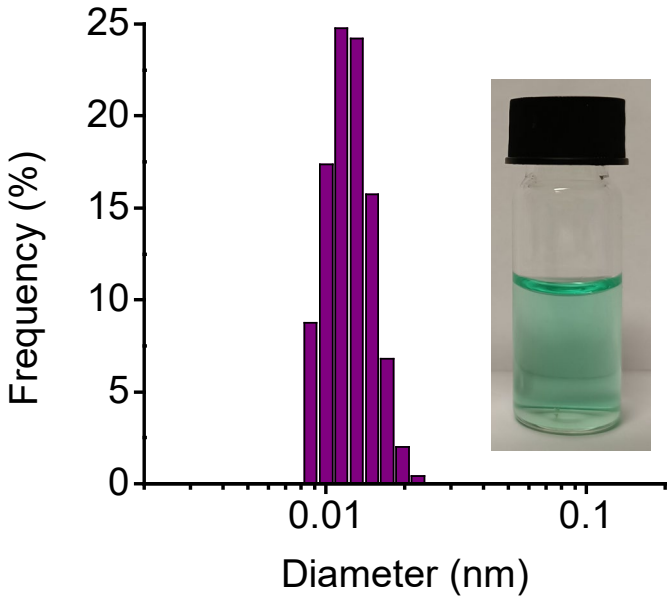

Figure 61: Hydrodynamic diameter and the actual picture of the ternary supramolecular assembly.

The capabilities of the ternary nanocargo to photogenerate NO and $^1O_2$ under light irradiation were investigated to evaluate its photodynamic properties.

Blue light irradiation resulted in the bleaching of the NOPD moiety absorption band at *ca.* 390 nm, with a photobehaviour and a photodecomposition rate very similar to those observed for the unloaded polymer (see Figure 52 for comparison). This indicates an efficient NO release and suggests the lack in any quenching effect and/or unexpected photochemical reaction, competitive with the NO release, and potentially due to the encapsulation of LVB and ZnPc. Furthermore, no spectral changes could be observed related to the absorption shoulders of LVB and ZnPc, in the UV and red spectral region, respectively, indicating the preservation of their structural integrity upon light exposure.

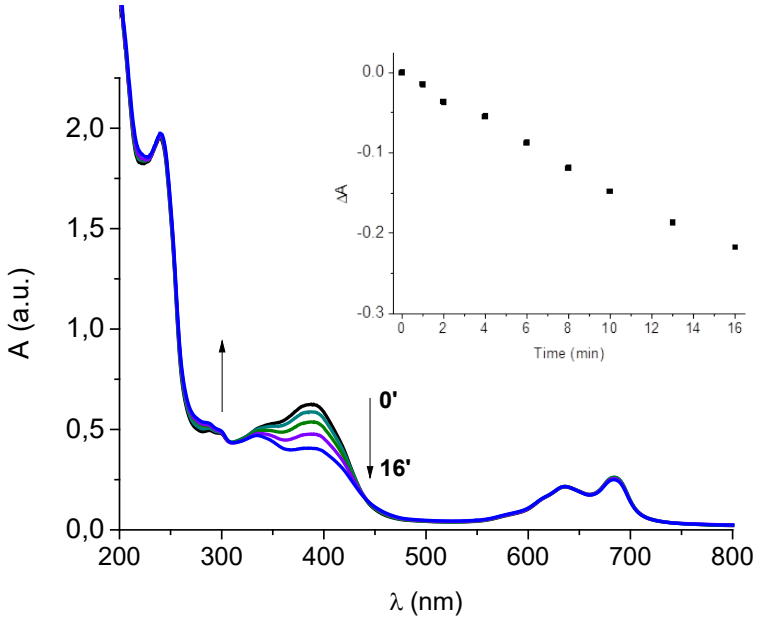

Figure 62: Absorption spectral changes observed upon exposure of an air-equilibrated water solution of βγCD-NOPD (2 mg/mL), loaded with LVB (25 µM) and ZnPc (10 µM), at λ_{exc} = 405 nm for time intervals from 0 to 16 min. The arrows indicate the course of the spectral profile with the illumination time. The inset shows the absorbance changes with the irradiation time at λ = 393 nm.

The direct amperometric detection unambiguously confirmed the NO photorelease (see Figure 63). Just like the recorded absorption spectral changes did, this analysis demonstrated the same efficiency that the empty polymeric host had shown (see Figure 53 for comparison).

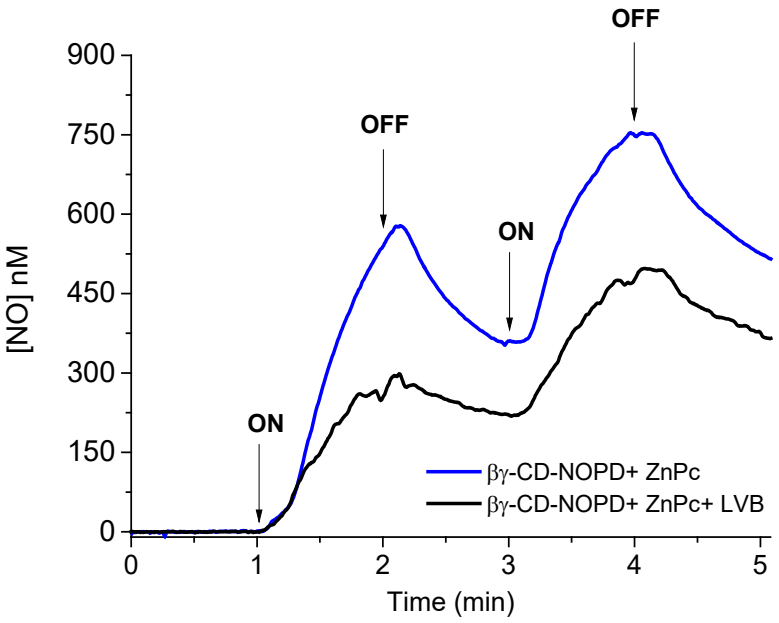

Figure 63: NO release profile observed for an aqueous solution of βγCD-NOPD (2 mg mL^{-1}) and of the model compound NOPD-1 upon alternate cycles of irradiation (λ_{exc} = 405 nm) and dark.

In Figure 64 are shown the transient absorption spectra observed at two different delay times after the initial laser pulse. After 1 μs, it was visible a band with a maximum at 500 nm and a bleaching at 680 nm, typical of the lowest triplet state of ZnPc in its monomeric form. The triplet absorbance was comparable to that one shown in Figure 57, relative to the same nanoassembly in the absence of LVB. If it is considered that the two aqueous solutions were optically matched at the excitation wavelength and that huge differences in the molar extinction coefficients of the triplet states are fairly improbable, being substantially identical in the bands profiles, the triplet absorbance is directly related to the efficiency of the triplet population which, for all these reasons, was not affected by the co-encapsulation of LVB.

Moreover, the antitumoral did not influence the dynamic of the ZnPc triplet. The spectrum recorded at 80 μs showed that no additional transient species, concurrently to its decay, were formed with the time evolution of the triplet state.

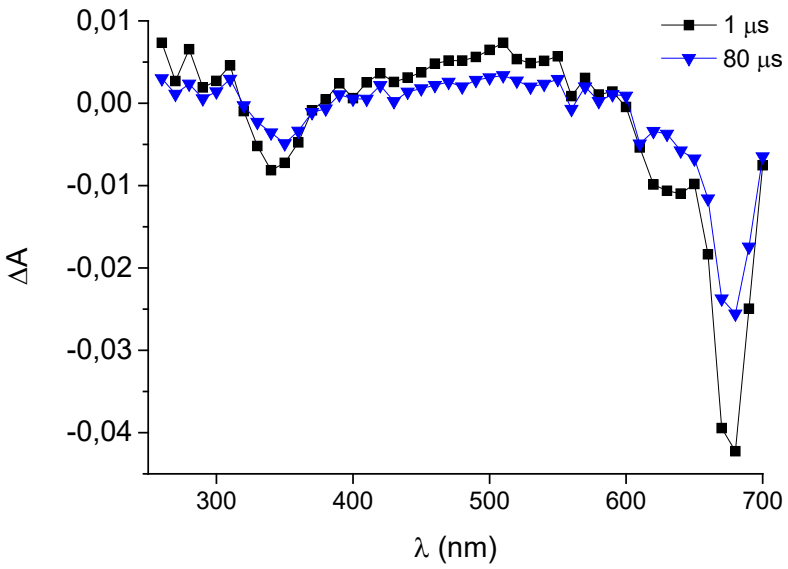

Figure 64: Transient absorption spectra observed 1 μs and 80 μs after 355 nm laser excitation (E_{355} ~ 10 mJ/pulse) of N_2-saturated water solution of βγCD-NOPD (2 mg/mL) loaded with LVB (25 μM) and with ZnPc (10 μM).

As it was already observed in the absence of LVB (see Figure 58), ZnPc in the ternary assembly showed a bi-exponential triplet decay, with lifetimes τ_1 ~ 18 μs and τ_2 ~ 200 μs (see Figure 65).

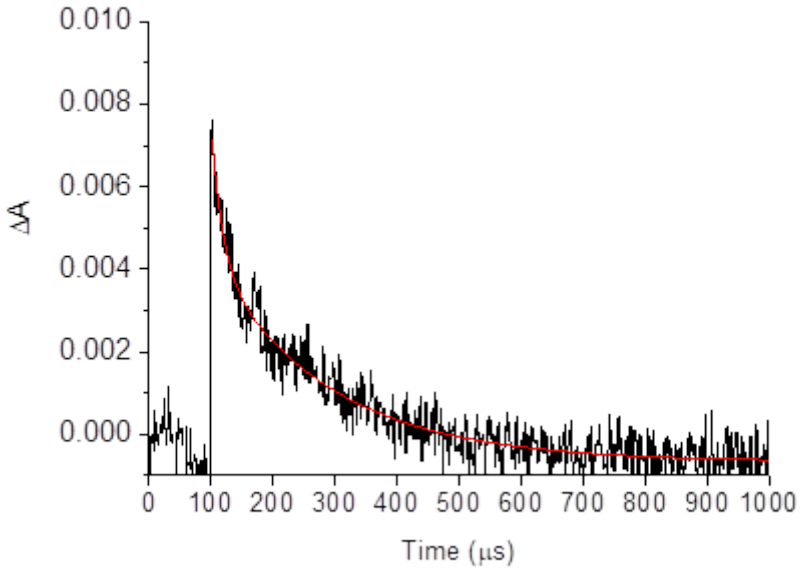

Figure 65: Decay trace and related bi-exponential fitting of the same sample as in Figure 64, monitored at 500 nm under N_2-saturated conditions.

The significant shortening of the triplet decay in air-equilibrated system, in Figure 66, accounted for the effective quenching of the triplet state by oxygen: it was mono-exponential, with a lifetime $\tau \sim$ 10 μs. This demonstrated that, even if entangled within the polymeric network, the ZnPc triplet still remained available and accessible for the collisional energy transfer with the surrounding oxygen and the consequent photoproduction in $^1O_2$.

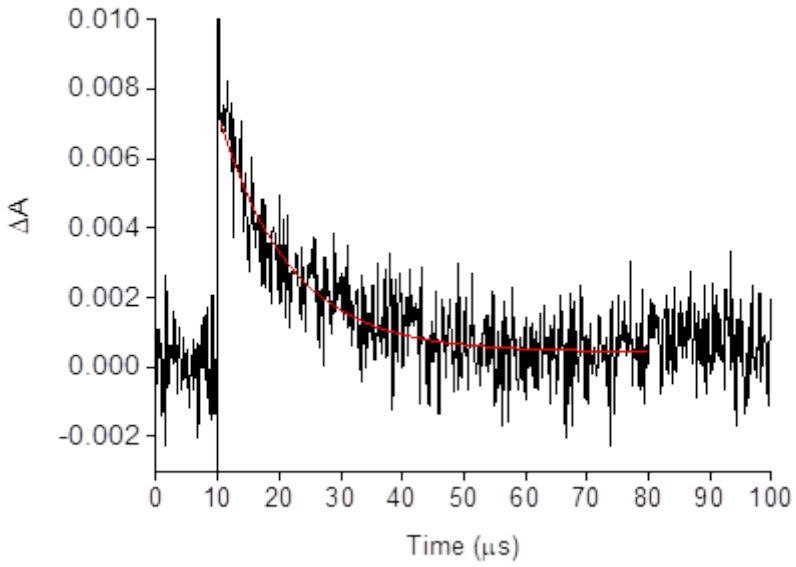

Figure 66: Decay trace and related mono-exponential fitting of the same sample as in Figure 64, monitored at 500 nm under air-equilibrated conditions.

The photogeneration of $^1O_2$ by the ternary nanoassembly was directly visualized through the detection of its typical near-IR spectral region phosphorescence, with a maximum at *ca.* λ_{em}= 1270 nm (see Figure 67). A value equal to $\Phi_\Delta = 0.25 \pm 0.05$ was calculated for the $^1O_2$ quantum yield, using methylene blue as a standard (see Material and Method section). It is essential to underline that red light excitation under aerobic conditions did not induce any substantial change in the entire absorption profile, ruling out any undesired bimolecular reaction of the ZnPc triplet state with the NOPD unit of the polymer and/or with the encapsulated LVB. Moreover, any potential oxidation of all the involved chromogenic component by the photogenerated $^1O_2$ should be excluded.

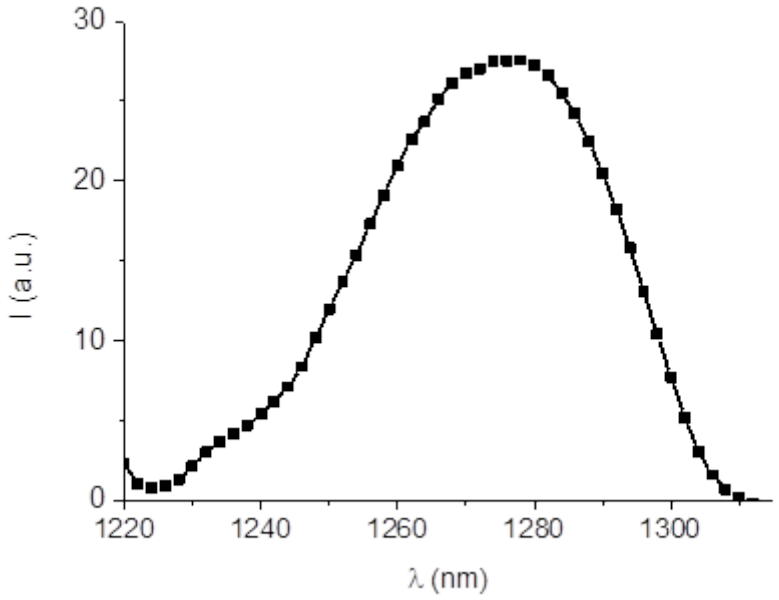

Figure 67: $^1O_2$ luminescence detected upon 671 nm light excitation of an air-equilibrated D_2O solution of βγCD-NOPD (2 mg/mL) loaded with LVB (25 µM) and of ZnPc (10 µM).

2.4.6 Conclusions

It was synthesized a branched polymeric material covalently integrating β and γCD units, functionalized with an NOPD moiety within its macromolecular network. The photoresponsive βγCD-NOPD polymer is highly soluble in water medium, presents compartments with different sizes

and hydrophobicity and has demonstrated to be a versatile polymeric host for the straightforward modular integration of multiple functional components. In fact, the simultaneous co-encapsulation of a hydrophobic chemodrug and a hydrophilic PS, allowed to achieve a system with a multiple photo-chemotherapeutic cargo into a single supramolecular construct with functions that would be otherwise impossible to replicate with the separate components.

In particular, the polymeric host: i) amplified the photoreleasing efficiency of the cytotoxic NO due to its active role as a reactant in the NO photorelease process; ii) increased the solubility of LVB more than 30-fold if compared with the free drug and more than two-fold if compared with a similar polymer containing only βCD units; iii) disrupted the aggregation of the non-photoresponsive ZnPc, making it photochemically active and able to produce the cytotoxic $^1O_2$ and emit red fluorescence.

A remarkable point of this nanoconstruct is the absence of mutual interactions between the NOPD unit, the PS and the chemodrug both in the ground and excited state, despite all components are confined in the same host. This result is not trivial and allowed the preservation of nature and efficiency of the individual photochemical properties of the phototherapeutic components while preserving the structural integrity of the chemodrug. In view of these results, we believe this polymeric multicargo nanoplatform, the first to our knowledge with the described peculiarities, may represent an intriguing system with potential trimodal photo-chemotherapeutic action to be tested in biological systems.

2.5 Near-Infrared Plasmonic Gold Nanostructures by Pomegranate Extract and Their Supramolecular Assembling with Chemo- and Photo-Therapeutics

2.5.1 Introduction

They were synthetized Au nanostructures, displaying a LSPR in the NIR spectral range, through a single, green step employing *Punica granatum* (pomegranate) seeds extract (PSE) as a reductant, in the presence of Poly-CD (see Figure 27). The β-CD polymer granted stability and water-solubility to the capped Au-nanoobjects (Au@Poly-CD) and allowed their co-assembling with SRB (Figure 6) and Rhod-NO (Figure 28). They were obtained novel supramolecular hybrid nanoconstructs for chemo- and photo-therapeutic applications (see Figure 68).

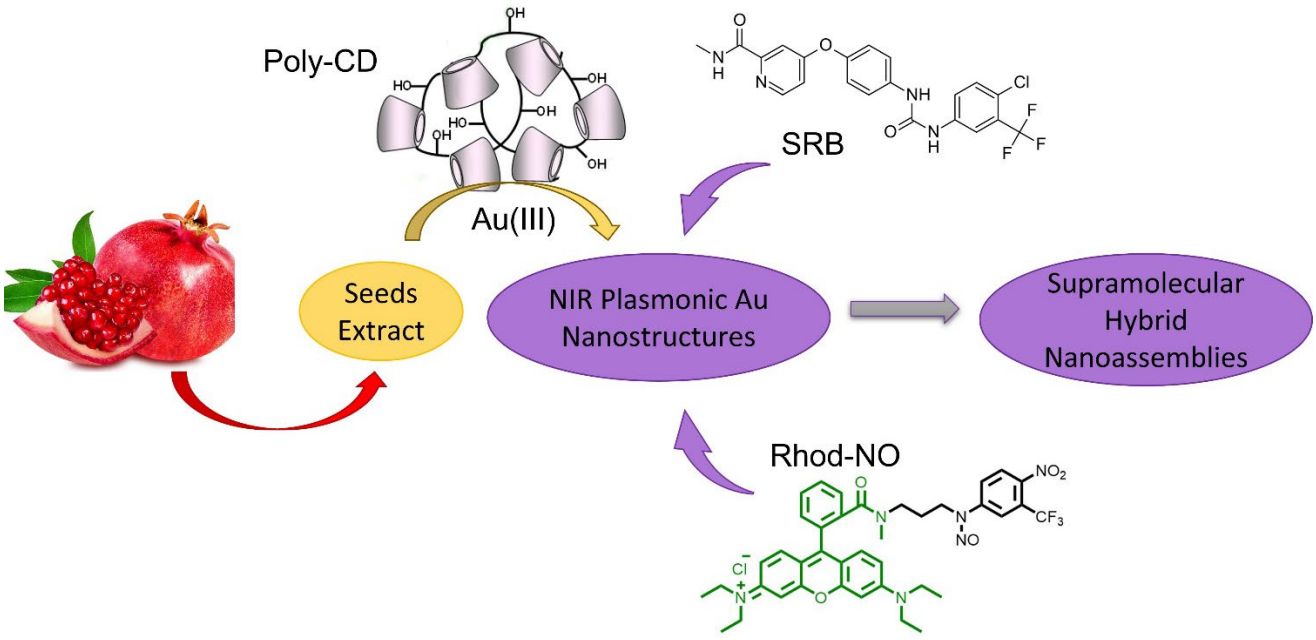

Figure 68: Schematic representation of NIR plasmonic Au nanostructure synthesis and their supramolecular assembling with SRB and Rhod-NO, allowed by Poly-CD.

As already discussed in the Introduction, PTT is one of the most intriguing unconventional approaches to cancer treatment, particularly appealing for its low cost, good specificity, and slight secondary effects to normal tissues [14].

The latest advances in the field of nanoscience made noble metal nanostructures highly appealing allies in PTT application for cancer treatment. Au, for example, thanks to the phenomenon of surface plasmon resonance allows its selective irradiation in the so-called “therapeutic window” (from 650 to 1350 nm), resulting in production of heat with great efficiency and excellent photostability [19, 20].

2.5.2 Synthesis of the Au nanoparticles

The absorption spectral changes of a solution of PSE in the presence of Poly-CD and $HAuCl_4$ were monitored as a function of time (see Figure 69). It was noted the formation of two LSPR absorption bands in the Vis and NIR spectral regions, at ca. 530 nm and ca. 850 nm, respectively, which are typically observed for Au nanostructures. The formation process was completed within *ca.* 6 hours. No isosbestic points were noted, according to the complexity of the process that leads to the formation of Au(0) [121].

As the inset in Figure 69 shows, Au@PolyCD formation was visible even at naked eye, considering that the initial transparent solution assumed a typical purple color over time.

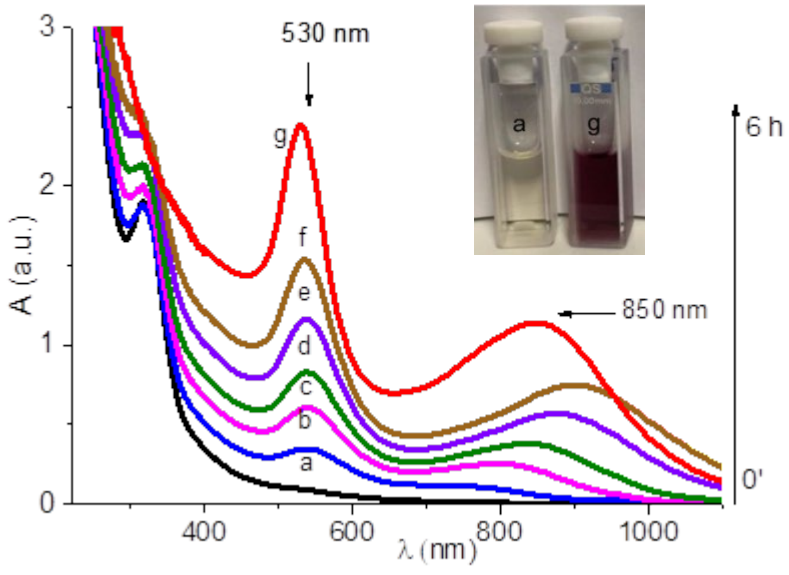

Figure 69: Absorption spectral changes from 0 min (a) to 6 h (g), observed for an aqueous solution of Poly-CD (2 mg/mL) capping PSE (4.5 mg/mL) in the presence of $HAuCl_4$ (0.4 mM). The inset shows the picture of the sample a and g, respectively; T = 25 °C.

The final solution was centrifugated and the supernatant was removed in order to purify the nanoobjects and eliminate any excess of non-reacted $HAuCl_4$ and non-capping β-CDs. The precipitate showed good dispersibility in water and its absorption profile maintained the two LSPR bands in the Vis and NIR spectral regions, at ca. 530 nm and 810 nm, respectively (see Figure 70).

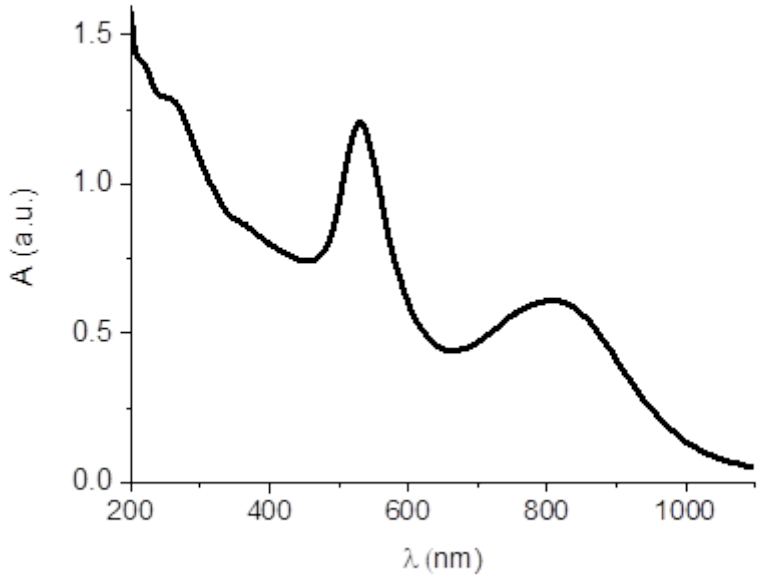

Figure 70: Absorption spectrum of an aqueous dispersion of Au@Poly-CD.

When the Au nanostructures were synthetized with higher concentrations of PSE, in the presence of equally concentrated $HAuCl_4$, only the LSPR in the Vis region were maintained, while the band in the UV spectral range was lost (see Figure 71). This implies that the nanoobjects shape is strongly dependent on the ratio between the two components. In a previous work from our research group, an equivalent trend had been commented for the same polymer in the presence of different ratio of the Au precursor and the reductant, which, in that case, was NO [122]. This aspect needs to be deeper investigated.

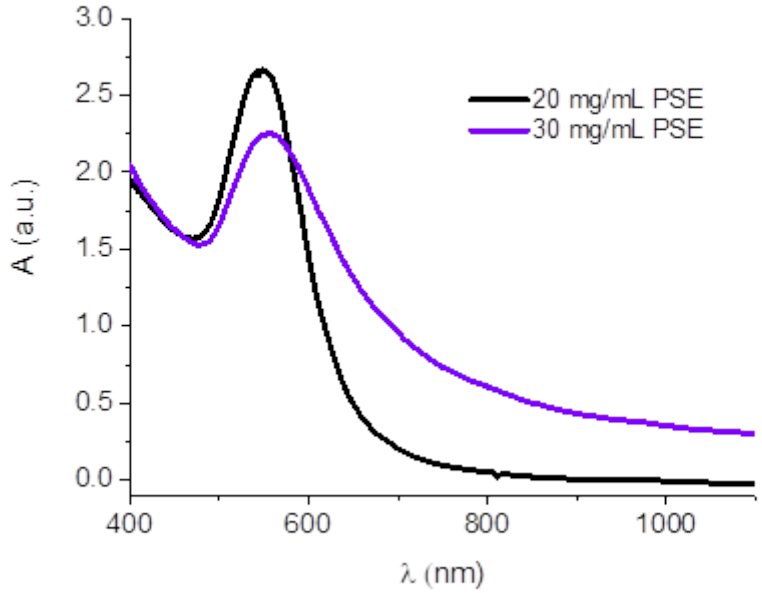

Figure 71: Absorption spectra of Au nanostructures formed with 20 or 30 mg/mL PSE in the presence of 0.4 mM $HAuCl_4$ in a Poly-CD (2 mg/mL) aqueous solution.

The same formation protocol was also repeated in the absence of the polymeric scaffold and the absorption spectral evolution was monitored at different times, as Figure 72 shows. In this case, the band in the Vis range was formed in similar time intervals, but the NIR region one, extending beyond 1000 nm, was weaker, non-defined and with much higher scattered light, which accounts for the generation of poorly water-soluble aggregates. These evidences support the hypothesis that the polymeric network plays a central role in the determination of the shape, solubility and stability over time of the Au NPs. It may also be added that a redox process between PSE and Au (III), probably occurring within the polymeric scaffold, might support the generation of the observed plasmonic Au nanostructures under our experimental conditions, thanks to the complexation ability of the β-CDs branched polymer towards Au metal ions. Indeed, similarly to other observed cases of Au (III) within other branched β-CDs polymeric scaffolds, a significant red-shift (*ca.* 20 nm) was observable for $HAuCl_4$ absorption band in the presence of Poly-CD (λ_{max} *ca.* 310 nm), if compared to the one in CDs absence (λ_{max} *ca.* 290 nm) [29, 30].

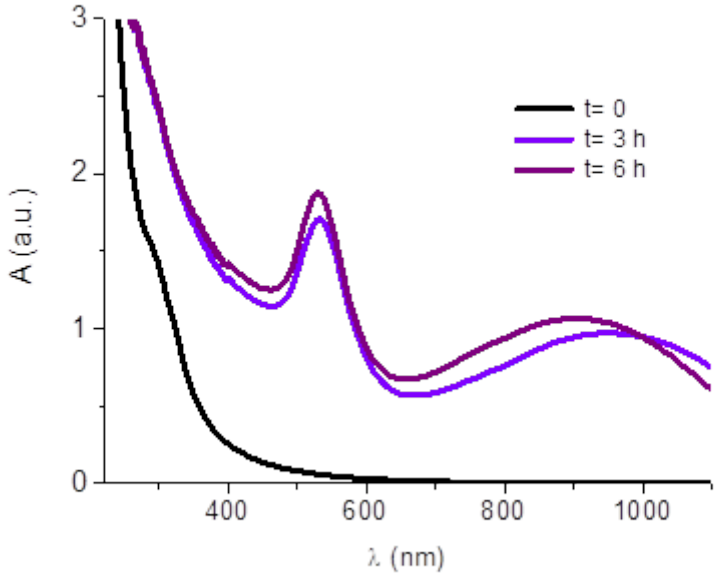

Figure 72: Absorption spectral changes from 0 min to 6 h, observed for an aqueous solution of PSE (4.5 mg/mL) and $HAuCl_4$ (0.4 mM), in the absence of Poly-CD.

2.5.3 Dynamic Light Scattering and Transmission Electron Microscopy analyses

DLS measurements were performed on the aqueous dispersion of Au@Poly-CD, confirming the presence of Au nanostructures with a hydrodynamic diameter of ca. 55 nm (see Figure 73 A).

Transmission Electron Microscopy (TEM) was also exploited to directly visualize the Au nanostructures, which were revealed to be divided into two species: almost-spherical nanoparticles NPs, with an average diameter of 19 nm, and non-spherical nanostructures, such as triangles and pentagons, with a dimension between 36 and 45 nm (see Figure 73). According to literature, the spherical NPs give rise to the LSPR localized in the Vis region, while the non-spherical ones cause the LSPR localized in the NIR region [32, 33]. Both of them remained stable and well dispersible in water for weeks, most likely thanks to the fine capping ability of the β-CDs polymeric units towards Au nanostructures [30, 31, 34].

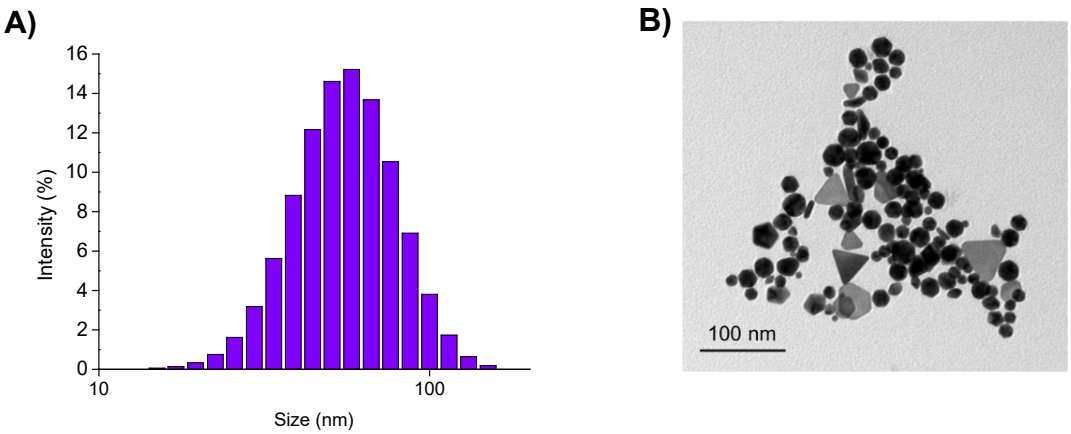

Figure 73: A) Size distribution of Au@Poly-CD measured by DLS; **B)** Representative TEM image of Au@PolyCD. The inset shows the size distribution of the almost-spherical NPs.

2.5.4 Photothermal properties

The photothermal properties of the Au@Poly-CD were evaluated through their irradiation with a λ_{exc} = 808 nm CW laser. The variations of temperature upon photoexcitation were monitored through an infrared (IR) camera. As Figure 74 shows, the temperature rapidly increased as soon as the light laser was turned on, reaching a plateau value of ca. 42 °C (ΔT = ca. 18 °C) in few minutes; then, it immediately decreased as photoexcitation was stopped. For the sake of control, a pure water sample was irradiated in the same experimental conditions and it led to no significant changes under light. They were taken during the irradiation thermographic images trough the IR camera, that allowed to visualize even at naked eye the considerable increase in temperature (see Figure 74).

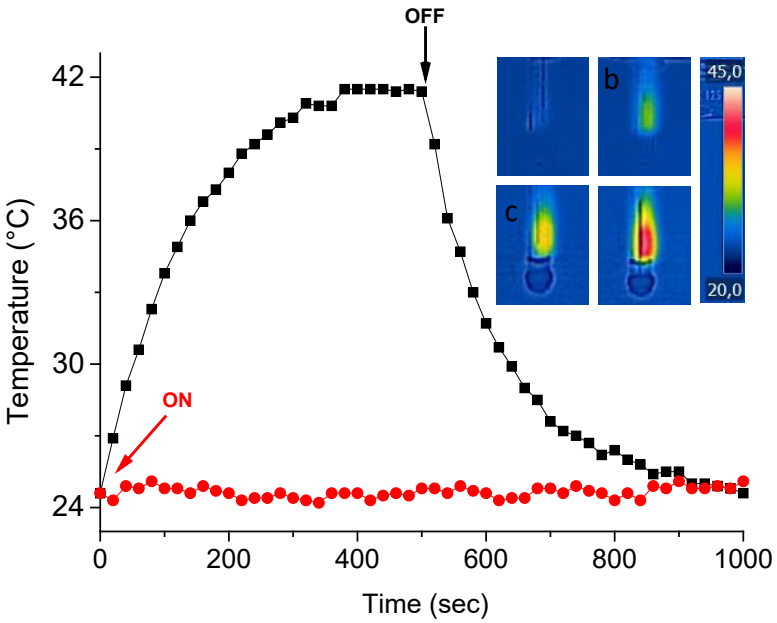

Figure 74: Temperature changes observed upon 808 nm CW laser irradiation (6 W cm^{-2}) of 100 µL Au@PolyCD sample (in black scatters) reported in Figure 74 and, for the sake of comparison, of pure water (in red). The inset shows representative thermographic images of the Au@Poly-CD sample, recorded after 0, 60, 140, and 400 s of irradiation and displaying a) 24.5 °C; b) 30.6 °C; c) 41.5 °C; d) 35.8 °C.

2.5.5 Encapsulation of Sorafenib

Once the photothermal features of Au@Poly-CD had been tested, the hosting properties of Poly-CD were exploited to encapsulate SRB and Rhod-NO. The final goal was to obtain multimodal therapeutic systems that may synergize PTT with additional antitumoral agents.

An aqueous solution of Poly-CD was stirred together with a SRB film (obtained by evaporating the solvent from a stock solution in MeOH) and the incorporation of the drug was ascertained through the absorption spectra (see Figure 75). Indeed, an increase of the absorption band at *ca.* 268 nm, typical of SRB, was detectable when the drug was englobed. This evidence suggested that Poly-CD, while already capping Au NPs, was able to complex the chemodrug too, leading to the formation of a new host-guest system, henceforth Au@Poly-CD@SRB. By employing the molar extinction coefficient of SRB within Poly-CD previously reported, a concentration of *ca.* 1.5 µg/mL drug could be estimated within the Au@Poly-CD@SRB.

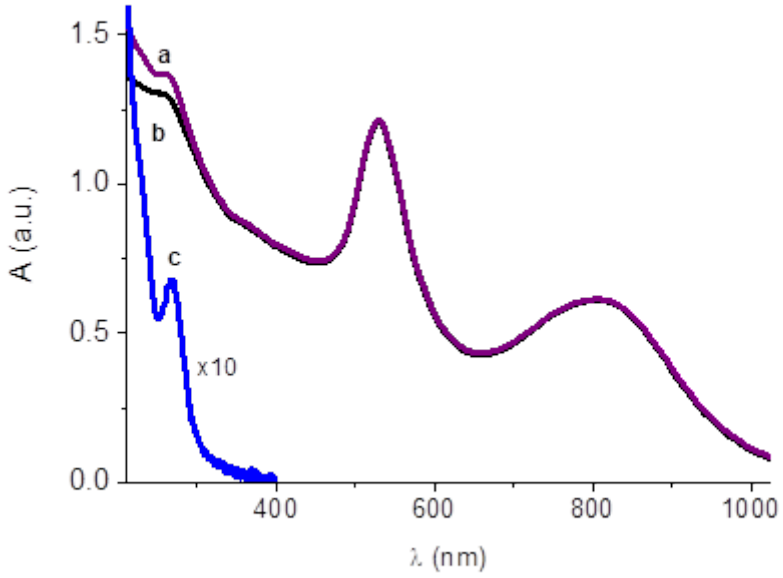

Figure 75: Absorption spectrum of an aqueous dispersion of Au@PolyCD after **(a)** and before **(b)** overnight stirring with a thin film of SRB. Difference absorption spectrum between a and b **(c)**, multiplied for a factor of 10 for the sake of clarity.

Interestingly, the LSPR bands of the spectrum remained unvaried after the overnight stirring, accounting for no interference of the drug with the optical and photothermal features of NPs. For the sake of control, the temperature changes upon 808 nm CW laser were registered for Au@Poly-CD@SRB too: no sensible differences might be outlined if compared with Au@Poly-CD, as Figure 76 A reports. Moreover, the complex stability upon light irradiation was testified by the absorption spectra, recorded before and after the latter photoirradiation, showing no modifications (see Figure 76 B).

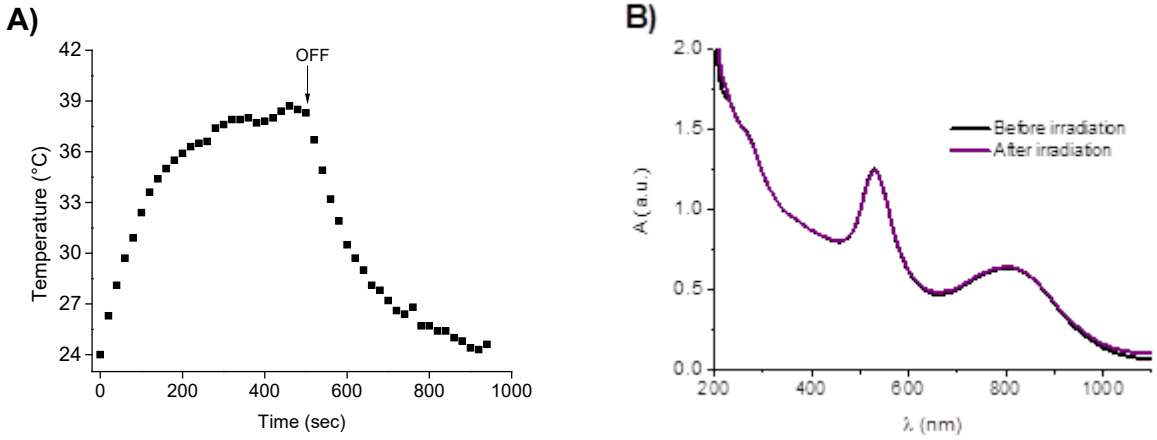

Figure 76: A) Temperature changes observed upon 808 nm CW laser irradiation (6 W cm^{-2}) of the Au@PolyCD@SRB complex; **B)** Absorption spectra recorded before and after the irradiation.

DLS analyses were carried out to monitor the dimensions of the NPs after SRB encapsulation. As shown in Figure 77, only a slight increase in the size, from *ca.* 50 to *ca.* 60 nm, may be mentioned after the drug complexation.

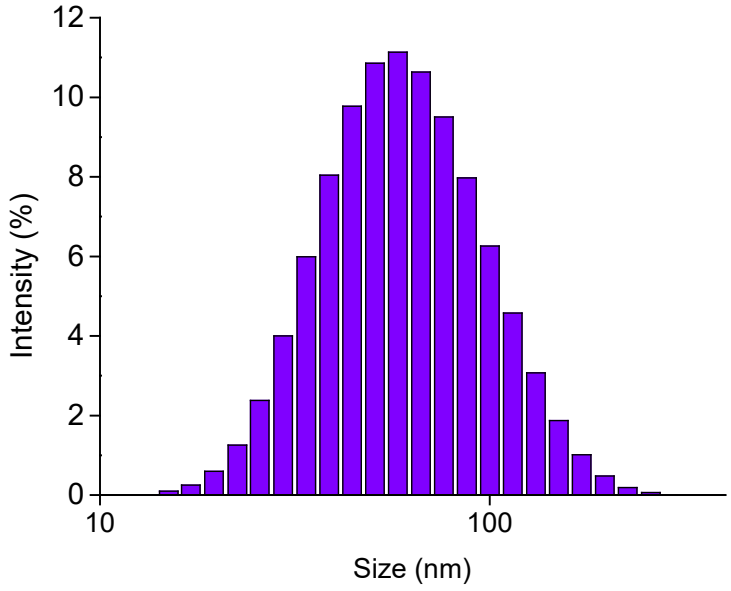

Figure 77: Size distribution of Au@Poly-CD@SRB measured by DLS.

2.5.6 Encapsulation of the NO Photodonor

Rhod-NO was chosen as unconventional therapeutic agent to be encapsulated within Poly-CD while capping the Au NPs.

The formation of the new host-guest supramolecular complex, henceforth Au@Poly-CD@Rhod-NO, was obtained by stirring the Au@Poly-CD aqueous solution with a thin film of the NOPD, and then ascertained through the absorption analysis (see Figure 78). The typical band of the chromophore Rhodamine appeared, very similarly to what it had been observed for the same compound incorporated within Poly-CD alone. Nonetheless, differently to what it had been observed for SRB, the complexation of Rhod-NO led to notable changes in the plasmonic spectral propertied of Au NPs. Indeed, both the Vis and NIR plasmonic absorption bands underwent to shifts towards longer

wavelength and to a decrease in intensity. This consequence was actually predictable, since it often occurs for dyes adsorbed in close proximity to Au nanoobjects when their absorption spectra strongly overlap. It may be explained as the result of a strong coupling between the molecular resonance of the dye (in this case Rhodamine) and the plasmonic resonance of Au [126].

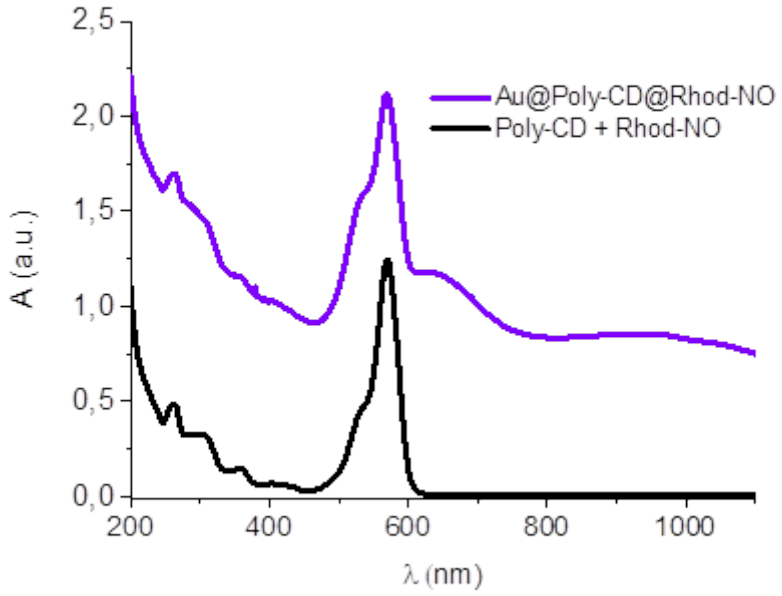

Figure 78: Absorption spectra of an aqueous dispersion of Au@Poly-CD after stirring overnight with a thin film of Rhod-NO and, for comparison, of a solution of Poly-CD (2 mg/mL) encapsulating Rhod-NO (7 µM).

In agreement with other already-reported Rhodamine-based dyes adsorbed on Au nanostructures [127], the size of Au@Poly-CD@Rhod-NO resulted to be ca. 200 nm, which is ca. 4-fold bigger than the one of Au@Poly-CD (see Figure 79).

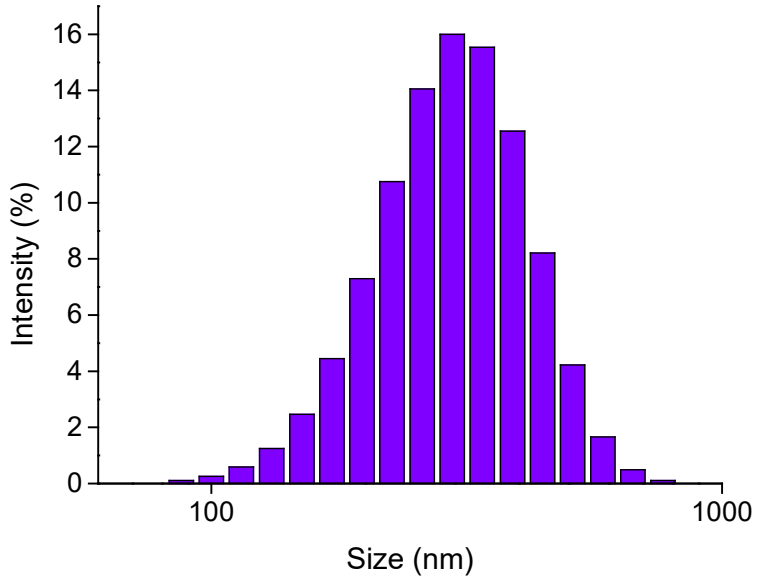

Figure 79: Size distribution of Au@Poly-CD@Rhod-NO measured by DLS.

The photoresponse of Au@Poly-CD-Rhod-NO was evaluated by monitoring the increase in temperature though the IR thermocamera and by observing the NO photorelease though the absorption spectral changes upon NIR and green light excitation (at λ_{exc} = 808 nm and 532 nm, respectively).

Interestingly, as it is reported in Figure 80, in spite of the 2-folds lower absorption in the NIR region, the complex with Rhod-NO exhibited a temperature jump profile comparable to the one observed in its absence (see Figure 74 for comparison).

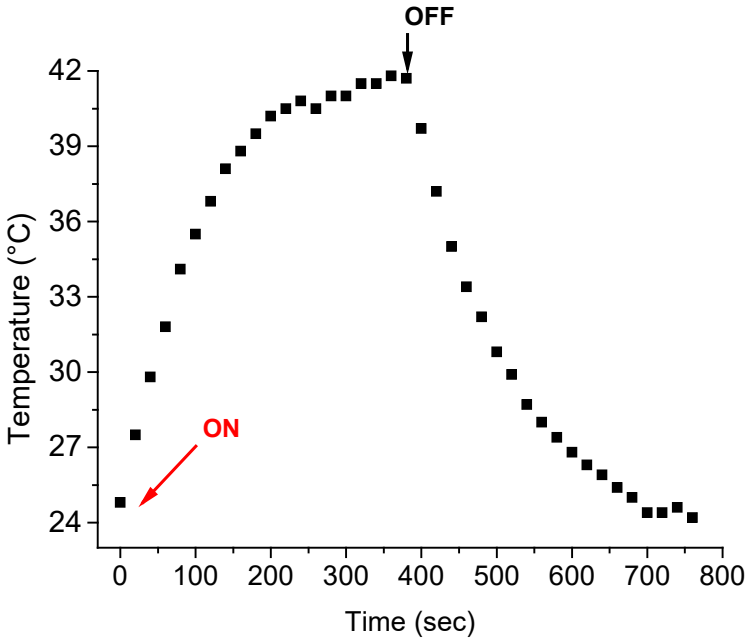

Figure 80: Temperature changes observed upon 808 nm CW laser irradiation (6 W cm^{-2}) for the aqueous dispersion of the Au@Poly-CD@Rhod-NO complex.

When the Au@Poly-CD@Rhod-NO complex was irradiated under green light, only the NOPD band showed significant changes, which, instead, did not affect the Au LSPR bands (see Figure 81). A new band was formed at ca. 400 nm and a bleaching was recorded at ca. 300 nm, together with fairly clear isosbestic points, representative for a clean photochemical reaction. This photochemical trend is in agreement with the one observed for irradiated Rhod-NO while releasing the radical specie, both when in free solution [83] and when encapsulated within Poly-CD, in the absence of Au NPs (see Figure 36).

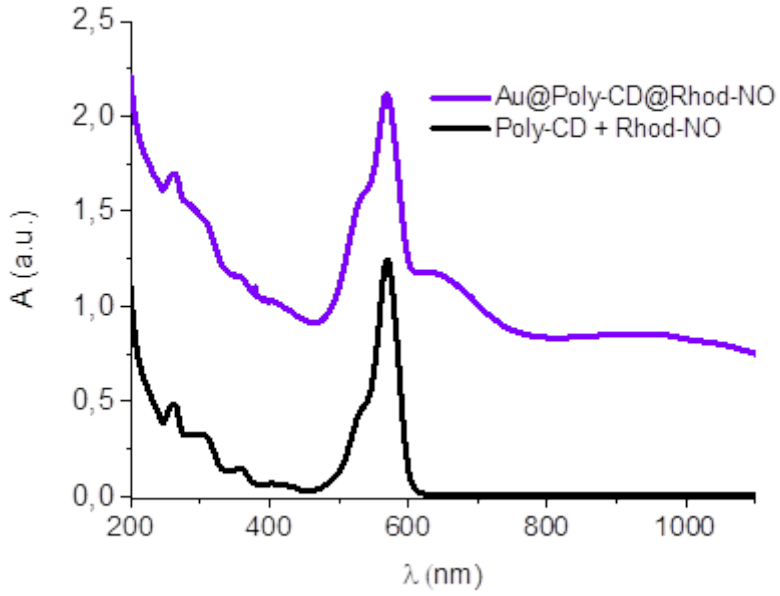

Figure 81: Absorption spectral changes observed from 0 to 55 min upon λ_{exc} = 532 nm CW laser irradiation (6 W cm^{-2}) of the aqueous dispersion of Au@Poly-CD@Rhod-NO.

2.5.7 *In vitro* tests over hepatocarcinoma cells line (Hep-G2)

Since Au@Poly-CD and its supramolecular complexes with SRB or Rhod-NO demonstrated good stability in culture *medium* for more than one week, as evidenced by the unaltered UV-Vis-NIR absorption profile and intensity, preliminary *in vitro* tests over Hep-G2 tumoral cells were carried out to evaluate the anticancer properties.

As Figure 81 illustrates, Au@Poly-CD led to a moderate reduction in cell viability in the dark, but its action over Hep-G2 drastically increased upon NIR light irradiation, thanks to the photothermal effect induced by Au. Cell mortality further grew in the case of Au@Poly-CD@SRB, thanks to the action of the antitumoral drug, despite its very low encapsulated amount (a concentration of ca. 1.5 µg/mL was used, which is below the IC_{50} value, 3.8 µg/mL, as already reported in Figure 18). The NIR irradiation of the latter complex caused the death of ca. 80% of the tumoral cells, probably due to the synergism between SRB and the phototermal effects. When cells were treated with Au@Poly-CD@Rhod-NO and kept in the dark, the observed impact was very similar to the one of Au@Poly-CD. When it came to light experiment, Hep-G2 were selectively irradiated with 808 nm or 532 nm laser, in order to trigger photothermia or NO release, respectively. They were obtained satisfying results, but the most successful ones were observed upon double irradiation, probably thanks to

the synergism between photothermal and photodynamic actions. It is worthwhile to underline that the shift of the green plasmon absorption of Au beyond 600 nm, occurred after the Rhod-NO encapsulation, had made the NOPD the main absorbing compound at 532 nm. This feature ruled out the hypothesis that an additional Au NPs photothermal effect might have caused the increase in cells mortality. Upon green light irradiation, indeed, only 5 °C increase was observed.

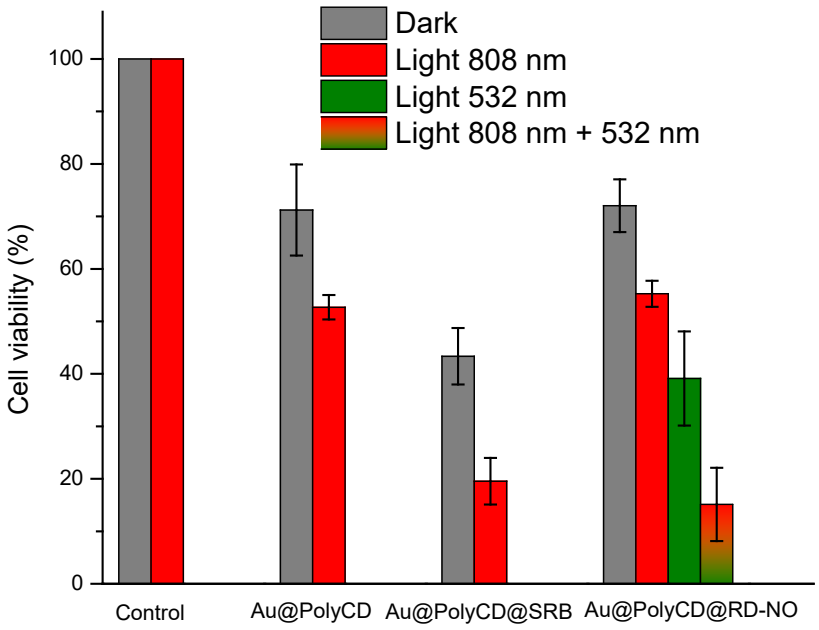

Figure 82: Cell viability observed 24 h after incubating Hep-G2 hepatocarcinoma cells with free aqueous dispersion of Au@Poly-CD, Au@Poly-CD@SRB and Au@Poly-CD@Rhod-NO in the dark and upon different irradiation conditions (occurred after the first 4 h of incubation) for 15 min.

2.5.8 Conclusions

It was shown a simple and eco-friendly procedure, based on PSE as a reductant to obtain plasmonic Au nanostructures with LSPR in the NIR spectral region and stabilized by a highly biocompatible β-CD branched polymer. The spectral properties of these nanoconstructs allowed their photoexcitation in the therapeutic window at 808 nm, resulting in a significant photothermia. Thanks to the excellent host capability of the branched polymer, the obtained nanoconstructs were able to encapsulate in a noncovalent fashion a conventional chemo-therapeutic such as SRB and an NOPD activatable with the biocompatible green light. This led to intriguing supramolecular hybrid assembly conserving (i)

the nanodimensional character, (ii) the photothermal activity of the Au component, (iii) the anticancer action of the chemo-therapeutic and (iv) the NO photorelease properties of the NOPD. The suitability of these nanoassemblies in the prospect of multimodal anticancer applications has been demonstrated by preliminary experiments over Hep-G2 hepatocarcinoma cell lines, which revealed synergistic action between the cytotoxic species involved.

2.6 Photobehaviour of curcumin in biocompatible hosts: the role of H-abstraction in the photodegradation and photosensitization

2.6.1 Introduction

Curcumin (CUR), 1,7-bis-(4-hydroxy-3-methoxyphenil)-epta-1,6-dien-3,5-dione, is a yellow-orange pigment which derives from *Curcuma Longa* [128]. It has obtained growing interest among the scientific community owing to the huge variety of its medicinal properties, like anticancer [129], antioxidant [130] and wound healing [131] capabilities, but it is also widely employed for its beneficial effects in cardiovascular [132] and neurodegenerative diseases [133].

One of the most investigated effects of CUR is connected to its intense absorption in the blue region, which allows the interaction with Vis light. For this reason, CUR has been widely proposed a suitable PS for PDT [134][135]. Nonetheless, even if the light-induced biological effects are extensively reported in literature in many systems, there are not convincing evidences about the main species which are effectively responsible for these photoinduced phenomena. This lack in information clashes with the several studies, carried out in organic solvents and micellar systems, that have underlined the huge sensitivity of CUR in its photophysical and photochemical properties depending on the features of the microenvironment (polarity, H-bond, H-donating capability, *etc.*) [136] and the dominance of either the enolic or diketo form of its tautomeric equilibrium (see Figure 83) [137].

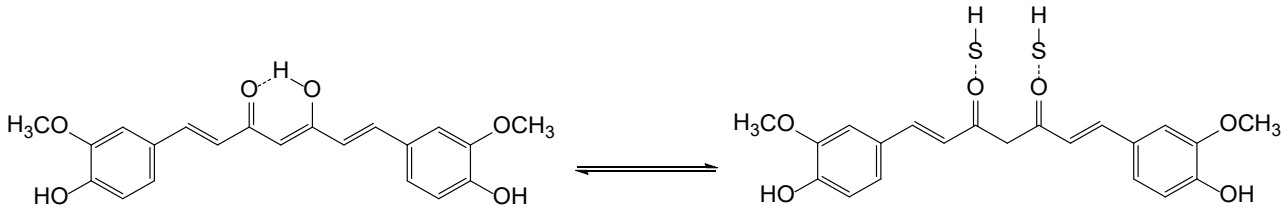

Figure 83: Equilibrium between the CUR enolic (on the left) and the diketo (on the right) forms. The latter is the prevailing form in the presence of H-bond donating solvents/substrates (SH).

CUR is basically water-insoluble: for this reason, several lipidic or polymeric vehicles have been developed, such as liposomes, microspheres, nanoparticles, solid dispersions, microemulsions, solid dispersions, and dendrimers [138–140] as suitable nanocarriers. These formulations manage to increase CUR bioavailability but do not consider its fate under light irradiation. For this reason, we have investigated the photochemical properties of CUR in different host environments, with the

purpose of getting insights into its photobehaviour in drug-delivery systems and of clarifying the mechanisms that stand behind the photobiological effects. It was conducted a spectroscopic and photochemical investigation on CUR formulated in Pluronic® polymeric micelles, microemulsions, and zein NPs, chosen as biocompatible nanocarriers, human serum albumin (HSA) as a representative biomolecule (see Figure 84) and also in dioxane and EtOH, for the sake of comparison, as examples of solvents with different features.

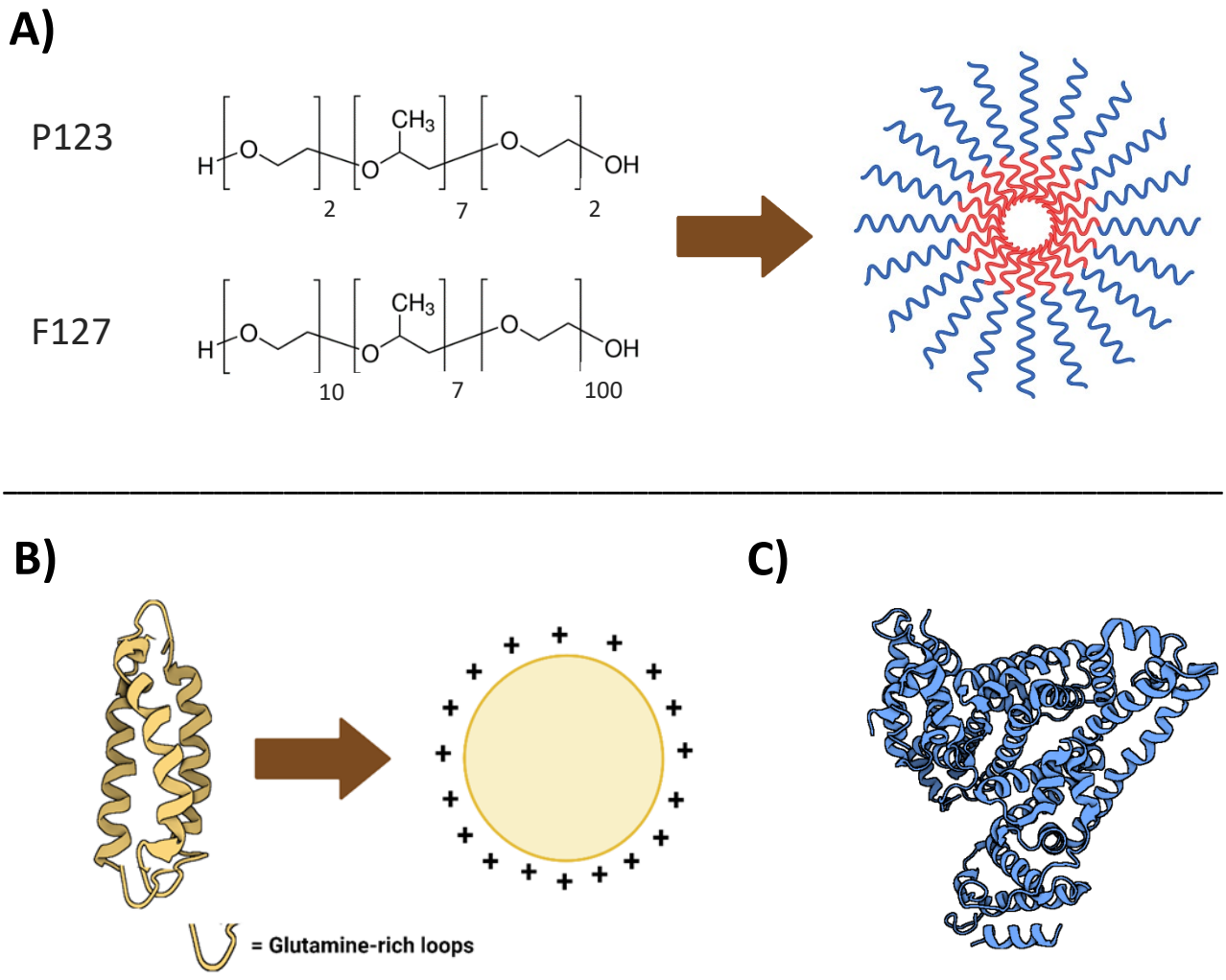

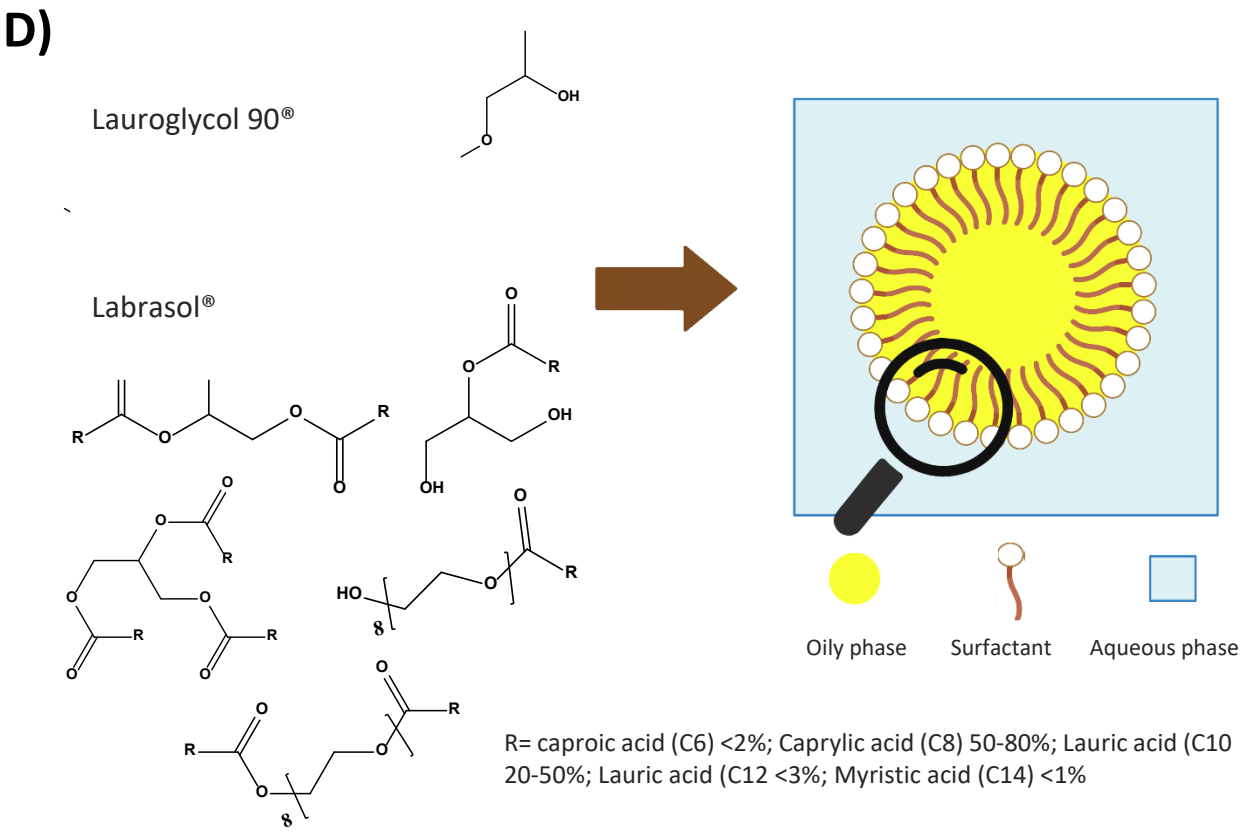

Figure 84: Schematic of the biocompatible nanocarriers used in this work and molecular structures of their components. **(A)** represents the Pluronic® polymeric micelles, **(B)** zein NPs, **(C)** HAS and **(D)** microemulsions.

2.6.2 Host systems

The host systems were synthetized in collaboration with the research group of Prof. Fabiana Quaglia (University of Naples, Italy).

Mixed micelles of Pluronic®, an oil/water (o/w) microemulsion, and nanoparticles (NPs) of Zein have been selected as representative nanocarriers able to incorporate lipophilic molecules with diverse structural characteristics. Pluronic® micelles are supramolecular structures with a hydrophobic core of polypropylene oxide able to host hydrophobic molecules and a surrounding shell of polyoxyethylene. Micelles prepared by a mixture of Pluronic F127 and P123 are less prone to dissociation in unimers upon dilution in aqueous media due to a lower critical micelle concentration than the single components [141]. The microemulsion formulation contains Labrasol® and Lauroglycol® FCC, two lipophilic components with well-known biocompatibility and surfactant properties able to act as a solubilizer for poorly soluble molecules. The o/w microemulsion is spontaneously formed under low mixing rates from Labrasol®/Lauroglycol® FCC mixture and water at appropriate ratios. The lipophilic components allow the solubilization of lipophilic compounds

that remain mainly confined in the oily phase. Both Pluronic® micelles and microemulsions share the common feature of being transparent to light and have been proposed as nanocarriers suitable for PDT with CUR [142]. Zein, a hydrophobic protein soluble in volatile organic solvents, gives colloidal dispersions of NPs with a typical positive surface due to the presence of glutamine loops in the primary protein structure. Zein NPs incorporate lipophilic molecules in the hydrophobic pockets, can be diluted in water, and scatter visible light as a function of their size, like many other polymeric NPs.

Table 1 reports the properties of the different biocompatible nanocarriers with CUR. The amount of CUR in the Pluronic® micelles and the microemulsion was adjusted to allow photophysical characterization, thus avoiding any sample dilution that could alter the structure of the nanocarriers and promote CUR precipitation. All the steps were carried out by protecting the sample from the environmental light. Pluronic® micelles prepared by the thin-film hydration incorporate CUR quantitatively, are small with low polydispersity, and are transparent to light. The composition of the prototype microemulsion containing Labrasol®:Lauroglycol® FCC: water at 20:2.5:77.5 v/v/v was based on the pseudo-ternary phase diagrams described previously [142], and the solubility of CUR in the oily phase. Remarkably, the microemulsion allowed the dissolution of CUR up to 1 mg/mL due to the solubility enhancer activity of the oily components.

The microemulsion is formed by tiny particles with a narrow size distribution and a slightly negative Z potential (ζ) and is transparent to light. Zein NPs show a larger DH with a low polydispersity and a positive ζ due to glutamine loops on the NP surface. The encapsulation efficiency of CUR in NPs was almost complete and the sample could be diluted in water without any change of size (data not shown).

NANOCARRIERS	D_H (nm)	PI	Z (mV)	CUR[A] (μg mL^{-1})
PLURONIC® MICELLES	28 ± 2.3	0.198 ± 0.05	- 0.7 ± 0.9	10
MICROEMULSION	29 ± 0.2	0.264 ± 0.02	- 0.1 ± 0.6	10
ZEIN NPS	124 ± 11	0.174 ± 0.07	+48 ± 3	82[b]

Table 1: Properties of CUR-loaded nanocarriers. Results are reported as the mean of three separate measurements on three different batches ± standard deviation (SD).
[a] CUR concentration in the as prepared samples. [b] Evaluated by the direct and indirect method as specified in 4.3. SD of CUR amount was 82 ± 1 μg mL^{-1}.

2.6.3 Spectroscopic characterization

As mentioned in the Introduction, the prevalence of the diketo or the enolic form of CUR in its tautomeric equilibrium is strictly dependent on both the microenvironment polarity and H-bond capability.

In Figure 85 A they are shown the normalized UV-Vis absorption spectra of CUR encapsulated within Pluronic® polymeric micelles, an o/w microemulsion, and Zein NPs, associated with HSA and, for comparison, solubilized in dioxane and EtOH. As it is evident, in dioxane, a solvent with no H-bond capability, the main absorption band, well structured, has a maximum at 420 nm and two shoulders at 400 and 440 nm, respectively. According to literature [143–146], these features are similar to those observed for CUR solubilized in other aprotic solvents and are due to the exclusive presence of the enolic form at the ground state.

When observing the spectrum in EtOH, which is a more polar solvent with H-bonding capability, it is clear the loss in vibronic structure of the main band, which broadens and red-shifts. These changes are explainable with intermolecular H-bonds formed with the solvent, prevailing on the intra-molecular ones, and shifting the equilibrium (see Figure 83) towards the diketo form [143–146].

The absorption spectra of CUR within Pluronic®, micelles and microemulsions show a significant broadening and red-shift if compared to the absorption profile in dioxane, but still maintains some vibronic structure, which, on the contrary, is almost completely lost when CUR is encapsulated within Zein NPs and HSA and is accompanied by an absorption extending beyond 500 nm.

Figure 85 B reports the normalized CUR fluorescence emission spectra. As it was observed for the absorption spectra, the emission profile in dioxane exhibits a vibrational structure that is lost in EtOH, where the emission band is, in this case too, significantly broadened and red-shifted. The fluorescence in the Pluronic® micelles and in the microemulsion is comparable, with the absence of any vibrational structure and displaying a broadening of the emission band and a red-shift compared to that in dioxane. When CUR is encapsulated in zein NPs and HSA, the emission band is even more broadened and red-shifted (*ca.* 15 nm). Anyway, the effects observed are less noticeable than those observed in ethanolic solution.

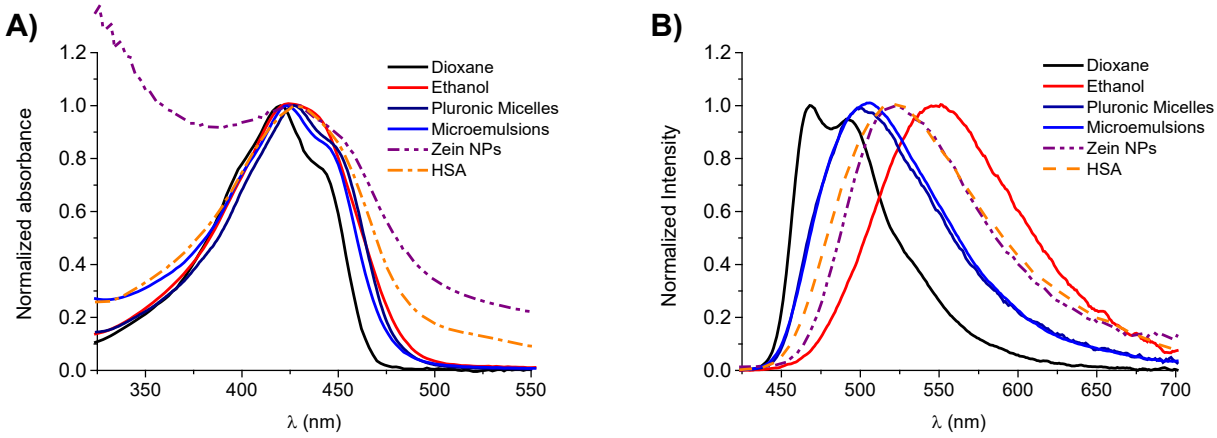

Figure 85: Normalized **(A)** absorption and **(B)** fluorescence emission (λ_{exc} = 400 nm) spectra of CUR in different solvents and host systems. *T* = 25 °C.

Overall, this spectroscopic scenario is very similar to that reported for CUR either solubilized in dioxane-water mixtures with variable water content [147] or encapsulated in surfactant micelles of TX-100 [146]. It suggests that CUR is confined in a quite hydrophobic microenvironment but can form, more likely, intermolecular H-bonds with water molecules at the interface, confined within the host systems, or both. As it regards zein NPs and HAS, the less structured spectral shape and the huger red shift of the absorption profiles may be due to the additional participation of H atoms of the protein scaffolds in intermolecular H-bonds with CUR, according to the well-established binding of CUR with hydrophobic pockets of albumins [148–150]. In these cases, the additional absorption extending beyond 500 nm is reasonably related to a small population of deprotonated CUR, as already reported in literature [146] and, only for zein NPS, to their typical scattering too.

Taking all together these data, it is fairly suggested that all the analysed hosts shift the CUR tautomeric equilibrium towards the diketo form, which is present in considerable amount under these experimental conditions.

They were performed steady-state photolysis experiments under anaerobic conditions, by exciting the host-guest complexes under visible light. All the examined systems showed very similar results, with a significant bleaching of the main absorption band in the visible region, slight increase at *ca.* 330 nm and a not very clear isosbestic point at *ca.* 360 nm. From this finding, it could be deduced that all these photodecomposition processes own a similar nature.

Figure 86 A reports representative spectral changes observed for CUR within Pluronic® micelles. The rate of photobleaching, showed in Figure 86 B, and monitored at the maximum absorption of each sample and calculated at early stages of the photoreactions, is comparable for polymeric micelles and microemulsions, but significantly smaller (*ca.* 4-5-fold) in the case of zein NPs and HSA. It is necessary to underline that such a result cannot be trivially attributed to different amounts of photons absorbed by the different samples as, in all the cases, the differences in absorbance at the excitation wavelength are below 5%.

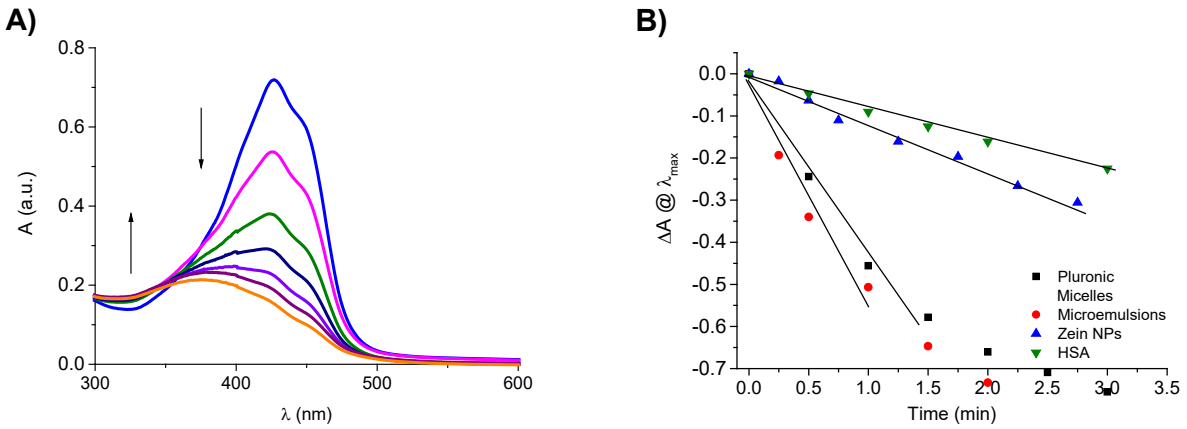

Figure 86: Normalized **(A)** absorption and **(B)** fluorescence emission (λ_{exc} = 400 nm) spectra of CUR in different solvents and host systems. T = 25 °C.

It is widely known that the triplet state of a suitable PS is the key intermediate for a successful photodynamic action. In the case of CUR, the triplet state behaviour can drastically change depending on the predominance of either the enolic od diketonic form and on the presence of a microenvironment with abstractable H-atoms. In their excellent paper, Ortica and Rodgers well explained the different triplet dynamics of CUR [147]. They elegantly demonstrated that, when CUR

is in a solvent with abstractable hydrogens but that does not allow intermolecular H-bonds (*i.e.,* dioxane), the enolic form dominates: it does not behave like a typical carbonyl compound *viz* hydrogen abstraction by the triplet state. On the other hand, when intermolecular H-bonding to solvent occurs (*i.e.*, adding water to dioxane) and the diketo fom is present, CUR behaves like a typical carbonyl compound: hydrogen abstraction by the triplet state takes place from solvents with abstractable H atoms (*i.e.*, dioxane or alcohols) [147]. The spectroscopic features in Figure 85 showed and above-discussed clearly indicate that in all the investigated systems, the diketo form of CUR is present in good amounts. Furthermore, all the considered host systems are rich in many easily abstractable H atoms. Therefore, taking into account all these considerations, it was deduced that the H-abstraction from the triplet state of CUR may occur in all cases. As Figure 87 illustrates, the photoreduction process leads to the formation of a ketyl radical as a key intermediate in the CUR photodecomposition process and subsequent stable photoproducts in which the chromophore conjugation is lost, in perfect agreement with the photobleaching that is observed.

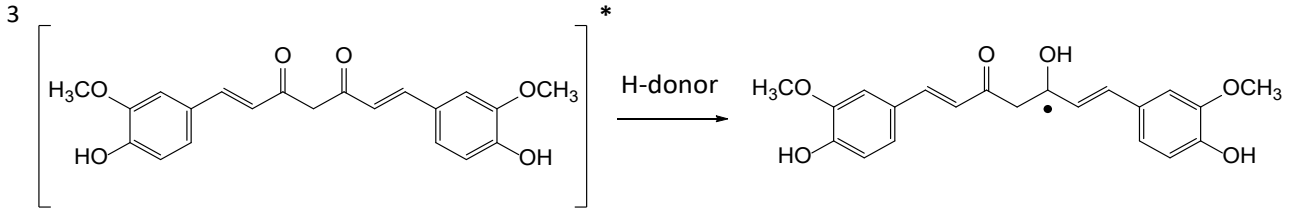

Figure 87: Scheme of the hydrogen abstraction from the host systems by the triplet state of the diketo form of CUR leading to the generation of a ketyl radical.

CUR has been widely proposed in literature as a suitable PS for PDT [134,135,151]. In this type of treatment, $^1O_2$ is the most active cytotoxic species, formed through a collisional energy transfer mechanism between the triplet state of the PS and the surrounding molecular oxygen (See Introduction section). Anyway, acceptable quantum yields for $^1O_2$ generation, Φ_Δ = 0.11, has been reported only in non-polar and not H-boning solvent [143]. This value falls by more than one order of magnitude in EtOH [143] and an average value of Φ_Δ = 0.04 has recently been reported for CUR embedded in liposomes [152]. Thus, in this work it was investigated the photogeneration of $^1O_2$ by CUR within the host systems and, for the sake of comparison, in dioxane as a reference solvent. The most efficient method to detect $^1O_2$ is the direct monitoring of its typical and diagnostic phosphorescence in the near-IR spectral window, with a maximum at 1270 nm [24]. As Figure 88

reports, a clear $^1O_2$ luminescence was detected for CUR dissolved in dioxane, where the enolic form predominates, whereas no detectable signal was revealed in any of the investigated systems. These data suggest that the H-abstraction process is the most likely deactivation pathway of the triplet state of the diketo form and is in great agreement with literature results, reporting no formation of the radical species by CUR encapsulated in different types of micellar systems [143]. The lack in $^1O_2$ photogeneration may also be due to the lifetime of the CUR triplet state in the hosts, short enough to make the diffusional quenching by oxygen not competitive with the triplet decay (see next session).

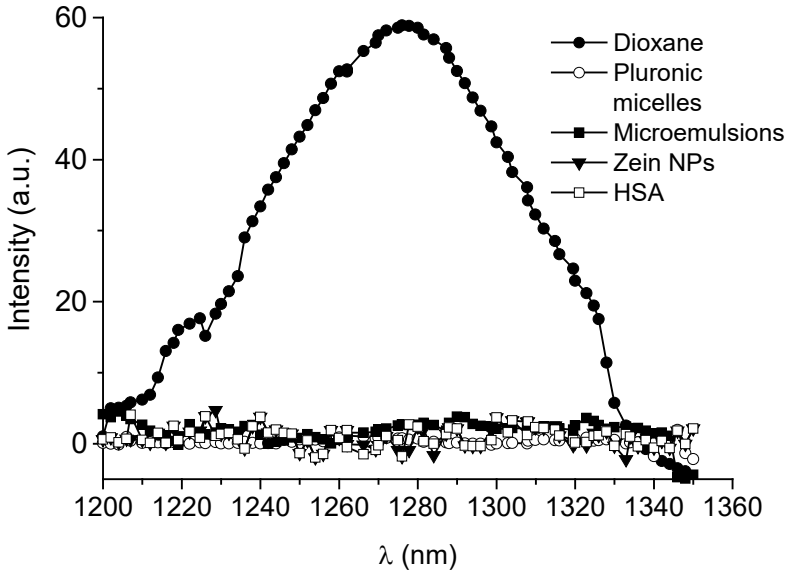

Figure 88. $^1O_2$ luminescence detected upon 405 nm light excitation of solutions of CUR (10 μg/mL) in dioxane and host systems in D_2O. *T* = 25°C.

2.6.4 Nanosecond Laser Flash Photolysis

Nanosecond laser flash photolysis is a powerful tool for acquiring spectroscopic and kinetic information into photochemically generated transient intermediates. Figure 89: Figure 89 reports the transient absorption spectra recorded at different delay times after 355 nm pulsed laser excitation of optically matched samples of CUR dissolved in dioxane, as a reference solvent, and embedded within the various host systems in aqueous solutions. The spectrum in dioxane (see Figure 89 A) exhibits a broad absorption band extending beyond 700 nm and its decay is not accompanied by the concomitant formation of any transient. The decay is mono-exponential, with

a K_{obs} ~ 3.3 x 10^5 s^{-1} (see inset Figure 89 A) and is remarkably quenched by oxygen with a quenching constant $k_q(O_2)$ ~ 1 x 10^9 M^{-1} s^{-1}. According to the literature [147,153], these spectral and kinetic features are unambiguously typical of the lowest triplet state of CUR, which, in this solvent, is exclusively present in the enolic form. Moreover, the observed quenching in the presence of oxygen is in perfect accordance with the photogeneration of $^1O_2$ reported in Figure 88.

It is worthwhile underlining that, in all cases in which CUR is within the host systems, its excitation gives ride to a transient absorption at the earlier delay time compared with the laser pulse, characterized by a maximum at *ca.* 490-500 nm and a broad absorption extending in the red region (Figure 89 B-E). These spectral features matches very well to that ones observed by Ortica and Rodgers when CUR was excited in a mixture of dioxane water 1:1 (v:v) and had been assigned by the authors to the ketyl radical produced after the H-abstraction by the diketo-form, which is the dominant one in this solvent mixture, of CUR triplet state from dioxane [147]. Based on these similarities, in our case, the transient observed may be attributed to the ketyl radical generated after H-abstraction by the CUR triplet state from the host systems, which are rich in several abstractable H atoms to be offered. This scenario well agrees with the huge abundance of the CUR diketo tautomer, which is indispensable for the H-abstraction to occur and which is demonstrated by the steady-state absorption spectra and emission data (see Figure 85).

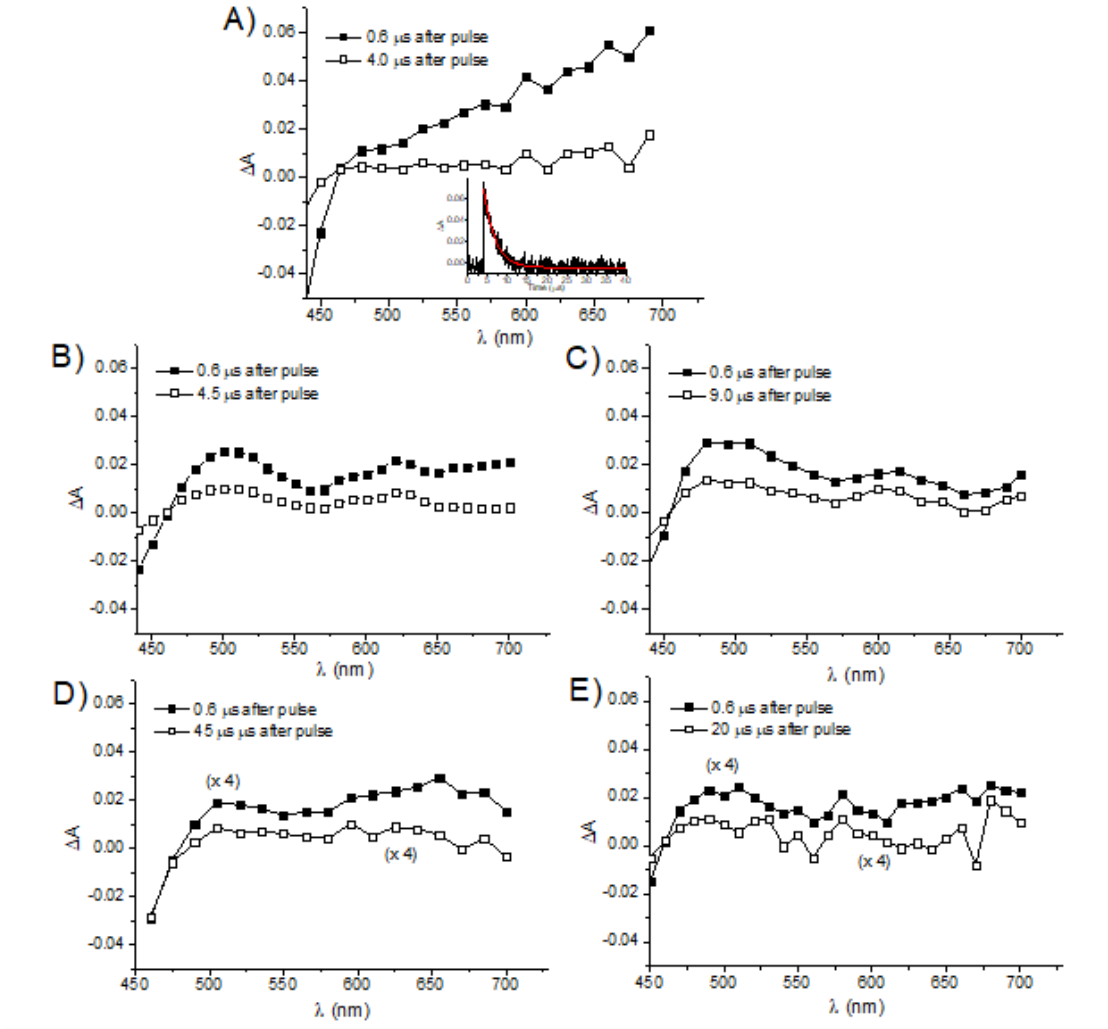

Figure 89: Transient absorption spectra obtained upon 355 nm laser excitation (E_{355} 10 mJ pulse^{-1}) of optically matched N_2-saturated samples of CUR (A_{355} ~ 0.3) and recorded at different delay times of the laser pulse. CUR in dioxane; the inset shows the decay trace and the related first-order fitting monitored at 700 nm **(A)**. CUR in Pluronic® micelles **(B)**, the microemulsion **(C)**, zein NPs **(D)** and HSA **(E)**. For clarity, the spectra of samples **(D)** and **(E)** have been multiplied by a factor 4.

The lack of the transient absorption of the CUR triplet state in the host systems, observed at 0.6 μM after the laser pulse, accounts for a triplet lifetime shorter than 0.6 μM. This data is in perfect agreement with the inefficient production in $^1O_2$ by CUR within the investigated systems. Indeed, even if it was estimated an upper limit for the triplet decay of 0.6 μM, with a diffusion-controlled quenching constant of the triplet state by oxygen (*ca.* 10^9 M^{-1} s^{-1}), the fraction of triplet state quenched by the surrounding oxygen within the solution (*ca.* 2.6 x 10^{-4} M) would be *ca.* 10%, that is basically an almost complete inefficient photosensitization of $^1O_2$. It may be also believed that the short value of the CUR triplet state under our experimental conditions could be not only the result

of the H-abstraction, but also of the solvent effect of water molecules, which are inevitably present at the periphery or inside the host systems, on the keto-enolic equilibrium. This hypothesis in in agreement with what Ortica and Rodgers had already proposed, since they had observed a constant decrease of the CUR triplet lifetime upon increasing the water amount in the dioxane:water mixtures, finally reaching a limit value below 0.01 μs, observed in a 1:1 (v:v) mixture [147].

The intensity of the transient absorption of the ketyl radical generated is another interesting aspect to be highlighted. Inspection of the transient spectra of Figure 89 B-E. recorded 0.6 μs after the light pulse, exhibits quite comparable absorbance values in the case of pluronic micelles and microemulsions, and values *ca.* 4-5-fold smaller in the case of zein NPs and HSA. Since in all samples the CUR absorption at the excitation wavelength is very similar and relevant differences in the extinction coefficient of the ketyl radical in the different hosts are very unlikely, the differences observed in the transient absorption may be reasonably attributed to different amounts of the ketyl radical generated in the different samples. Such differences are in great agreement with the rate of the photobleaching observed in the steady-state photolysis experiments, reported in Figure 86, which showed comparable rates for Pluronic® micelles and microemulsions, while values *ca.* 4-5-fold smaller for zein NPs and HAS were found. This comparison supplies strong evidence for the H-abstraction being the main photodeactivation process of the CUR triplet state encapsulated in the hosts. The different efficiency in photoreactivity can be tentatively attributed to a reduced yield of intersystem crossing (ISC) of CUR in the protein-based hosts. This is not surprising if it is considered that the confinement of many drugs in specific hydrophobic pockets, with more steric constraints compared with micelles and microemulsions, have demonstrated to favour other deactivation pathways from the singlet state competitive with ISC (i.e. fluorescence) [148]. For CUR this evidence has already been reported when complexed with albumin [141] and other systems mimicking the hydrophobic pockets of proteins, such as cucurbituril [149] and cyclodextrins [150], in which a significant increase of fluorescence has been reported.

Figure 90 illustrates the decays of the ketyl radical. In all cases, it was observed the largest part of the decay being mono-exponential, with lifetimes of *ca.* 7.5 μs in Pluronic micelles and microemulsions (Figure 90 A, B) and *ca.* 20 μs in Zein NPs and HSA (Figure 90 C, D). The ketyl radical

decay is shown to be quenched by oxygen (traces b in Figure 90), except in zein NPs.

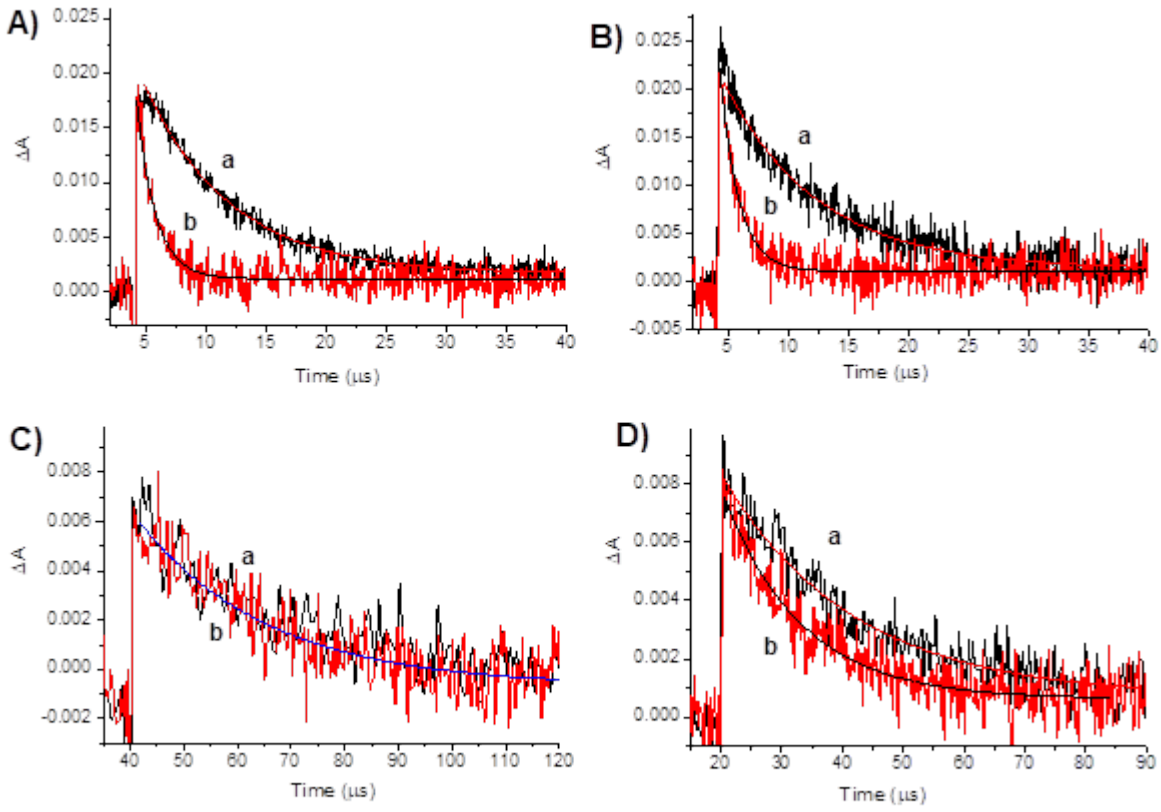

Figure 90: Decay profiles and related first-order fittings of the ketyl radical generated upon 355 nm laser excitation (E_{355} 10 mJ pulse^{-1}) of aqueous suspension of CUR (50 μM) encapsulated in Pluronic micelles (A), microemulsions (B), Zein NPs (C) and HSA (D) and recorded in N_2-saturated (a) and air-equilibrated conditions (b).

The bimolecular constants, $k_q(O_2)$, were estimated by equation (1):

$$k_{obs} = k_0 + k_q(O_2)[O_2] \quad (1)$$

where k_{obs} and k_0 are the experimental values for the pseudo-first and first-order decay of the ketyl radical observed under air-equilibrated and N_2-saturated conditions, respectively, and $[O_2]$ is the concentration of oxygen (*ca.* 2.6x10^{-4} M). It was obtained kq(O_2) *ca.* 1 x 10^9 M^{-1} s^{-1} in the case of Pluronic micelles and microemulsions, and ca. 1 x 10^8 M^{-1} s^{-1} in the case of HSA. While the latter agrees with those typically expected for a CUR derived resonance-stabilized carbon centred radical [147,154], the former is quite surprising. It may be considered that such a quenching constant can be

overestimated due to the larger oxygen concentration really present in the highly hydrophobic microemulsions and polymeric micelles which, of course, affects the calculation of $k_q(O_2)$ by (1). As far as the lack of quenching observed in the case of zein NPs is concerned, this might be the result of the more densely packed structure of this type of NPs compared with HSA, which significantly hinder either access or diffusion of oxygen to the radical centre. Such an effect is not uncommon and has been frequently observed for oxygen-sensitive transient species confined within very restricted microenvironments [148].

Overall, these results demonstrate that in all the host systems the well-known general mechanism typically observed for the aromatic ketone triplets (i.e. benzophenone) confined in host systems with H-abstractable hydrogens [154–157], may also apply for CUR triplet, as summarized in Figure 91 and discussed below.

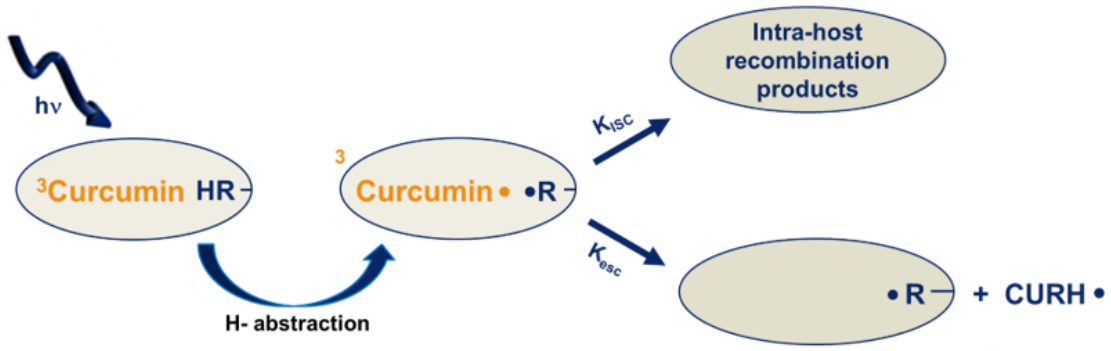

Figure 91: Primary photochemical processes of CUR in the host systems investigated. R is the host component with abstractable H atoms.

H-abstraction by the CUR triplet state takes place inside the host systems and leads to the formation of triplet radical pairs, the ketyl radical (CURH•) and a host-confined carbon-centered radical (R•). After ISC, they can form intra-host covalent recombination products. Besides, the ketyl radical can escape the host, thus the germinate nature of the radical pair is destroyed. According to literature, the first-order decay of the ketyl radical observed in our case (k_{obs}) corresponds to the sum of the k_{ISC} and k_{esc} processes [154]. This interpretation accords well with the observation that, despite radical-radical combination reactions in homogeneous solution are usually bimolecular and second-order, these decay processes in confined spaces such as micelles, polymeric matrices or cyclodextrin cavities are still bimolecular, but they follow first-order kinetics [154,157–159]. As reported in the

seminal papers by Scaiano *et al.* [158] although the germinate radical pair is destroyed by the escape of the ketyl radical, the absorption of the ketyl radical chromophore is not destroyed too: in principle, it can be detectable over longer time scales. The kinetic traces observed in our cases show only a small residual absorption after the first-order kinetics were completed. This can be due to either only a small fraction of ketyl radical really escaped or to a fast formation of decomposition products occurring in the bulk solution.

When oxygen is present, the quenching on the ketyl radical decay turns to be, of course, competitive with the formation of intra-host recombination product. In our case reaction with molecular oxygen leads more likely to the formation of the peroxyl radical CURHOO•, which, in principle may also eliminate the hydroperoxyl radical HOO•, according to what already observed for other ketyl radical derivatives [160]. Of course, peroxyl radicals are inevitably formed also through reaction of oxygen with the host-confined carbon-centred radical R• which, in contrast to CURH•, has a very low translational mobility.

2.6.5 Conclusions

In the presented study it was investigated the photobehaviour of CUR encapsulated in different host systems, such as polymeric micelles, microemulsions, zein NPs, and HSA and, for comparison, in organic solvents like dioxane and ethanol. It was underlined the importance of the microenvironment in dictating the CUR behaviour upon light excitation. In all the host microenvironments, CUR has demonstrated to be largely present in the diketo tautomeric form, due to favourable intermolecular H-bonding with water molecules present in the formulations and, in the case of the protein-based systems, probably also with H-bonding protein components. In contrast to the enolic form, the diketo tautomer exhibits the typical reactivity of carbonyl compound *viz* hydrogen abstraction by the triplet state, leading to the formation of the CUR-derived ketyl radical due to the large presence of easily abstractable H atoms present in the host systems explored. A large part of this radical recombines with the counterpart host-confined radical produced after H-abstraction, generating intra-host covalent products and, in the presence of oxygen, is oxidized by molecular oxygen, generating more likely peroxyl radical species. H-abstraction leads to the loss of the highly conjugated structure of the CUR chromophore, leading to UV-absorbing stable products responsible for the photobleaching observed upon steady-state irradiation. The photobleaching rate is in good agreement with the amount of the ketyl radical detected with time-resolved experiments indicating that the H-abstraction is the primary process

responsible for CUR photodecomposition. The triplet state of CUR is short-lived because of a combination of the effective H-abstraction reaction and the solvent effect of water molecules present in the hosts on the keto-enolic equilibrium. This makes the triplet state quenching by molecular oxygen inefficient, resulting in the lack of $^1O_2$ photogeneration. Taking into account that polymeric micelles, microemulsions, and zein NPs can be considered not only carrier systems to solubilize and deliver CUR, but also biological mimicking media, the above-discussed findings suggest a scenario in which the photodynamic inactivation of bacteria or cancer cells induced by CUR, maybe is not mediated by $^1O_2$, as extensively reported without direct evidence on its photochemical generation. Rather, cytotoxic effects initiated by H-abstraction processes, in which the role of peroxyl radical thereafter formed by the reaction with molecular oxygen can be crucial, need to be considered.

The results obtained also deserve some comments regarding the actual view of CUR as PS. Some of the ideal pre-requisites for a good PS include i) strong absorption in the red region, ii) high ISC to triplet and high $^1O_2$ quantum yields, iii) low tendency to auto-oxidation by $^1O_2$ and iv) preferable water solubility [22,161,162]. CUR does not possess any of these features. In fact, it shows i) absorption confined to the not biologically relevant blue spectral window with absorption molar coefficient smaller than those exhibited by typical photosensitizers such as porphyrin and BODIPY derivatives [143]; ii) small, upper limit for ISC and $^1O_2$ quantum yields of ca. 0.1 only in organic solvents such as toluene, benzene and acetonitrile, values that drop significantly down in more polar and H-bonding solvents [144]; iii) high reactivity with $^1O_2$, comparable with that of typical antioxidants [163]; iv) very low solubility in aqueous media. Based on these evidence, it might be reasonable to take some precaution before considering CUR as a suitable PS and if it really deserves such a high reputation and attention from the scientific community.

Also, the widespread CUR formulations for topical applications as a remedy for the prevention and treatment of skin aging and disorders might raise serious doubts. Accumulation of CUR in the skin leads to direct absorption of the environmental light and, as recently also emphasized by Becker and coworkers [164], can lead to a more serious phototoxic effect when localized in a lipophilic environment. Considering that many formulations possess some features common to those of the carrier systems investigated herein, the use of CUR, and the potential of adverse, uncontrolled, and undesired CUR side effects triggered by light on patients cannot be underestimated. Therefore, the skin application of CUR is advisable to be avoided, or at least one should pay attention to exposure to environmental light.

2.7 Dextrans polymer functionalized with BODIPY-based NO Photodonor

During the six months stay in Almería, it was drawn up a research plan focused on the synthesis of a novel fluorescent dextrans polymer, functionalized with an NOPD exploiting BODIPY as a green light triggering antenna and simultaneously assembling conventional drugs (see Figure 92).

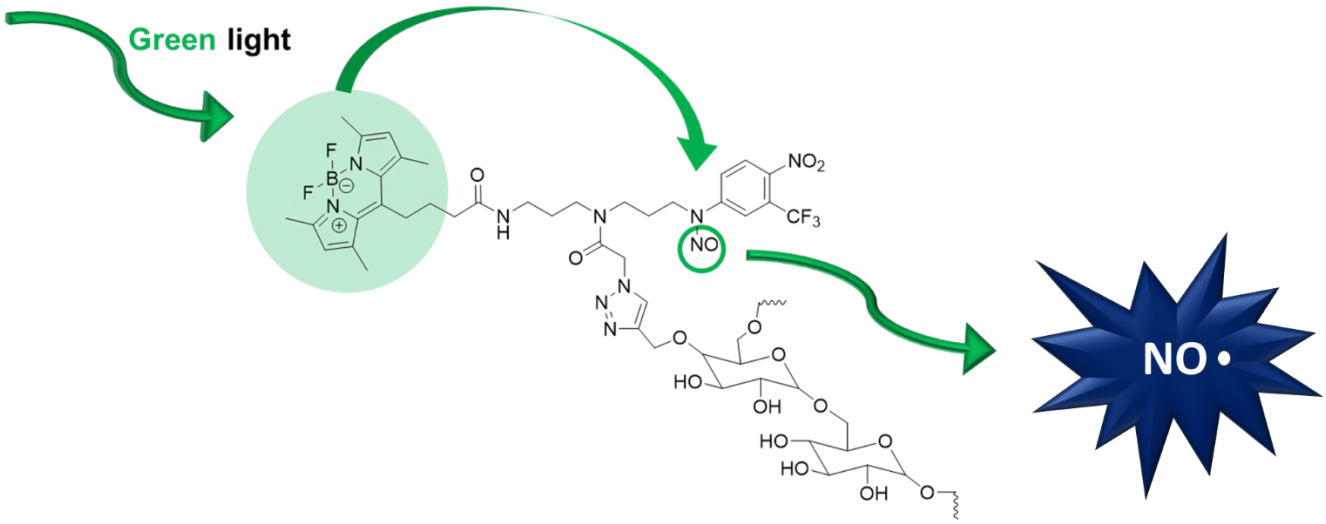

Figure 92: Projected novel construct consisting of a dextrans polymer functionalized with a BODIPY-based NOPD.

Very similarly to what has already been reported in literature [83], the N-nitroso-moiety of the NOPD will be linked to the fluorescent, light harvesting BODIPY antenna through a suitable spacer. The novel polymeric system will be able to release NO under strict control of the very biocompatible green light. Moreover, the fluorescent properties of BODIPY in the green spectral region will be potentially exploited to monitor the uptake of the novel system in the cellular environment.

Preliminary synthesis steps of the NOPD-functionalized polymer have been carried out, following the synthetic strategy shown in Figure 93.

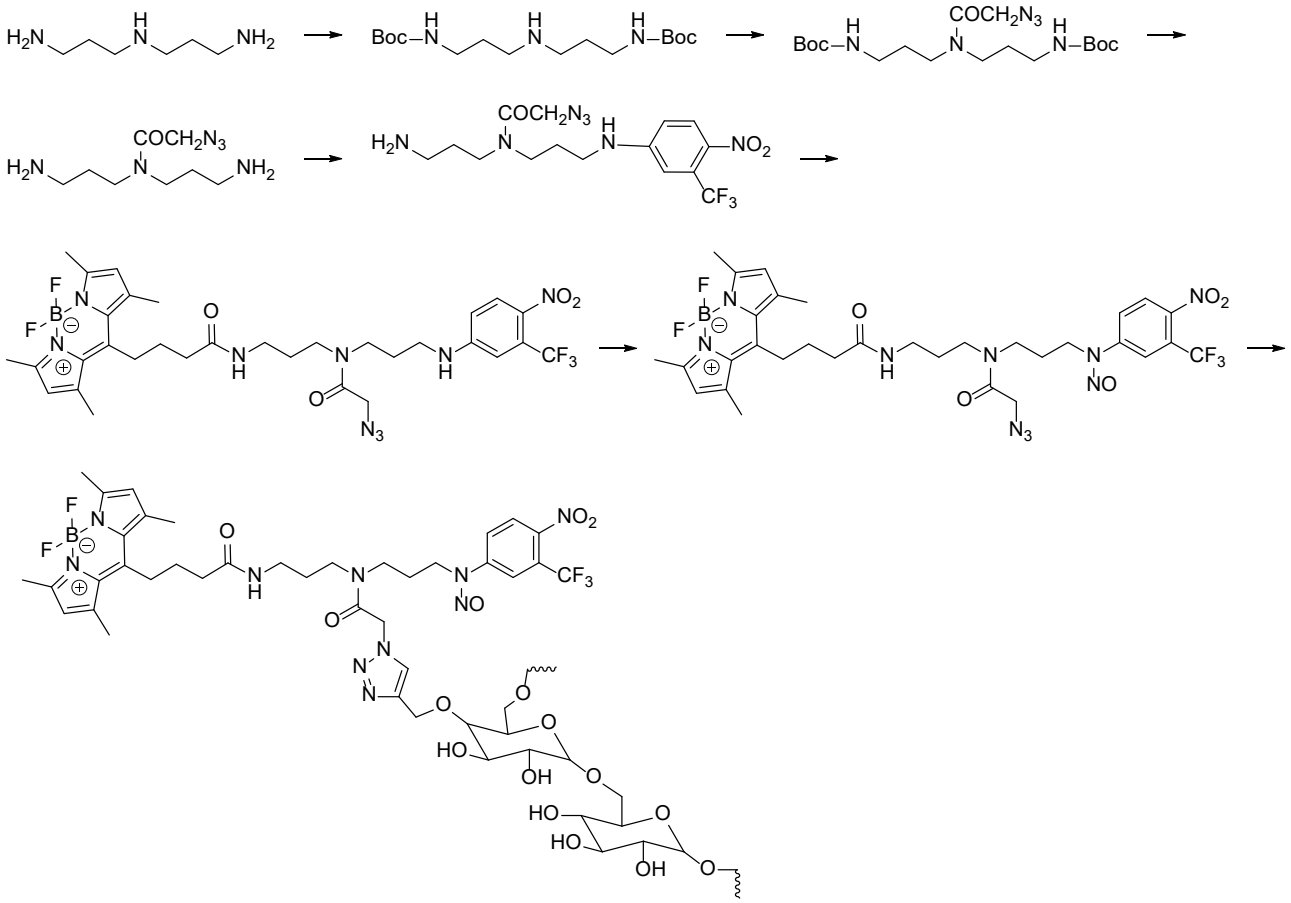

Figure 93: Projected synthesis of the novel NOPD, based on BODIPY as an Antenna and a nitrosated nitroaniline moiety.

The project provides for a subsequent encapsulation of Doxorubicin (DOX) within the polymeric scaffold. Dextrans- based polymers are widely used in literature as suitable drug nanocarriers [165], [166]. In particular, they represent optimal deliverer for antitumoral drugs, since they demonstrated to increase their blood permanence time, as a result of the reduction of kidney ultrafiltration once the mass is increased [167]. They have been reported other cases of similar dextrans polymers encapsulating DOX, which, after incorporation, has overcome the Multi Drug Resistance issues that typically displays [168].

Our novel supramolecular complex would hopefully combine the anticancer properties of the released NO as a radical cytotoxic species together with the antitumoral activity of DOX. Biological tests would be performed on DOX-resistant cells, such as HuCC-T1 cell line, to investigate the *in vitro* anticancer effects of the polymeric micelles.

Chapter 3

General conclusions

During the PhD work, different photoactivatable nanosystems were successfully designed and developed, merging the antitumoral properties of conventional chemodrugs with the release of active species (NO and $^1O_2$) and photoproduction of heat. Visible light has demonstrated to be a perfect trigger for the temperature increase and for the production of cytotoxic radicals, controlling their release in terms of space, time, and dosage. *In vitro* tests upon different cancer cells line have proven the high therapeutic potential of the nanoplatforms. An investigation of the photobehaviour of CUR, encapsulated within different biocompatible nanocarriers, has been conducted to get insight into the mechanisms behind its photobiological activities.

Acknowledgements

I would like to thank my Tutor, Prof. Salvatore Sortino, who taught be a lot in these three years (both in science and music). I also thank all the PhotoChemLab, who supported me a lot.

My acknowledgements also go to Prof. Vargas, who kindly hosted me in his laboratory, and to Dr. Valentina Marassi for her support, together with all the byFlow team. I also thank Prof. Fabiana Quaglia and Dr. Milo Malanga, who made possible part of this work.

Outcomes

Manuscripts

- F. Laneri, A. C. E. Graziano, M. Seggio, A. Fraix, M. Malanga, S. Béni, G. Longobardi, C. Conte, F. Quaglia, S. Sortino; Enhancing the Anticancer Activity of Sorafenib through Its Combination with a Nitric Oxide Photodelivering β-Cyclodextrin Polymer, **2022**, *Molecules*, 27(6), 1918;

- F. Laneri, M. Seggio, A. C. E. Graziano, M. M. Natile, A. Fraix, S. Sortino; Green Synthesis of Near-Infrared Plasmonic Gold Nanostructures by Pomegranate Extract and Their Supramolecular Assembling with Chemo-and Photo-Therapeutics, **2022**, *Nanomaterials*, 12(24), 4476;

- F. Laneri, S. García-Viñuales, V. Lanza, N. Licciardello, D. Milardi, S. Sortino, G. Grasso. Dipyridamole for tracking amyloidogenic proteins aggregation and enhancing polyubiquitination*,* **2022**, *Archives of Biochemistry and Biophysics*, 728, 109354. (This work was carried out to completion of the graduation thesis, F. Laneri, 2020, Tutor: Prof. Giuseppe Grasso);

- F. Laneri, N. Licciardello, Y. Suzuki, A. C. E. Graziano, F. Sodano, A. Fraix, S. Sortino; A Supramolecular Nanoassembly of Lenvatinib and a Green Light-Activatable NO Releaser for Combined Chemo-Phototherapy, **2023**, *Pharmaceutics*, 15(1), 96;

- F. Laneri, C. Conte., C. Parisi, O. Catanzano, A. Fraix, F. Quaglia, S. Sortino. On the photobehaviour of curcumin in biocompatible hosts: The role of H-abstraction in the photodegradation and photosensitization, **2023**, *Journal of Photochemistry and Photobiology B: Biology*, 245, 112756;

- F. Laneri, M. Seggio, C. Parisi, S. Béni, A. Fraix, M. Malanga, S. Sortino; A mixed β-γ-cyclodextrin branched polymer with multiple photochemotherapeutic cargos, **2023**, *ACS Applied Polymer Materials,* 5(10), 7918-7926*.*

Participation to conferences

- Francesca Laneri, Milo Malanga and Salvatore Sortino
  "A Fluorescent β-Cyclodextrins Polymer Encapsulating Sorafenib and Releasing Nitric Oxide Under Visible Light"
  Flash oral communication and poster at the European Society for Photobiology meeting, held in Salzburg and the World Wide Web, September 2021;

- Francesca Laneri, Aurore Fraix, Adriana Graziano, Cristina Parisi, Mimimorena Seggio, Milo Malanga and Salvatore Sortino
  "A Fluorescent β-Cyclodextrins Polymer Encapsulating Sorafenib and Releasing Nitric Oxide Under Visible Light"
  Best oral communication prize at the virtual photochemistry GIF^2-meeting, September 2021;

- Francesca Laneri, Mimimorena Seggio, Aurore Fraix, Adriana Graziano, Cristina Parisi, Milo Malanga and Salvatore Sortino
  "Biofriendly Route to Gold Nanoplasmonics through Mixed Cyclodextrin Branched Polymers Photoreleasing Nitric Oxide"
  Oral communication at the photochemistry GIF^2-meeting, Turin, December 2021;

- Francesca Laneri, Aurore Fraix, Cristina Parisi, Adriana C. E. Graziano and Salvatore Sortino
  "Development of Photoactivatable Polymeric Nanoparticles for Multimodal Antitumoral Therapies"
  Oral communication at the International Workshop on Industrial Ph.D. in the EUNICE European University, October 2022;

- Francesca Laneri, Nadia Licciardello, Yota Suzuki, Adriana Graziano, Aurore Fraix and Salvatore Sortino
  "A Cyclodextrins Based Fluorescent Supramolecular Nanoassembly for Combined Photo-Chemotherapy"

Oral communication at the photochemistry GIF2-meeting, Ferrara, December 2022;

- Francesca Laneri, Nadia Licciardello, Yota Suzuki, Adriana Graziano, Aurore Fraix, and Salvatore Sortino
  "A Supramolecular Nanoassembly of Lenvatinib and a Green Light-Activatable NO Releaser for Combined Chemo-Phototherapy"
  Best oral communication prize, 2nd place, at the PhotOnline '2023, World Wide Web, February 2023;

- Francesca Laneri, Mimimorena Seggio, Adriana C.E. Graziano, Marta M. Natile, Aurore Fraix and Salvatore Sortino
  "Green Synthesis of Near-Infrared Plasmonic Gold Nanostructures by Pomegranate Extract and Their Supramolecular Assembling with Chemo- and Photo-Therapeutics"
  Oral communication at the 20th Congress of the European Society for Photobiology meeting, Lyon, August 2023;

- Francesca Laneri, Mimimorena Seggio, Adriana C.E. Graziano, Marta M. Natile, Aurore Fraix and Salvatore Sortino
  "Green Synthesis of Near-Infrared Plasmonic Gold Nanostructures by Pomegranate Extract and Their Supramolecular Assembling with Chemo- and Photo-Therapeutics"
  Oral communication at the Nano Bio&Med Congress, Barcelona, November 2023;

- Francesca Laneri, Claudia Conte, Cristina Parisi, Ovidio Catanzaro, Aurore Fraix, Fabiana Quaglia, Salvatore Sortino
  "The photobehaviour of curcumin in biocompatible hosts: the role of H-abstraction in the photodegradation and photosensitization"
  Oral communication at the photochemistry GIF2-meeting, Sestri Levante, December 2023.

Bibliography

[1] A. Fraix, S. Sortino, in *Advances in Inorganic Chemistry* (Eds.: P.C. Ford, R. van Eldik), Academic Press, **2022**, pp. 171–203.
[2] C. Riganti, E. Miraglia, D. Viarisio, C. Costamagna, G. Pescarmona, D. Ghigo, A. Bosia, *Cancer Res* **2005**, *65*, 516–525.
[3] S. Nussbaumer, P. Bonnabry, J.-L. Veuthey, S. Fleury-Souverain, *Talanta* **2011**, *85*, 2265–2289.
[4] Y. A. Luqmani, *Med Princ Pract* **2005**, *14 Suppl 1*, 35–48.
[5] K. Onizuka, M. E. Hazemi, N. Sato, G.-I. Tsuji, S. Ishikawa, M. Ozawa, K. Tanno, K. Yamada, F. Nagatsugi, *Nucleic Acids Res* **2019**, *47*, 6578–6589.
[6] L. Infante Lara, S. Fenner, S. Ratcliffe, A. Isidro-Llobet, M. Hann, B. Bax, N. Osheroff, *Nucleic Acids Res* **2018**, *46*, 2218–2233.
[7] B. D. Bax, G. Murshudov, A. Maxwell, T. Germe, *J Mol Biol* **2019**, *431*, 3427–3449.
[8] Q. Wu, Z. Yang, Y. Nie, Y. Shi, D. Fan, *Cancer Lett* **2014**, *347*, 159–166.
[9] R. Bayat Mokhtari, T. S. Homayouni, N. Baluch, E. Morgatskaya, S. Kumar, B. Das, H. Yeger, *Oncotarget* **2017**, *8*, 38022–38043.
[10] E. Culotta, J. Daniel E. Koshland, *Science* **1992**, DOI 10.1126/science.1361684.
[11] R. SoRelle, *Circulation* **1998**, *98*, 2365–2366.
[12] Qin-ge Ding, J. Zang, S. Gao, Q. Gao, W. Duan, X. Li, W. Xu, Y. Zhang, *Drug Discoveries & Therapeutics* **2016**, *10*, 276–284.
[13] A. Fraix, N. Marino, S. Sortino, *Top Curr Chem* **2016**, *370*, 225–257.
[14] D. Fukumura, S. Kashiwagi, R. K. Jain, *Nat Rev Cancer* **2006**, *6*, 521–534.
[15] J. C. Pieretti, M. T. Pelegrino, M. H. M. Nascimento, G. R. Tortella, O. Rubilar, A. B. Seabra, *Biochemical Pharmacology* **2020**, *176*, 113740.
[16] A. Fraix, S. Sortino, *Chemistry – An Asian Journal* **2015**, *10*, 1116–1125.
[17] J. R. Hickok, D. D. Thomas, *Current Pharmaceutical Design* **2010**, *16*, 381–391.
[18] P. Klán, T. Šolomek, C. G. Bochet, A. Blanc, R. Givens, M. Rubina, V. Popik, A. Kostikov, J. Wirz, *Chem Rev* **2013**, *113*, 119–191.
[19] S. Sortino, *Chem. Soc. Rev.* **2010**, *39*, 2903–2913.
[20] N. L. Fry, P. K. Mascharak, *Acc. Chem. Res.* **2011**, *44*, 289–298.
[21] C. Ash, M. Dubec, K. Donne, T. Bashford, *Lasers Med Sci* **2017**, *32*, 1909–1918.
[22] J. P. Celli, B. Q. Spring, I. Rizvi, C. L. Evans, K. S. Samkoe, S. Verma, B. W. Pogue, T. Hasan, *Chem. Rev.* **2010**, *110*, 2795–2838.
[23] P. Agostinis, K. Berg, K. A. Cengel, T. H. Foster, A. W. Girotti, S. O. Gollnick, S. M. Hahn, M. R. Hamblin, A. Juzeniene, D. Kessel, M. Korbelik, J. Moan, P. Mroz, D. Nowis, J. Piette, B. C. Wilson, J. Golab, *CA Cancer J Clin* **2011**, *61*, 250–281.
[24] P. R. Ogilby, *Chemical Society Reviews* **2010**, *39*, 3181–3209.
[25] T. C. Pham, V.-N. Nguyen, Y. Choi, S. Lee, J. Yoon, *Chem Rev* **2021**, *121*, 13454–13619.
[26] D. L. Sai, J. Lee, D. L. Nguyen, Y.-P. Kim, *Exp Mol Med* **2021**, *53*, 495–504.
[27] I. O. L. Bacellar, T. M. Tsubone, C. Pavani, M. S. Baptista, *International Journal of Molecular Sciences* **2015**, *16*, 20523–20559.
[28] S. Sortino, *J. Mater. Chem.* **2011**, *22*, 301–318.
[29] K. Kadish, R. Guilard, K. M. Smith, *The Porphyrin Handbook: Phthalocyanines: Properties and Materials*, Elsevier, **2012**.

[30] S. Wang, R. Gao, F. Zhou, M. Selke, *J. Mater. Chem.* **2004**, *14*, 487–493.
[31] A. Fraix, S. Sortino, *Photochem Photobiol Sci* **2018**, *17*, 1709–1727.
[32] X. Li, J. F. Lovell, J. Yoon, X. Chen, *Nat Rev Clin Oncol* **2020**, *17*, 657–674.
[33] R. R. Anderson, J. A. Parrish, *Science* **1983**, *220*, 524–527.
[34] Y. Yu, L. Yan, J. Si, Y. Xu, X. Hou, *Journal of Physics and Chemistry of Solids* **2019**, *132*, 116–120.
[35] M. Camerin, S. Rello, A. Villanueva, X. Ping, M. E. Kenney, M. A. J. Rodgers, G. Jori, *European Journal of Cancer* **2005**, *41*, 1203–1212.
[36] G. Jori, J. D. Spikes, *Journal of Photochemistry and Photobiology B: Biology* **1990**, *6*, 93–101.
[37] P. K. Jain, X. Huang, I. H. El-Sayed, M. A. El-Sayed, *Acc. Chem. Res.* **2008**, *41*, 1578–1586.
[38] M. Hu, J. Chen, Z.-Y. Li, L. Au, G. V. Hartland, X. Li, M. Marquez, Y. Xia, *Chem. Soc. Rev.* **2006**, *35*, 1084–1094.
[39] V. Myroshnychenko, J. Rodríguez-Fernández, I. Pastoriza-Santos, A. M. Funston, C. Novo, P. Mulvaney, L. M. Liz-Marzán, F. J. G. de Abajo, *Chem. Soc. Rev.* **2008**, *37*, 1792–1805.
[40] S. Ashraf, B. Pelaz, P. del Pino, M. Carril, A. Escudero, W. J. Parak, M. G. Soliman, Q. Zhang, C. Carrillo-Carrion, *Top Curr Chem* **2016**, *370*, 169–202.
[41] N. Kandoth, E. Vittorino, M. T. Sciortino, T. Parisi, I. Colao, A. Mazzaglia, S. Sortino, *Chem. Eur. J.* **2012**, *18*, 1684–1690.
[42] S. V. Kurkov, T. Loftsson, *International Journal of Pharmaceutics* **2013**, *453*, 167–180.
[43] A. Baykal, A. Bozkurt, R. Jeremy, S. M. M. Asiri, M. K. Lima-Tenório, C. Kaewsaneha, A. Elaissari, in *Stimuli Responsive Polymeric Nanocarriers for Drug Delivery Applications*, Elsevier, **2019**, pp. 155–193.
[44] T. Loftsson, M. E. Brewster, *Journal of Pharmacy and Pharmacology* **2010**, *62*, 1607–1621.
[45] E. Bilensoy, Ed. , *Cyclodextrins in Pharmaceutics, Cosmetics, and Biomedicine: Current and Future Industrial Applications*, John Wiley & Sons, Inc., Hoboken, NJ, USA, **2011**.
[46] R. Challa, A. Ahuja, J. Ali, R. K. Khar, *AAPS PharmSciTech* **2005**, *6*, E329–E357.
[47] H. B. El-Serag, *Gastroenterology* **2012**, *142*, 1264-1273.e1.
[48] S. L. Abrams, P. P. Ruvolo, V. R. Ruvolo, G. Ligresti, A. M. Martelli, L. Cocco, S. Ratti, A. Tafuri, L. S. Steelman, S. Candido, M. Libra, J. A. McCubrey, *Oncotarget* **2017**, *8*, 76525–76557.
[49] J. M. Llovet, S. Ricci, V. Mazzaferro, P. Hilgard, E. Gane, J.-F. Blanc, A. C. de Oliveira, A. Santoro, J.-L. Raoul, A. Forner, M. Schwartz, C. Porta, S. Zeuzem, L. Bolondi, T. F. Greten, P. R. Galle, J.-F. Seitz, I. Borbath, D. Häussinger, T. Giannaris, M. Shan, M. Moscovici, D. Voliotis, J. Bruix, SHARP Investigators Study Group, *N Engl J Med* **2008**, *359*, 378–390.
[50] A.-L. Cheng, Y.-K. Kang, Z. Chen, C.-J. Tsao, S. Qin, J. S. Kim, R. Luo, J. Feng, S. Ye, T.-S. Yang, J. Xu, Y. Sun, H. Liang, J. Liu, J. Wang, W. Y. Tak, H. Pan, K. Burock, J. Zou, D. Voliotis, Z. Guan, *Lancet Oncol* **2009**, *10*, 25–34.
[51] B. Escudier, T. Eisen, W. M. Stadler, C. Szczylik, S. Oudard, M. Siebels, S. Negrier, C. Chevreau, E. Solska, A. A. Desai, F. Rolland, T. Demkow, T. E. Hutson, M. Gore, S. Freeman, B. Schwartz, M. Shan, R. Simantov, R. M. Bukowski, TARGET Study Group, *N Engl J Med* **2007**, *356*, 125–134.
[52] A. Moreno-Aspitia, *Future Oncology* **2010**, *6*, 655–663.
[53] J. Mangana, M. P. Levesque, M. B. Karpova, R. Dummer, *Expert Opinion on Investigational Drugs* **2012**, *21*, 557–568.
[54] F. Pitoia, F. Jerkovich, *Drug Design, Development and Therapy* **2016**, *10*, 1119–1131.
[55] T. Kacan, E. Nayir, A. Altun, S. Kilickap, N. A. Babacan, H. Ataseven, T. Kaya, *Journal of Oncological Sciences* **2016**, *2*, 53–57.
[56] K. Almhanna, P. A. Philip, *Onco Targets Ther* **2009**, *2*, 261–267.

[57] S. Bracarda, E. M. Ruggeri, M. Monti, M. Merlano, A. D'Angelo, F. Ferraù, E. Cortesi, A. Santoro, Sorafenib Working Group, *Crit Rev Oncol Hematol* **2012**, *82*, 378–386.
[58] Z. Ren, K. Zhu, H. Kang, M. Lu, Z. Qu, L. Lu, T. Song, W. Zhou, H. Wang, W. Yang, X. Wang, Y. Yang, L. Shi, Y. Bai, X. Guo, S.-L. Ye, *J Clin Oncol* **2015**, *33*, 894–900.
[59] Y. Li, Z.-H. Gao, X.-J. Qu, *Basic & Clinical Pharmacology & Toxicology* **2015**, *116*, 216–221.
[60] M. Cervello, D. Bachvarov, N. Lampiasi, A. Cusimano, A. Azzolina, J. A. McCubrey, G. Montalto, *PLOS ONE* **2013**, *8*, e65569.
[61] L. Almeida e Sousa, S. M. Reutzel-Edens, G. A. Stephenson, L. S. Taylor, *Mol. Pharmaceutics* **2015**, *12*, 484–495.
[62] M. A. Khan, A. Raza, M. Ovais, M. F. Sohail, S. Ali, *International Journal of Polymeric Materials and Polymeric Biomaterials* **2018**, *67*, 1105–1115.
[63] M. L. Bondì, A. Scala, G. Sortino, E. Amore, C. Botto, A. Azzolina, D. Balasus, M. Cervello, A. Mazzaglia, *Biomacromolecules* **2015**, *16*, 3784–3791.
[64] F. Sukkar, M. Shafaa, M. El-Nagdy, W. Darwish, *International Journal of Nanomedicine* **2021**, *16*, 8309–8321.
[65] Z. Li, L. Ye, J. Liu, D. Lian, X. Li, *International Journal of Nanomedicine* **2020**, *15*, 1469–1480.
[66] F. Chen, Y. Fang, X. Chen, R. Deng, Y. Zhang, J. Shao, *Asian Journal of Pharmaceutical Sciences* **2021**, *16*, 318–336.
[67] K. Mg, K. V, H. F, *J Nanomed Nanotechnol* **2015**, *06*, DOI 10.4172/2157-7439.1000336.
[68] J. S. Lagas, R. A. B. van Waterschoot, R. W. Sparidans, E. Wagenaar, J. H. Beijnen, A. H. Schinkel, *Mol Cancer Ther* **2010**, *9*, 319–326.
[69] S. Ghassabian, T. Rawling, F. Zhou, M. R. Doddareddy, B. N. Tattam, D. E. Hibbs, R. J. Edwards, P. H. Cui, M. Murray, *Biochem Pharmacol* **2012**, *84*, 215–223.
[70] J. P. Rigalli, N. Ciriaci, A. Arias, M. P. Ceballos, S. S. M. Villanueva, M. G. Luquita, A. D. Mottino, C. I. Ghanem, V. A. Catania, M. L. Ruiz, *PLOS ONE* **2015**, *10*, e0119502.
[71] Z. T. Al-Salama, Y. Y. Syed, L. J. Scott, *Drugs* **2019**, *79*, 665–674.
[72] *Cancer Treatment Reviews* **2016**, *42*, 47–55.
[73] M. Schlumberger, M. Tahara, L. J. Wirth, B. Robinson, M. S. Brose, R. Elisei, M. A. Habra, K. Newbold, M. H. Shah, A. O. Hoff, A. G. Gianoukakis, N. Kiyota, M. H. Taylor, S.-B. Kim, M. K. Krzyzanowska, C. E. Dutcus, B. de las Heras, J. Zhu, S. I. Sherman, *N Engl J Med* **2015**, *372*, 621–630.
[74] R. J. Motzer, T. E. Hutson, H. Glen, M. D. Michaelson, A. Molina, T. Eisen, J. Jassem, J. Zolnierek, J. P. Maroto, B. Mellado, B. Melichar, J. Tomasek, A. Kremer, H.-J. Kim, K. Wood, C. Dutcus, J. Larkin, *Lancet Oncol* **2015**, *16*, 1473–1482.
[75] *The Lancet* **2018**, *391*, 1163–1173.
[76] N. V. S. REDDY, A. K. Kapoor, A. Nath, M. Prasad, *Crystalline Forms of Salts of Lenvatinib*, **2017**, WO2017221214A1.
[77] S. Chen, Q. Cao, W. Wen, H. Wang, *Cancer Letters* **2019**, *460*, 1–9.
[78] S. Zhang, L. Zhao, X. Peng, Q. Sun, X. Liao, N. Gan, G. Zhao, H. Li, *Colloids and Surfaces B: Biointerfaces* **2021**, *201*, 111644.
[79] L. Ielasi, F. Tovoli, F. Piscaglia, *Drugs Today* **2019**, *55*, 305.
[80] H. Takeda, N. Nishijima, A. Nasu, H. Komekado, R. Kita, T. Kimura, M. Kudo, Y. Osaki, *Hepatol Res* **2019**, *49*, 594–599.
[81] EMA, "Lenvima," can be found under https://www.ema.europa.eu/en/medicines/human/EPAR/lenvima, **2018**.
[82] M. Othman, K. Bouchemal, P. Couvreur, D. Desmaële, E. Morvan, T. Pouget, R. Gref, *Journal of Colloid and Interface Science* **2011**, *354*, 517–527.

[83] C. Parisi, M. Failla, A. Fraix, B. Rolando, E. Gianquinto, F. Spyrakis, E. Gazzano, C. Riganti, L. Lazzarato, R. Fruttero, A. Gasco, S. Sortino, *Chemistry – A European Journal* **2019**, *25*, 11080–11084.
[84] C. Parisi, M. Seggio, A. Fraix, S. Sortino, *ChemPhotoChem* **2020**, *4*, 742–748.
[85] F. L. Callari, S. Sortino, *Chem. Commun.* **2008**, 1971–1973.
[86] M. Malanga, M. Seggio, V. Kirejev, A. Fraix, I. D. Bari, E. Fenyvesi, M. B. Ericson, S. Sortino, *Biomater. Sci.* **2019**, *7*, 2272–2276.
[87] T. Suzuki, O. Nagae, Y. Kato, H. Nakagawa, K. Fukuhara, N. Miyata, *J. Am. Chem. Soc.* **2005**, *127*, 11720–11726.
[88] V. Giglio, M. Viale, V. Bertone, I. Maric, R. Vaccarone, G. Vecchio, *Invest New Drugs* **2018**, *36*, 370–379.
[89] A. Fraix, V. Kirejev, M. Malanga, É. Fenyvesi, S. Béni, M. B. Ericson, S. Sortino, *Chemistry – A European Journal* **2019**, *25*, 7091–7095.
[90] S. Swaminathan, J. Garcia-Amorós, A. Fraix, N. Kandoth, S. Sortino, F. M. Raymo, *Chemical Society Reviews* **2014**, *43*, 4167–4178.
[91] N. Kandoth, V. Kirejev, S. Monti, R. Gref, M. B. Ericson, S. Sortino, *Biomacromolecules* **2014**, *15*, 1768–1776.
[92] V. Kirejev, N. Kandoth, R. Gref, M. B. Ericson, S. Sortino, *J. Mater. Chem. B* **2014**, *2*, 1190–1195.
[93] A. Fraix, N. Kandoth, I. Manet, V. Cardile, A. C. E. Graziano, R. Gref, S. Sortino, *Chem. Commun.* **2013**, *49*, 4459–4461.
[94] PubChem, "Sorafenib," can be found under https://pubchem.ncbi.nlm.nih.gov/compound/216239.
[95] E. B. Caruso, S. Petralia, S. Conoci, S. Giuffrida, S. Sortino, *J. Am. Chem. Soc.* **2007**, *129*, 480–481.
[96] R. Coriat, C. Nicco, C. Chéreau, O. Mir, J. Alexandre, S. Ropert, B. Weill, S. Chaussade, F. Goldwasser, F. Batteux, *Molecular Cancer Therapeutics* **2012**, *11*, 2284–2293.
[97] G. Czapski, S. Goldstein, *Free Radical Biology and Medicine* **1995**, *19*, 785–794.
[98] C.-F. Chang, A. R. Diers, N. Hogg, *Free Radical Biology and Medicine* **2015**, *79*, 324–336.
[99] S. Moncada, J. D. Erusalimsky, *Nat Rev Mol Cell Biol* **2002**, *3*, 214–220.
[100] D. A. Wink, Y. Vodovotz, J. Laval, F. Laval, M. W. Dewhirst, J. B. Mitchell, *Carcinogenesis* **1998**, *19*, 711–721.
[101] Z. Huang, J. Fu, Y. Zhang, *J. Med. Chem.* **2017**, *60*, 7617–7635.
[102] C. Parisi, M. Failla, A. Fraix, A. Rescifina, B. Rolando, L. Lazzarato, V. Cardile, A. C. E. Graziano, R. Fruttero, A. Gasco, S. Sortino, *Bioorganic Chemistry* **2019**, *85*, 18–22.
[103] E. Deniz, N. Kandoth, A. Fraix, V. Cardile, A. C. E. Graziano, D. Lo Furno, R. Gref, F. M. Raymo, S. Sortino, *Chemistry – A European Journal* **2012**, *18*, 15782–15787.
[104] *Handbook of Photochemistry*, CRC Press, **2006**.
[105] B. J. Brinda, F. Viganego, T. Vo, D. Dolan, M. G. Fradley, *Curr Treat Options Cardiovasc Med* **2016**, *18*, 33.
[106] P. Kruzliak, G. Kovacova, O. Pechanova, *Angiogenesis* **2013**, *16*, 289.
[107] C. Fowley, A. P. McHale, B. McCaughan, A. Fraix, S. Sortino, J. F. Callan, *Chem. Commun.* **2014**, *51*, 81–84.
[108] F. Sodano, R. J. Cavanagh, A. K. Pearce, L. Lazzarato, B. Rolando, A. Fraix, T. F. Abelha, C. E. Vasey, C. Alexander, V. Taresco, S. Sortino, *Biomater. Sci.* **2020**, *8*, 1329–1344.
[109] P. Taladriz-Blanco, M. G. de Oliveira, *Journal of Photochemistry and Photobiology A: Chemistry* **2014**, *293*, 65–71.

[110] C. Udagawa, S. Fukuyoshi, S. Morimoto, Y. Tanimoto, R. Nakagaki, *Journal of Photochemistry and Photobiology A: Chemistry* **2011**, *226*, 57–63.
[111] I. D. Bari, R. Picciotto, G. Granata, A. R. Blanco, G. M. L. Consoli, S. Sortino, *Organic & Biomolecular Chemistry* **2016**, *14*, 8047–8052.
[112] M. Morisue, S. Ueda, M. Kurasawa, M. Naito, Y. Kuroda, *J. Phys. Chem. A* **2012**, *116*, 5139–5144.
[113] L. H. and, J. Z. Zhang*, "Ultrafast Studies of Excited-State Dynamics of Phthalocyanine and Zinc Phthalocyanine Tetrasulfonate in Solution," DOI 10.1021/jp9622445can be found under https://pubs.acs.org/doi/pdf/10.1021/jp9622445, **1997**.
[114] B. Brożek-Płuska, A. Jarota, K. Kurczewski, H. Abramczyk, *Journal of Molecular Structure* **2009**, *924–926*, 338–346.
[115] A. Ruebner, Z. Yang, D. Leung, R. Breslow, *Proceedings of the National Academy of Sciences* **1999**, *96*, 14692–14693.
[116] J. W. Park, H. J. Song, *J. Phys. Chem.* **1989**, *93*, 6454–6458.
[117] H. S. Jung, P. Verwilst, A. Sharma, J. Shin, J. L. Sessler, J. S. Kim, *Chem. Soc. Rev.* **2018**, *47*, 2280–2297.
[118] Q. Hu, Y. Lu, Y. Luo, *Carbohydrate Polymers* **2021**, *264*, 117999.
[119] P.-P. Yang, Y.-G. Zhai, G.-B. Qi, Y.-X. Lin, Q. Luo, Y. Yang, A.-P. Xu, C. Yang, Y.-S. Li, L. Wang, H. Wang, *Small* **2016**, *12*, 5423–5430.
[120] L. C. Kennedy, L. R. Bickford, N. A. Lewinski, A. J. Coughlin, Y. Hu, E. S. Day, J. L. West, R. A. Drezek, *Small* **2011**, *7*, 169–183.
[121] J. C. Scaiano, P. Billone, C. M. Gonzalez, L. Marett, M. L. Marin, K. L. McGilvray, N. Yuan, *Pure and Applied Chemistry* **2009**, *81*, 635–647.
[122] G. Nocito, S. Petralia, M. Malanga, S. Béni, G. Calabrese, R. Parenti, S. Conoci, S. Sortino, *ACS Appl. Nano Mater.* **2019**, *2*, 7916–7923.
[123] R. Martin-Trasanco, R. Cao, H. E. Esparza-Ponce, M. E. Montero-Cabrera, R. Arratia-Pérez, *Carbohydrate Polymers* **2017**, *175*, 530–537.
[124] E. Ye, K. Y. Win, H. R. Tan, M. Lin, C. P. Teng, A. Mlayah, M.-Y. Han, *J. Am. Chem. Soc.* **2011**, *133*, 8506–8509.
[125] R. Martin-Trasanco, R. Cao, H. E. Esparza-Ponce, L. García-Pupo, M. E. Montero-Cabrera, *RSC Advances* **2015**, *5*, 98440–98446.
[126] W. Ni, Z. Yang, H. Chen, L. Li, J. Wang, *J. Am. Chem. Soc.* **2008**, *130*, 6692–6693.
[127] E.-O. Ganbold, J.-H. Park, U. Dembereldorj, K.-S. Ock, S.-W. Joo, *Journal of Raman Spectroscopy* **2011**, *42*, 1614–1619.
[128] V. Sueth-Santiago, G. Peron, D. Decoté-Ricardo, M. Lima, *Química Nova* **2015**, *38*, DOI 10.5935/0100-4042.20150035.
[129] M. Salem, S. Rohani, E. R. Gillies, *RSC Advances* **2014**, *4*, 10815–10829.
[130] M. J. Dehzad, H. Ghalandari, M. Nouri, M. Askarpour, *Cytokine* **2023**, *164*, 156144.
[131] D. Akbik, M. Ghadiri, W. Chrzanowski, R. Rohanizadeh, *Life Sciences* **2014**, *116*, 1–7.
[132] A. M. Pourbagher-Shahri, T. Farkhondeh, M. Ashrafizadeh, M. Talebi, S. Samargahndian, *Biomedicine & Pharmacotherapy* **2021**, *136*, 111214.
[133] S. Mukherjee, A. K. Mishra, G. D. G. Peer, S. A. Bagabir, S. Haque, R. P. Pandey, V. S. Raj, N. Jain, A. Pandey, S. K. Kar, *Frontiers in Aging Neuroscience* **2021**, *13*.
[134] K. T. Kazantzis, K. Koutsonikoli, B. Mavroidi, M. Zachariadis, P. Alexiou, M. Pelecanou, K. Politopoulos, E. Alexandratou, M. Sagnou, *Photochem Photobiol Sci* **2020**, *19*, 193–206.
[135] L. D. Dias, K. C. Blanco, I. S. Mfouo-Tynga, N. M. Inada, V. S. Bagnato, *Journal of Photochemistry and Photobiology C: Photochemistry Reviews* **2020**, *45*, 100384.

[136] “Photophysics, photochemistry and photobiology of curcumin: Studies from organic solutions, bio-mimetics and living cells - ScienceDirect,” can be found under https://www.sciencedirect.com/science/article/pii/S1389556709000331.
[137] H. H. Tønnesen, J. Karlsen, *Z Lebensm Unters Forsch* **1985**, *180*, 402–404.
[138] R. Tabanelli, S. Brogi, V. Calderone, *Pharmaceutics* **2021**, *13*, 1715.
[139] S. Maleki Dizaj, M. Alipour, E. Dalir Abdolahinia, E. Ahmadian, A. Eftekhari, H. Forouhandeh, Y. Rahbar Saadat, S. Sharifi, S. Zununi Vahed, *Phytotherapy Research* **2022**, *36*, 1156–1181.
[140] A. Karthikeyan, N. Senthil, T. Min, *Front Pharmacol* **2020**, *11*, 487.
[141] M. A. Tănase, A. C. Soare, L. M. Diţu, C. L. Nistor, C. I. Mihaescu, I. C. Gifu, C. Petcu, L. O. Cinteza, *Pharmaceutics* **2022**, *14*, 2137.
[142] A. Fraix, O. Catanzano, I. D. Bari, C. Conte, M. Seggio, C. Parisi, A. Nostro, G. Ginestra, F. Quaglia, S. Sortino, *J. Mater. Chem. B* **2019**, *7*, 5257–5264.
[143] “SPECTRAL AND PHOTOCHEMICAL PROPERTIES OF CURCUMIN - Chignell - 1994 - Photochemistry and Photobiology - Wiley Online Library,” can be found under https://onlinelibrary.wiley.com/doi/abs/10.1111/j.1751-1097.1994.tb05037.x.
[144] S. M. Khopde, K. Indira Priyadarsini, D. K. Palit*, T. Mukherjee, *Photochemistry and Photobiology* **2000**, *72*, 625–631.
[145] L. Nardo, R. Paderno, A. Andreoni, M. Másson, T. Haukvik, H. H. Tønnesen, *Spectroscopy* **2008**, *22*, 187–198.
[146] R. Adhikary, P. J. Carlson, T. W. Kee, J. W. Petrich, *J. Phys. Chem. B* **2010**, *114*, 2997–3004.
[147] F. Ortica, M. a. J. Rodgers, *Photochemistry and Photobiology* **2001**, *74*, 745–751.
[148] A. Barik, K. I. Priyadarsini, H. Mohan, *Photochem Photobiol* **2003**, *77*, 597–603.
[149] H. Dezhampanah, Z. Shabanzade, *J Biomol Struct Dyn* **2022**, *40*, 722–732.
[150] A. C. Pulla Reddy, E. Sudharshan, A. G. Appu Rao, B. R. Lokesh, *Lipids* **1999**, *34*, 1025–1029.
[151] C. Santezi, B. D. Reina, L. N. Dovigo, *Photodiagnosis and Photodynamic Therapy* **2018**, *21*, 409–415.
[152] “The Role of Singlet Oxygen in Photoreactivity and Phototoxicity of Curcumin - Wolnicka-Glubisz - 2023 - Photochemistry and Photobiology - Wiley Online Library,” can be found under https://onlinelibrary.wiley.com/doi/full/10.1111/php.13666.
[153] A. A. Gorman, I. Hamblett, V. S. Srinivasan, P. D. Wood, *Photochemistry and Photobiology* **1994**, *59*, 389–398.
[154] S. V. Jovanovic, C. W. Boone, S. Steenken, M. Trinoga, R. B. Kaskey, *J. Am. Chem. Soc.* **2001**, *123*, 3064–3068.
[155] M. A. Rankin, B. D. Wagner, *Supramolecular Chemistry* **2004**, *16*, 513–519.
[156] K. N. Baglole, P. G. Boland, B. D. Wagner, *Journal of Photochemistry and Photobiology A: Chemistry* **2005**, *173*, 230–237.
[157] N. J. Turro, V. Ramamurthy, J. C. Scaiano, *Modern Molecular Photochemistry of Organic Molecules*, Univ Science Books, Sausalito, Calif, **2010**.
[158] J. C. Scaiano, J. C. Selwyn, *Can. J. Chem.* **1981**, *59*, 2368–2372.
[159] J. C. Scaiano, E. B. Abuin, L. C. Stewart, *J. Am. Chem. Soc.* **1982**, *104*, 5673–5679.
[160] P. P. Levin, A. F. Efremkin, N. B. Sultimova, V. V. Kasparov, I. V. Khudyakov, *Photochemistry and Photobiology* **2014**, *90*, 369–373.
[161] M. R. Hamblin, T. Hasan, *Photochem Photobiol Sci* **2004**, *3*, 436–450.
[162] M. Wainwright, *Photosensitisers in Biomedicine*, Wiley, Chichester, UK ; Hoboken, NJ, **2010**.
[163] K. C. Das, C. K. Das, *Biochemical and Biophysical Research Communications* **2002**, *295*, 62–66.
[164] A. Wolnicka-Glubisz, M. Olchawa, M. Duda, P. Pabisz, A. Wisniewska-Becker, *Photochemistry and Photobiology* **2023**, *99*, 57–67.
[165] S. Huang, G. Huang, *Drug Deliv* **2019**, *26*, 252–261.

[166] S. Lee, A. Stubelius, N. Hamelmann, V. Tran, A. Almutairi, *ACS Appl Mater Interfaces* **2018**, *10*, 40378–40387.
[167] J. Varshosaz, *Expert Opin Drug Deliv* **2012**, *9*, 509–523.
[168] Y.-I. Jeong, D. H. Kim, C.-W. Chung, J.-J. Yoo, K. H. Choi, C. H. Kim, S. H. Ha, D. H. Kang, *Int J Nanomedicine* **2011**, *6*, 1415–1427.

La borsa di dottorato è stata cofinanziata con risorse del
Programma Operativo Nazionale Ricerca e Innovazione 2014-2020 (CCI 2014IT16M2OP005),
Fondo Sociale Europeo, Azione I.1 "Dottorati Innovativi con caratterizzazione Industriale"

UNIONE EUROPEA
Fondo Sociale Europeo